6-11-2018

Toward More Efficient Solar Energy Conversion Using Molecularly Anchored Nanocatalysts and Novel Porphyrinoid Dyes

Bowen Yang
University of Connecticut - Storrs, bowen.yang@uconn.edu

Toward More Efficient Solar Energy Conversion Using Molecularly Anchored Nanocatalysts and Novel Porphyrinoid Dyes

Bowen Yang, Ph.D.

University of Connecticut, 2018

The scarcity and pollution of fossil fuels, together with the high cost of conventional silicon-based solar cells, have motivated the development of lower-cost means of converting sunlight to electrical power. The dye-sensitized solar cell (DSC) is a promising technology, with a cheap TiO_2 nanoparticle film coated with dye molecules that absorb sunlight and inject excited electrons into the nanoparticles. After electrons are extracted from the TiO_2 and routed through an electrical load to provide power, they are returned to the dye via electrochemical reactions involving a dissolved redox couple that surrounds the dye. While the cost of the DSC is low, there is a need to improve its efficiency, which stands at a record of 14%, about half the value for silicon solar cells.

Two routes are described to improve the efficiency. One way is to reduce the energy loss in redox reactions in the device using platinum nanoparticles as nanocatalysts. This involves Pt nanoparticle synthesis, coupling of customized dyes to Pt and to TiO_2, and characterization of resulting devices. The second route involves modifying strongly light-absorbing porphyrin molecules to work as dyes in DSC devices. This requires the characterization of redox and optical properties of different porphyrin dyes and chemical modification to allow attachment to TiO_2 nanoparticles.

Toward More Efficient Solar Energy Conversion Using Molecularly Anchored Nanocatalysts and Novel Porphyrinoid Dyes

Bowen Yang

B.S., Jilin University, **2013**

A Dissertation

Submitted in Partial Fulfillment of the

Requirements for the Degree of

Doctor of Philosophy

at the

University of Connecticut

2018

APPROVAL PAGE

Doctor of Philosophy Dissertation

Toward More Efficient Solar Energy Conversion Using Molecularly Anchored Nanocatalysts and Novel Porphyrinoid Dyes

Presented by

Bowen Yang, B.S.

Major Advisor

_____

Dr. Alexander G. Agrios

Associate Advisor

_____

Dr. Elena Galoppini

Associate Advisor

_____

Dr. Christian Brückner

Associate Advisor

_____

Dr. Baikun Li

Associate Advisor

_____

Dr. Timothy Vadas

University of Connecticut
2018

Acknowledgement

It has been an amazing and special journey when I look back on the years of my Ph.D. career in the United States. My grandma, who I admire and respect the most, was a senior high school headmaster and my first teacher in life. She always said I would be a great learner and researcher – even when I was just five years old, reading books on her knee. Now, twenty years later, I'm getting my Ph.D., and will continue working in research.

First and foremost, I would like to thank my advisor Dr. Alexander G. Agrios, for introducing me to the interesting world of photovoltaics, for giving me a lot of freedom, being patient and supportive of my research, allowing me to be an independent researcher, and for the financial support. I am grateful he gave me the opportunity to join his research group and to get to know his lovely family. They are so sweet and I wish them all the best. I would also like to thank my previous lab mate Juanpa, for his generosity, training and help my first year.

This of course, could not have been possible without the support of my collaborators. I would like to thank Dr. Galoppini and her graduate student, Ian Weiss, at Rutgers University, for their hard work on synthesizing those complicate dye molecules and helpful discussion. I would like to thank Dr. Brückner for all his support and guidance on our projects and for the financial support of my last summer of stay. I have also had the pleasure of working with Nisansala Hewage, our collaborator in Dr. Brückner's group, who is excellent at making those beautiful porphyrin molecules. We are not only collaborators, but good friends, who always get together to discuss research and to share our lives. Furthermore, I would like to thank Dr. Vadas and Dr. Li for being a part of my advisory committee.

Over the past five years, I am extremely grateful to have had the loving support of many best friends. These include, Lingyu, Taofeek, Nancy, Feiwei, Jiayu, Celicia and her whole family. I can't image how my life would be without them. They were a source of happiness, encouragement and company. We'll be friends and family forever.

I dedicate this thesis to my family, my amazing husband and fantastic parents. Thank you so much for allowing me to grow up in love and happiness. Thank you so much for encouraging me and supporting me to pursue and fulfill my dreams. Thank you so much for sharing life with me, for always being there with me and always being proud of me. I feel so lucky to have you in my life and I would not be where I am today without you.

Last but not least, I would like to thank myself for overcoming all the difficulties I went through. Thank you to myself for always being positive and optimistic, for not being afraid of but enjoying all the challenges, for never give up. And thanks for all the experiences I had, good or bad, you made me stronger and better.

TABLE OF CONTENTS

LIST OF SCHEMES

LIST OF FIGURES

LIST OF TABLES

Sections of this thesis have been, and will be, published as follows:

- Yang, B.; Hewage, N.; Guberman-Pfeffer, M. J.; Gascon, J.; Wax, T.; Zhao, J.; Agrios, A. G.; Brückner, C.; 'Electronic Modulation of *meso*-Pentafluorophenyl-substituted Chlorins and Bacteriochlorins through Chromene-annulation', accepted by *Physical Chemistry Chemical Physics*.

  Contributions: BY: performed electrochemistry experiments and electronic state calculations; NH: provided the synthesis of the chromene-annulated hydroporphyrins and structural determination, JG: accomplished the DFT calculations; TW: provided the time-resolved photoluminescence measurements; all were involved in the writing of the manuscript.

- Yang, B.; Agrios, A. G.; 'Attachment of Pt nanoparticles to a metal oxide surface using a thiol-carboxyl bifunctional molecule' *Journal of Colloid and Interface Science*. **2018**, *513*, 464-469.

  Contributions: BY: provided the experiments, data analysis and writing of the manuscript.

- Hewage, N.; Yang, B.; Agrios, A. G.; Brückner, C.; 'Introduction of carboxylic ester and acid functionalities to *meso*-tetrakis(pentafluorophenyl)porphyrin and their limited electronic effects on the chromophore' *Dyes and Pigments*. **2015**, *121*, 159-169.

  Contributions: NH: performed porphyrinoid dyes synthesis and the structural determinations; BY: obtained the electronic and attachment measurements and analysis; all were involved in the writing of the manuscript.

CHAPTER 1. MOTIVATION

1.1 Objectives

The dye-sensitized solar cell is a promising technology which has attracted a great deal of attention since 1991 when O'Regan and Gräztel reported a breakthrough efficiency of 7-8%, with a change in paradigm, from planar p-n junctions to a 3-dimensional nano-crystalline architecture.[3] With the effects of the last over 20 years, the record conversion efficiency is now standing at over 14% under one sun illumination.[4] However, the low solar-to-electrical power conversion efficiency and stability have remained the major challenges for DSCs, comparing with other types of photovoltaic solar cells.

Therefore, the overall goal of this dissertation is to improve the solar power conversion efficiency of dye-sensitized solar cells in two ways.

The first objective of this project is to understand and develop a more efficient DSC device by using Pt nanoparticles as nanocatalysts to reduce the energy loss in redox reactions involving the iodide/triiodide redox mediator. Our collaborators, Prof. Galoppini's group at Rutgers University--Newark, are synthesizing novel dye molecules. These dyes are bifunctional in that they have a thiol or disulfide group to bind to Pt, in addition to a carboxyl group to attach to TiO_2 surface, shown in Figure 1-1.

The second objective is to study the electrochemical properties of various modified strongly light-absorbing novel porphyrinoid molecules to work as sensitizers in DSC devices. Our collaborator, Prof. Brückner's group in the Chemistry Department at UConn, has introduced carboxylic ester and acid functionalities to *meso*-tetrakis(pentafluorophenyl)porphyrin (T^FPP) molecules. Because

alkyl- or aryl-carboxylic acid-functionalized porphyrinic dyes are sought after due to their propensity to adhere strongly to many metal oxide surfaces as required for their application as sensitizers in dye-sensitized solar cells. However, from a practical point of view, the synthesis of porphyrinoid dyes with a single or multiple carboxylic acid groups is associated with practical difficulties since conventional bulk silica gel column chromatography techniques are difficult to apply to (poly)carboxylates. This suggests the unveiling of the carboxyl functionality at a very late stage of the dye synthesis, such as by synthesis of protected carboxyl derivatives that are deprotected directly prior to attachment to the semiconductor and introduce the carboxyl group to the dye at a late – ideally final – synthetic stage. Therefore, we are interested in whether the introduction of one to four thiols or catechols to the (C_6F_5)-groups would affect the electronic structure of the chromophore, if their HOMO-LUMO energy levels match the energy diagram and whether these (C_6F_5)-substituted porphyrinoid dyes would link to a surface of semiconductor working electrodes through carboxylic acid groups for application as sensitizers in DSCs.

In addition, our collaborator, Prof. Brückner's group also synthesized series dye molecules of *meso*-pentafluorophenyl-substituted chlorins and bacteriochlorins through chromene-annulation. Since at the time of the discovery of the chromene-annulated hydroporphyrins, the details of the origins of their electronic modulations were not further investigated. This study fills this gap and illuminates the changes of the electronic structures of the *meso*-C_6F_5-substituted chlorins and bacteriochlorins upon chromene-annulation, including a comparison of the various regio- and stereo-isomers, using optical, electrochemical, and computational data. We thus contribute to the further understanding of the class of synthetic *meso*-aryl-substituted bacteriochlorins and the scopes and limits of the degree to which their electronic structures can be tuned by chromene-annulation.

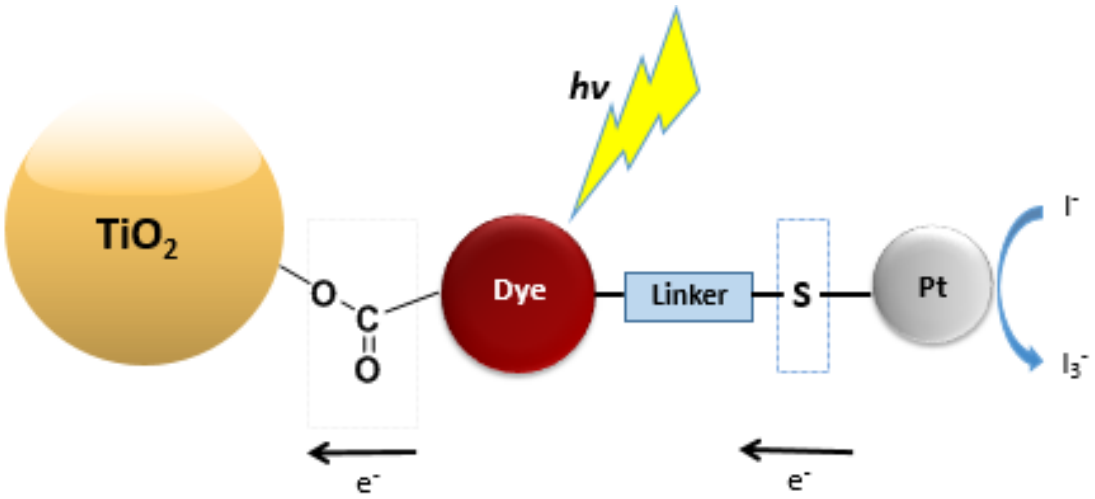

Figure 1-1. Scheme of a bifunctional dye that binds to TiO_2 through a carboxyl group and binds via a thiol linkage to a Pt nanoparticle, which catalyzes the reduction of the oxidized dye by iodide

1.2 Overview

Chapter 2 introduces the background and principle, major material components and current challenges of DSC. The specific experimental techniques, device fabrication and characterization are detailed in Chapter 3. The first objective will be explained in details in Chapters 4 and 5, which have the goal of building novel catalytic nanoassemblies, consisting of semiconductor—bifunctional molecular chromophore—metal nanoparticle, in order to catalyze the critical dye regeneration reaction in DSC with iodide/triiodide electrolytes. By reducing the overpotential associated with that reaction, adding a catalytic nanoparticle at the bifunctional dye/electrolyte interface has the potential to greatly improve solar power conversion efficiency while retaining the cheap and otherwise favorable redox couple iodide/triiodide. Platinum nanoparticles have been selected as the catalyst in this investigation since they have a demonstrated ability to catalyze the

desired reaction and are stable in an iodide/triiodide electrolyte. A key step is demonstrating binding of the dye molecule to the Pt nanoparticles.

In Chapter 4, we detail the characterization of the binding between the molecule and the Pt, using 4-mercaptobenzoic acid (4-MBA) and lipoic acid as models for a bifunctional dye having both a carboxyl group for anchoring to TiO_2 and a thiol or disulfide group for attachment to Pt. However, these model molecules lack the chromophore functionality and are not dyes. The three principal characterization techniques are cyclic voltammetry (CV), Raman spectroscopy, and X-ray photoelectron spectroscopy (XPS). In aqueous CV, currents for reduction and oxidation of the potassium ferrocyanide/ferricyanide redox couple on a Pt working electrode are sharply decreased when the Pt is previously exposed to 4-MBA, indicating bonding of 4-MBA to the Pt surface. The absence of the S–H stretching vibrational mode in Raman spectra of 4-MBA-modified Pt nanoparticles implies that the molecules are sulfur-bonded to the nanoparticle surface. High-resolution XPS studies of S and Pt core electrons show clear changes in binding energies when 4-MBA and Pt nanoparticles are brought together, suggesting the formation of S–Pt bonds. By contrast, these signals are not present for lipoic acid, indicating that lipoic acid cannot attach to the Pt via the formation of a Pt–S bond. Then a model assembly system, TiO_2-4MBA-Pt, is built in Chapter 5 and its catalytic performance is further investigated. In addition, results of the characterizations and device fabrications with sulfur-bearing ligands and complete bifunctional Ru-complex dyes will also be presented in Chapter 5.

In Chapter 6, we demonstrate that neither of the substitutions on T^FPP derivatives have an effect on the electronic properties of the porphyrin. By experimental determination of their optical properties (absorption and emission spectroscopy) and their frontier orbital positions by cyclic voltammetry, we determine the minimal electronic influence this derivatization method has on the

chromophore. However, these porphyrin derivatives are still likely ill-suited as efficient dyes in DSCs.

Also, in Chapter 7, we demonstrate that limited electronic modulations can be tuned through chromene-annulation, with the comparison of the experimental determination of their optical properties and electrochemical properties examined by absorption and fluorescence spectroscopy and cyclic voltammetry, respectively. And small modulations of the frontier orbitals of the porphyrinoids are rationalized using a collaborator's DFT computations and can be traced to small electronic effects due to the co-planarized *meso*-aryl groups in combination with conformational effects.

CHAPTER 2. BACKGROUND

2.1 Solar Energy

The sun is the central star of our solar system, which is 330,000 times more massive than the Earth. At its core, the sun is 15 million degrees Celsius, which releases tiny packets of energy called photons. Photons travel 150 million kilometers from the sun to Earth in about 8.5 minutes, at the speed of light, or 186,000 miles per second, or 3.0×10^8 meters per second. The sun offers a considerable amount of power: about 885 million terawatt-hours (TWh) reach the earth's surface in a year and will not run out for the next 5 billion years. That makes it a renewable resource. Other renewable resources like wind and water, can also provide us with energy. But even all the energy we can get from all these resources added together is still less than 1% of the solar energy reaching the earth (Figure 2-1). Therefore, it is clear that the potential of solar energy outshines its competitors.

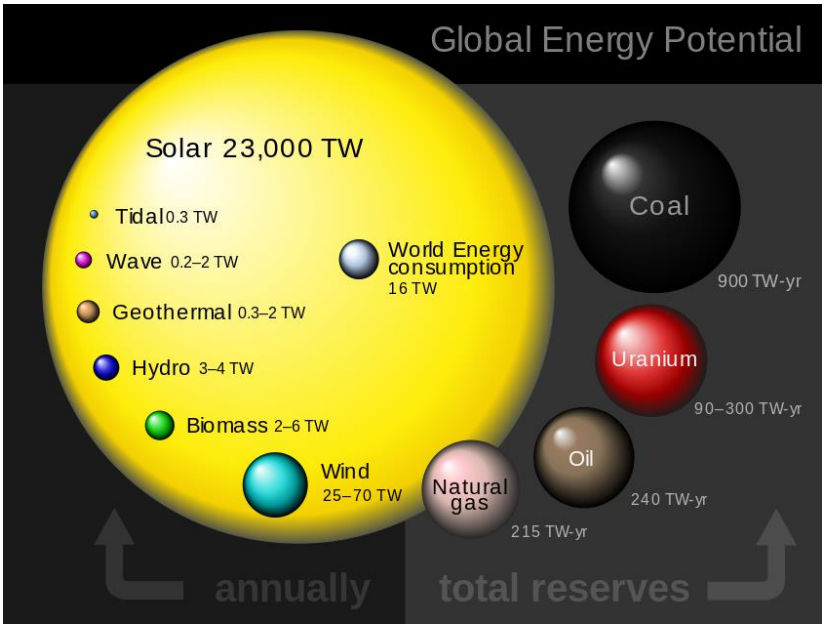

Figure 2-1. Global energy potential of various energy sources [5]

Today, people use solar energy to heat buildings and water and to generate electricity. However, solar energy only accounts for a very small percentage (less than 1%) of total world energy consumption (Figure 2-2).[6]

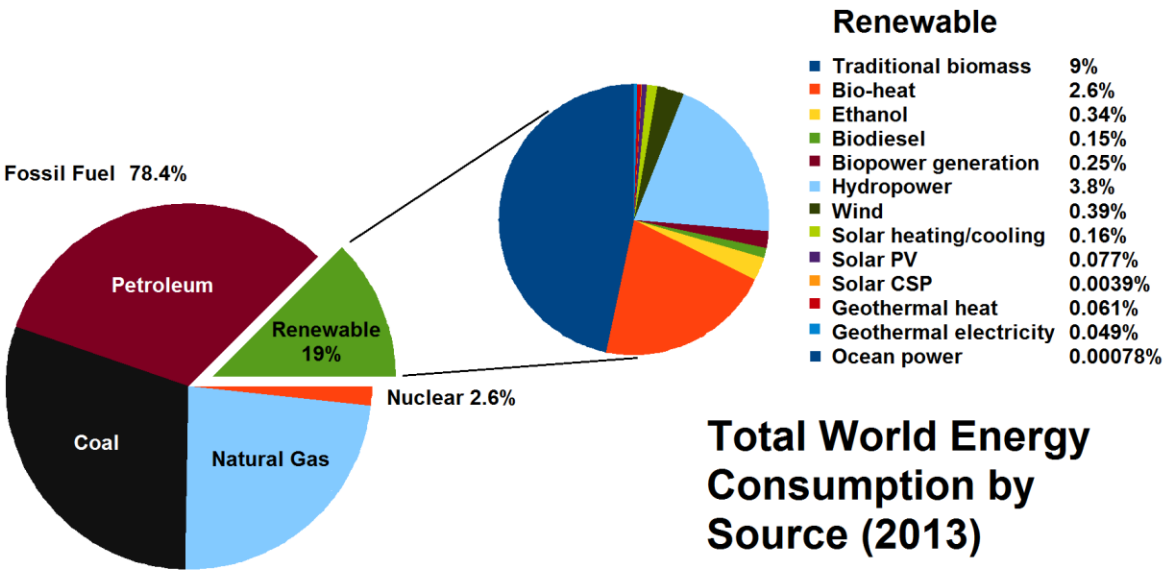

Figure 2-2. Total world energy consumption by source (2013)[6] (from REN21 Renewables 2014 Global Status Report)

2.2 Photovoltaic Devices

Photovoltaic (PV) cells are devices that can convert solar energy directly into electricity. The efficiency, the ratio of electric output over the incoming solar energy, is usually given in "standard" conditions, which specifies an external temperature of 25 ℃ and an irradiance of 1000 W/m^2 with an air mass 1.5 (AM 1.5, the relative path length of the direct solar beam through the atmosphere at the angle of 48° of the sum from the vertical)[7] spectrum. The first photovoltaic device was created in 1954,[8] when scientists in Bell Labs discovered that an array of several strips of silicon can produce electrical current when exposed to sunlight. The solar power efficiency was only 6%

at the very beginning. With decades of research, solar cell can basically be classified into mainly three generations (Figure 2-3).[9, 10]

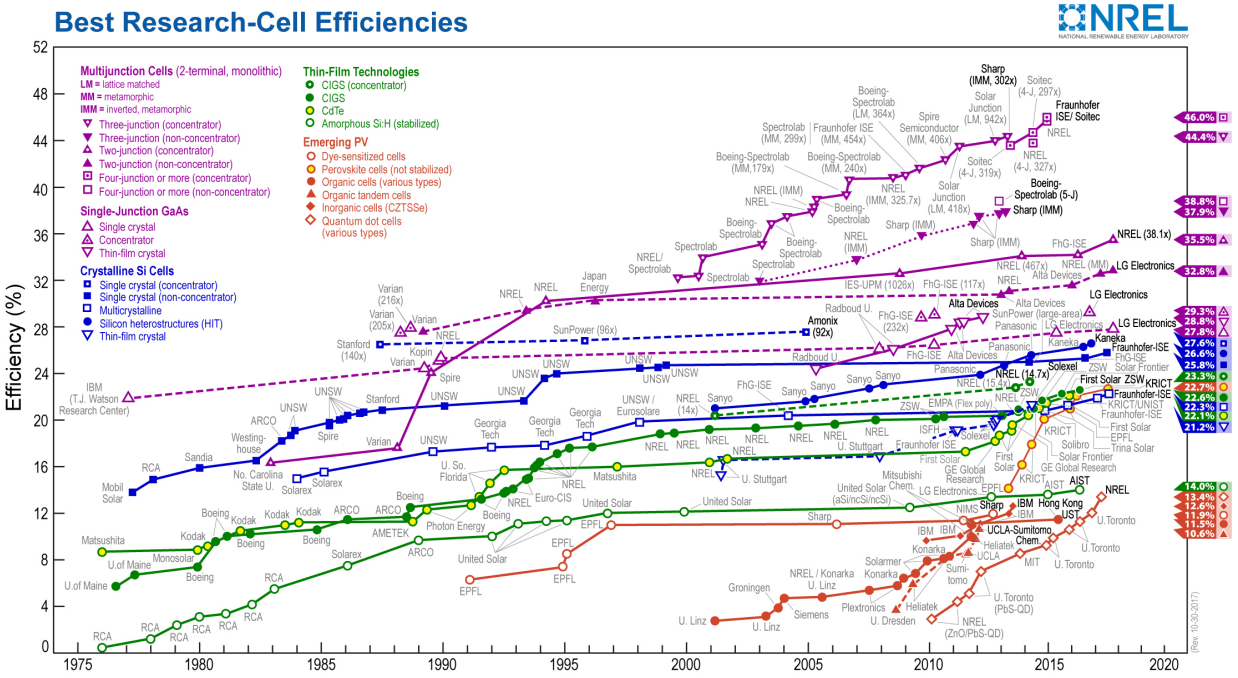

Figure 2-3. Summarized efficiencies of certified best performance PV devices in laboratory by year and solar cell type (from the National Renewable Energy Laboratory)

The first generation PV technologies are wafer-based crystalline silicon (c-Si), including single-crystalline (sc-Si) and multi-crystalline (mc-Si), which currently dominate the market with a share of over 90%.[11] Up to now, crystalline silicon PV cells have laboratory energy conversion efficiencies over 25% for single-crystalline Si cells and over 22% for multi-crystalline Si cells under standard test conditions. With a majority guaranteed life-time of 25 to 30 years at a degradation rate of 0.5% per year, the efficiency of crystalline silicon solar modules produced industrially could currently achieve at the range of 18% to 22%. Although c-Si solar cells represent a mature PV technology, they have their disadvantages, especially the high cost for

commercialization, since the silicon substrate requires high purity and should be thick enough to absorb enough sunlight.

The second generation PV technologies are based on thin film technologies, which can be classified into three primary types depending on the material used: copper indium gallium deselenide (CIS/CIGS), cadmium-telluride (CdTe) and amorphous silicon (a-Si). CIGS has a current laboratory conversion efficiency record that stands at 22.3%. They have high efficiency, and can be made using either glass or flexible materials as substrates. But since these cells traditionally have been more costly than other type of solar cells on the market, they are not widely used. CdTe based solar cells are the most commonly commercialized type of thin film solar cells because of their low cost manufacturing. They have reached around 22% efficiency in laboratory settings. However, the use of cadmium, highly toxic and an environmental hazard, can accumulate in plant and animal tissue, which often raises concerns. A-Si solar cells are a mature technology with a peak recorded efficiency of 14.0%. Even though most of the second generation solar cells show record efficiencies more than 20% in the laboratory, they only perform efficiencies in the 8% to 14% range in industry.

The third generation solar cells include multijunction cells and emerging PVs shown in NREL chart (Figure 2-3). They are photovoltaic devices that are potentially able to overcome the Shockley-Queisser limit of a maximum efficiency of 30% for an energy gap of 1.1 eV. Up till now, multijunction cells exhibit an obviously highest efficiencies compare to other types of solar cells. The emerging PV technologies are appeared more recently with efficiencies in the range of 10.6% to 22.7%. Most of the third generation solar cells are still in the research stage.

2.3 Dye-Sensitized Solar Cells

2.3.1 Background

DSC is considered to be a technology in between of the second generation and the third generation solar cells, which has the potential to become the third generation technology. It has some advantages such as being environmentally friendly, easy fabrication, low-cost manufacturing and compatibility with lightweight and flexible substrates. Besides, it also offers some other attractions for commercialization.[12, 13] For example, it can be designed as selected colors, semi-transparent or transparent, which makes it a good candidate for decoration, building-integrated applications, and other consumer products. It exhibits a good performance under diffuse light and high temperatures, which is a competitive advantage than other solar cell technologies under real outdoor conditions. In addition, it could also be made bifacially in order to capture light from all angles.

However, the low solar-to-electrical power conversion efficiency and stability, compared with other types of photovoltaic solar cells, have remained the major challenges for DSCs.[14]

2.3.2 Operation Principle of DSCs

A schematic diagram of a DSC showing the principle by which the device operates is shown in Figure 2-4. A DSC device contains three essential components: a semiconductor film, deposited on a conducting glass substrate (usually glass coated with a thin layer of fluorine-doped tin oxide, FTO), coated with a monolayer of dye molecules; a platinized counter electrode; and an electrolyte containing a redox mediator (e.g., the iodide/triiodide redox couple), filling the gap between the two electrodes.

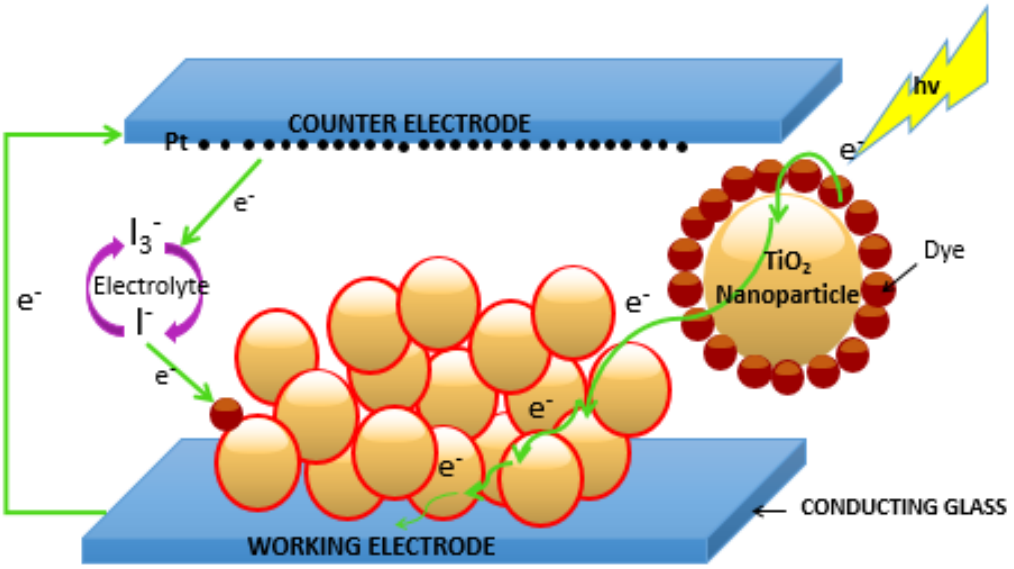

Figure 2-4. Schematic diagram of a DSC with the electron pathways

The operating principles are as follows: first of all, under illumination, a dye molecule (D) absorbs a photon of visible light, leading to the excited state (D*).

$$D + hv \rightarrow D^{*} \quad (2.1)$$

The excited electron injects into the conduction band of the semiconductor, leaving the dye in the oxidized state (D^{+}).

$$D^{*} \rightarrow D^{+} + e^{-} (TiO_2) \quad (2.2)$$

Then the iodide reduces D^{+} back to D and becomes I_3^{-}.

$$2D^{+} + 3I^{-} \rightarrow 2D + I_3^{-} \quad (2.3)$$

Lastly, electrons would recombine with triiodide in the electrolyte to complete the circuit.

$$I_3^{-} + 2e^{-} (Pt) \rightarrow 3I^{-} \quad (2.4)$$

2.3.3 Electron Transfer Process

The basic electron transfer processes in each component of the device are shown in Figure 2-5. Processes 1, 2, 3, and 4 are the desired pathway of the electron transfer. It starts by the electrons that are excited from the highest occupied molecular orbital (HOMO) to the lowest unoccupied molecular orbital (LUMO) of the dye sensitizer (process 1). This is followed by injecting an electron into the conduction band of the semiconductor (process 2), which induces the energetic increase of the Fermi level (E_F) to the quasi-Fermi level ($_nE_F$). Then the injected electrons transport through the semiconductor network (process 3) and are cycled by an external load to the platinized counter electrode to reduce the electrolyte. Then, the dye can be regenerated by the redox couple in the electrolyte (process 4) to complete the circuit.

Meanwhile, however, three main undesirable recombination processes also happen (shown in Figure 2-5 in red). Process 5 is the direct recombination between the excited state and the ground state of the dye sensitizer. Process 6 and 7 indicate the recombination of injected electrons in the semiconductor with either the oxidized dye or the acceptors of the redox mediator in the electrolyte, respectively.

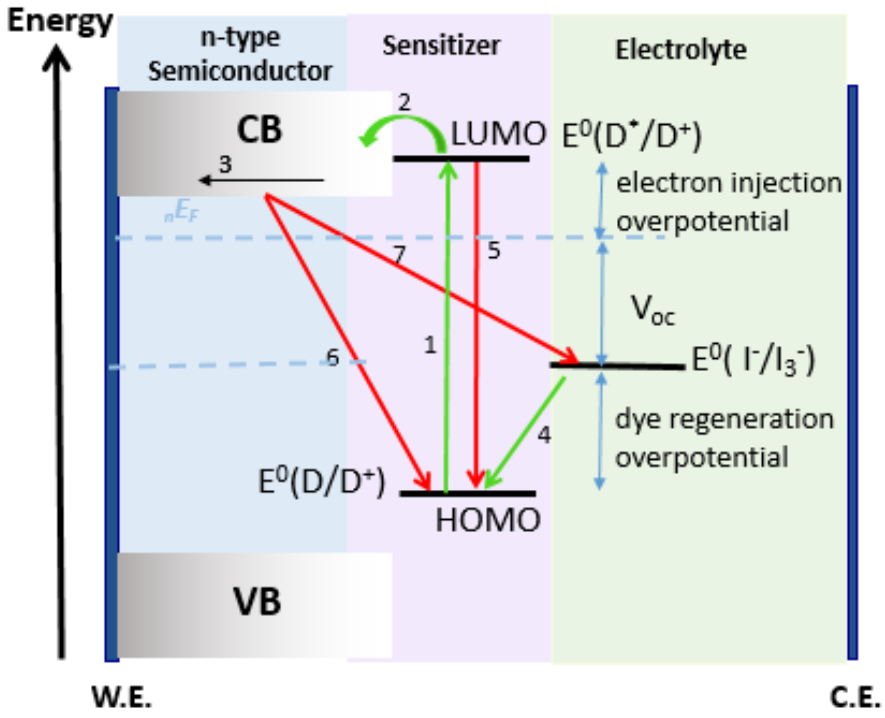

Figure 2-5. Energy structure of a DSC with the electron transfer processes

Usually, in a good DSC device, such as Ru-dye-sensitized solar cells with iodide/triiodide electrolyte, a fast electron injection and dye regeneration time constants under standard conditions are expected, whereas the recombination rate should be comparably slow (Figure 2-6).[15]

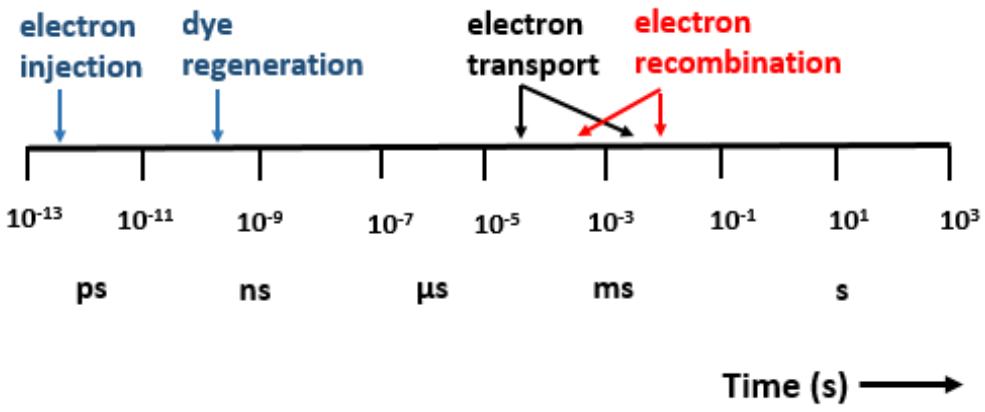

Figure 2-6. Summary of the kinetics in a DSC[15]

2.3.4 Iodide/Triiodide Electrolyte

The redox couple is very important in a DSC system. On one hand, it must regenerate the oxidized dye to its neutral state, and diffuse to the platinized counter electrode and be reduced from the formed oxidized species. On the other hand, the redox couple sets the electrochemical potential at the counter electrode and also affects the recombination kinetics between the conduction-band electrons in TiO_2 and the oxidized redox species.[16]

Among different redox couples used in a DSC, iodide/triiodide is mostly ideal. It has suitable redox potential, has good solubility in multiple solvents, does not absorb too much visible light and provides rapid dye regeneration. Besides, due to the small size, it allows fast mass transport. Most importantly, iodide/triiodide redox couple has very slow recombination kinetics between electrons in TiO_2 and the oxidized species of the redox couple, triiodide.[16]

However, iodide/triiodide results in significant electrochemical energy loss. The standard electrochemical potential of iodide/triiodide redox couple is +0.35 V vs NHE.[16] The oxidation potential of the common DSC sensitizer N719 is +0.97 V vs NHE.[17] The electrochemical overpotential between the oxidized dye N719 and the iodide/triiodide couple is as large as 0.62 V vs NHE.

While the regeneration of oxidized dye by iodide is not a simple one-step reaction, the result is a loss of about 0.5 V – 0.6 V due to the formation of a mediator, diiodide radicals ($I_2^{-\cdot}$), which brings the largest internal potential loss in DSC.

The reactions are listed below:[16]

$$D^* \rightarrow D^+ + e^- (TiO_2) \quad (1)$$

$$D^+ + I^- \rightarrow (D \cdots I) \quad (2)$$

$$(D \cdots I) + I^- \rightarrow D + I_2^{-\cdot} \quad (3)$$

$$2\, I_2^{-\cdot} \rightarrow I_3^- + I^- \quad (4)$$

Several alternative redox couples (electrochemical potentials are shown in Figure 2-7) have also been developed, all with their advantages and disadvantages. For example, cobalt redox couple has a good kinetics of electron transfer, but much lower long-term stability compared to the iodide/triiodide redox couple.[18, 19, 20] Ferrocene/ferrocenium has a more positive redox potential than the iodide/triiodide redox couple, but higher recombination rates.[21] Organic system electrolytes, such as disulfide/thiolate (T_2/T^-), have mass-transport limitations as well as chemical stability problems.[22, 23] Therefore, in our work, we are trying to solve the one big problem with the most common and unexpensive iodide/triiodide redox couple to enable it to reach high efficiencies.

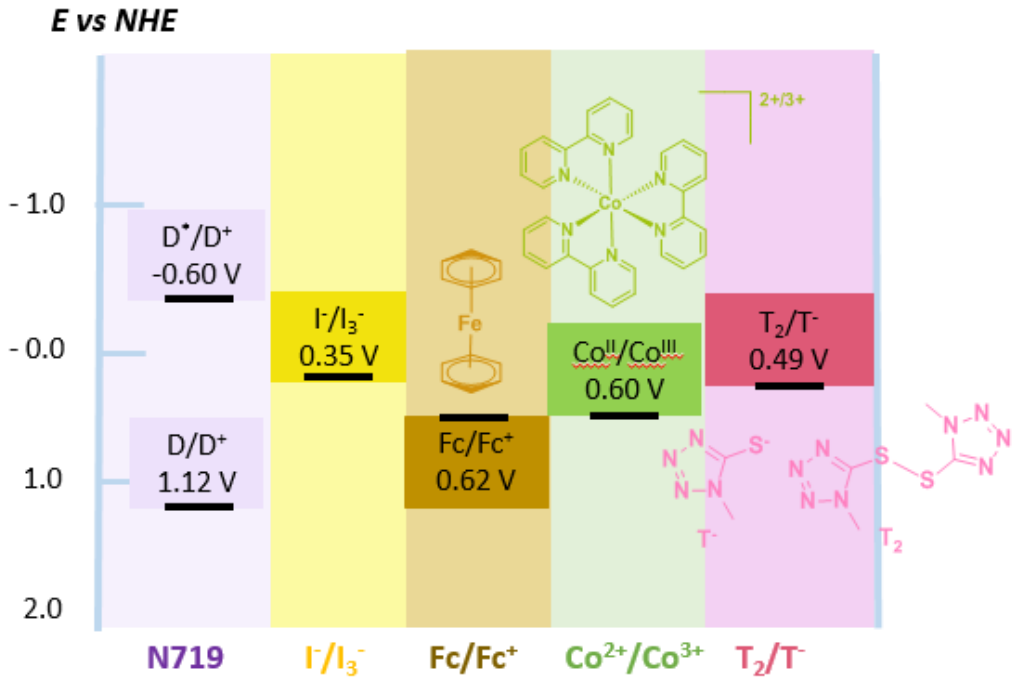

Figure 2-7. Comparison of electrochemical potential between different electrolytes

2.3.5 Sensitizers

As one of the most crucial parts in a dye-sensitized solar cell, the photosensitizer should fulfill some essential properties as follows:

(1) An absorption spectrum of a photosensitizer should cover the whole visible region and even part of the near-infrared.

(2) A photosensitizer should be photochemically and electrochemically stable.

(3) A photosensitizer should have functional groups, such as –COOH, -SO_3H –$P(O)(OH)_2$, etc., that can strongly bind to the semiconductor surface for a fast electron transfer.

(4) Proper energy levels of the photosensitizer are required. The HOMO level of the photosensitizer has to be more positive than the redox potential of electrolyte for dye regeneration, whereas the LUMO level of the photosensitizer must be more negative than the conduction band edge of the semiconductor for electron injection.

Ruthenium Complex Sensitizers. Different types of dye molecules have been designed for DSCs, such as, metal complexes and metal-free organic dyes,[24, 25, 26, 27, 28, 29] porphyrins and phthalocyanines dyes,[30, 31, 32, 33, 34] and quantum dots.[35, 36, 37] Among those, metal complexes, especially ruthenium (Ru(II)) complexes have attracted the most attentions due to their broad absorption spectra, relatively long excited-state lifetime and suitable energy levels.[24, 38, 39, 40, 41, 42, 43] For example, the ruthenium complex, *cis*-$RuL_2(NCS)_2$, known as N3 dye (Figure 2-8, left), with a solar power conversion efficiency of over 10%, shows good electrochemical stability, approximately 20 ns excited state lifetime and a broad light absorption range from ultraviolet to near-infrared light due to its metal to ligand charge transfer (MLCT). In addition, it also exhibits a strong binding on the semiconductor surface through the carboxyl groups.[13] Because of the above

advantages, N3 and another dye with its doubly deprotonated form, named N719 Figure 2-8, right), have been used as a basic structure for further design of other Ru dye molecules by changing the ancillary ligands in order to improve the efficiency of a DSC device or other applications.

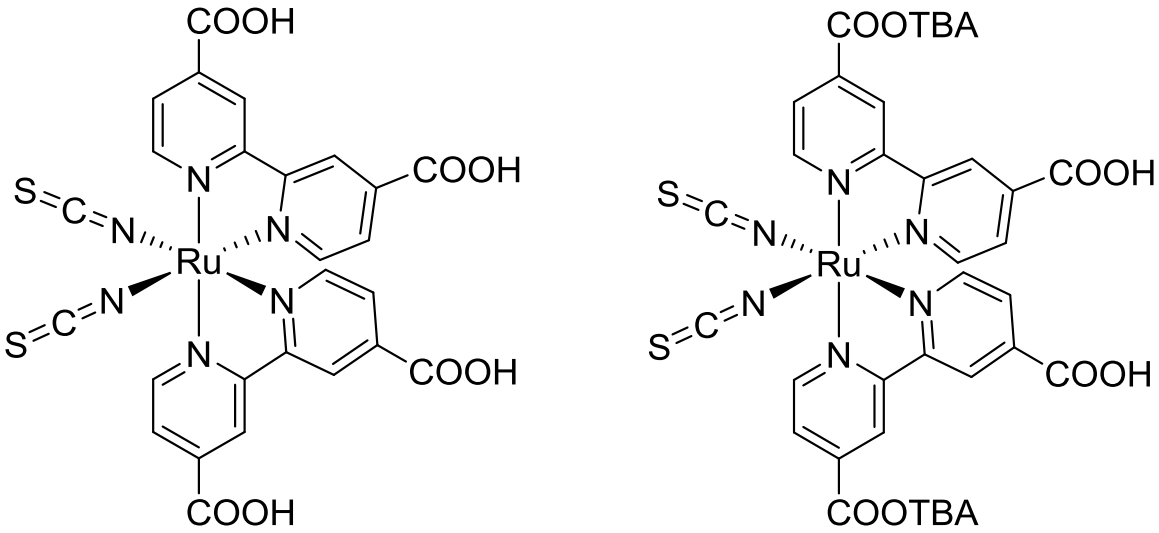

Figure 2-8. Molecule structures of dye (left) N3 and (right) N719, TBA = tetrabutylammonium

Porphyrin Sensitizers. Among different photosensitizers, porphyrin sensitizers have also been widely used in solar energy conversion.[33] Up to now, the best conversion efficiency has been obtained with a porphyrin sensitizer of 13% efficiency. The advantages of porphyrin derivative sensitizers are their rigid molecular structures with strong absorbing ability in visible range because of its highly π-conjugated systems, ease of synthesis and modification due to many reaction sites, i.e., four *meso* and eight β positions (shown in Figure 2-9), available for tuning photochemical and electrochemical properties.[48]

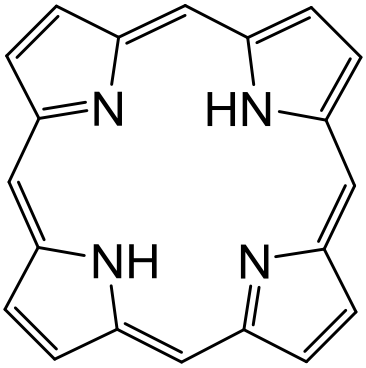

Figure 2-9. Typical structure of a porphyrin[48]

2.3.6 The Anchoring of the Dye on the Metal Oxide Surface

Anchoring groups are one or more chemical substituents on the dye molecules that can serve to enable their strong adsorption onto the TiO_2 or other metal oxide surface,[44] which play a crucial role in DSCs. An anchoring group influences the electron injection rate from the dye into the TiO_2 semiconductor, fixes the distance of the dye from the semiconductor surface, tunes the electrochemical properties of the dye, and also affects the aggregation of the chromophores.[45]

Anchoring to TiO_2 surface by different dye molecules has been achieved through a number of functional groups, such as carboxylic acid, phosphonic acid, salicylate and acetylacetonate derivatives.[45, 46] Among these functional groups, carboxylic acid is of the most common one. The major binding modes of carboxylate binding on a TiO_2 surface are shown in Figure 2-10.[13, 47]

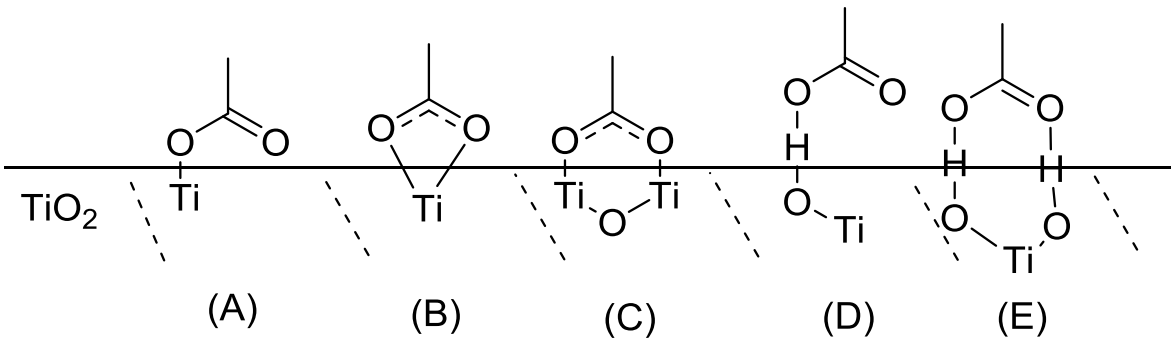

Figure 2-10. Binding modes for the carboxylate unit on TiO_2 surface. (A) unidentate; (B) bidendate chelating; (C) bidentate bridging; (D) and (E) H-bonded[13]

2.3.7 Challenges in Improving Efficiency

Extensive work has been done to improve the DSC efficiency by modifying dye molecules,[26, 27, 29, 48] electrolytes[49] and hole conductors, developing and optimizing the semiconductors for working electrode and counter electrode.[50, 51] The maximum theoretical efficiency of DSC has been estimated to be 32%.[52] However, with the development of DSC for over 20 years, the record efficiency so far is only above 14%.[4] One main deviation is due to the limited light-harvesting region of dyes. Another deviation from its limit of the standard cell with iodide/triiodide electrolyte is due to the large overpotential of dye regeneration, which refer to the driving force for electron to regenerate the oxidized dye from the electrolyte redox mediator shown in Figure 2-5, respectively.

Metal complexes, especially the most popular ruthenium (Ru(II)) complexes, such as N3, N719, and Z907, contain a central metal along with ancillary ligands that include at least one anchoring group.[13] Due to metal to ligand charge transfer, these complexes exhibit a broad absorption range in the visible light spectrum. However, their molar extinction coefficients are relatively low (5,000

– 20,000 $M^{-1}cm^{-1}$) and possess a limited absorption in the near-infrared region of the solar spectrum.[13, 14] While, organic dyes, which have been considered as an alternative to Ru complexes show molar extinction coefficients (50,000 – 200,000 $M^{-1}cm^{-1}$) higher than those of Ru-based complexes, they have shorter excited state emission lifetimes and narrower spectral band widths.[53, 54] Porphyrin and phthalocyanine systems, on the other hand, provide strong absorption in the near-IR region and outstanding photoelectrochemical properties, which makes them good candidates for photovoltaic devices. However, some of those phthalocyanine dyes have solubility issues and a strong tendency of aggregation. Co-sensitization systems have been developed as sensitizers in DSCs, in order to complement the absorption spectra of each dye and therefore increase light absorption range. Such systems have been investigated, for instance co-sensitization between two organic dyes,[55, 56] Ru-complex and organic dyes,[57, 58, 59] porphyrin or phthalocyamine and organic dyes.[60, 61, 62] Up till now, the record efficiency of a DSC device of 14% efficiency is obtained by a co-photosensitizer system with a silyl-anchored dye **ADEKA-1** and a carboxy-anchored organic dye **LEG4** (Figure 2-11).[4] However, dye aggregation problems might result from the co-sensitization system.[63]

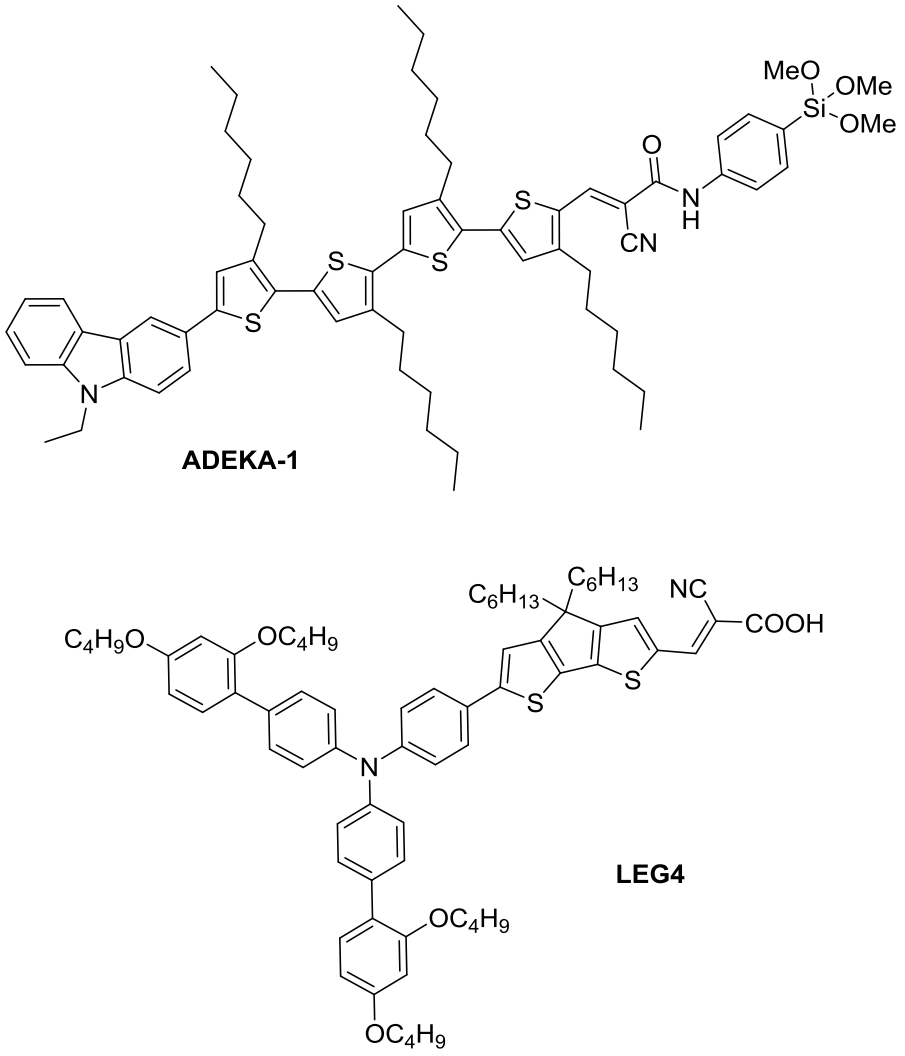

Figure 2-11. Molecular structures of silyl-anchor **ADEKA-1** and carboxy-anchor **LEG4** dyes[4]

The redox mediator is one of the most important factors that effects the overpotential and the energy loss within a DSC system. Especially, the open circuit voltage (V_{oc}) is highly dependent on the electrochemical potential of the redox couple in the electrolyte. Although iodide/triode redox couple shows a remarkable performance in DSC, they create a large dye regeneration overpotential. Therefore, numerous research has been developed to enlarge the open circuit voltage or/and decrease the overpotential of electron injection and dye regeneration processes by

investigating more positive redox couples, utilizing additives in the electrolyte, optimizing the counter electrode, designing the nanostructured semiconductors and its corresponding dye sensitizers to achieve low electron injection overpotential and fast electron transportation.[64, 65, 66, 67]

In this thesis, two routes will be described to improve the efficiency of a DSC. One way is to reduce the energy loss in redox reactions by using platinum nanoparticles as catalysts. This involves the synthesis of Pt nanoparticles, coupling of N3-type bifunctional dyes, with a thiol group and a carboxyl group, to Pt and to TiO_2, respectively, and characterization of resulting devices. This is discussed in Chapter 4 and Chapter 5. The second route involves modifying strongly light-harvesting porphyrinoid dye molecules to work as dyes in DSC devices. This requires the characterization of redox and optical properties of different porphyrinoid dyes and chemical modification to allow attachment to TiO_2 nanoparticles. This will be future discussed in Chapter 6 and Chapter 7.

CHAPTER 3. MATERIALS AND METHODS

3.1 Substrate

A transparent conducting oxide (TCO) is commonly used as substrate electrodes in a DSC device to serve as collector for the photogenerated current. In this work, fluorine-doped tin oxide (FTO)-coated glass was purchased from Hartford Glass Co (USA) as a conductive substrate, which has transmission of over 80% in the visible spectrum and a sheet resistance of 8 Ω/square. The FTO substrate was cleaned sequentially with detergent, DI water, and ethanol by sonicating for 5 min in each step.

3.2 Processing of Mesoporous TiO_2 Films

The TiO_2 nanoparticles were bought from Dyesol with a particle size of 18 nm. It was diluted with (+)/(-) terpineol with a 1 to 0.8 mass ratio to make a TiO_2 paste. A typical mesoporous TiO_2 film was made by the doctor blading technique. A piece of Scotch tape with a punched hole is placed on the substrate, and a drop of the TiO_2 paste is smoothed over the hole with a glass rod. The tape is removed and the sample is sintered at 500 ℃ for 30 min (according to the temperature program in Table 3-1) in order to remove the organic components and to establish sufficient interparticle contacts between the TiO_2 nanoparticle networks. This resulted in TiO_2 nanoparticle films with a thickness of 6 to 8 μm.

Table 3-1. Sintering program of TiO_2 film

	Step 1	Step 2	Step 3	Step 4	Step 5
Ramping Time (min)	5	5	5	5	5
Temperature (℃)	125	250	375	450	500
Holding Time (min)	5	5	5	15	30

3.3 $TiCl_4$ Post-Treatment

A post-treatment with $TiCl_4$ was applied to freshly sintered doctor-bladed TiO_2 films.[68] A solution of 40 mM aqueous $TiCl_4$ was diluted from a stock solution of 2 M $TiCl_4$. Sintered TiO_2 films were immersed into this solution and heated in an oven at 70 ℃ for 30 min inside a closed glass petri dish. The electrodes were sintered again at 500 ℃ for 30 min after flushing with DI water and dried in air. The profile and the thickness of the films were measured using a Dektak 150 stylus profilometer.

3.4 Sensitization

N719 is one of the standard sensitizers for DSC devices. The TiO_2 films were immersed in a 0.3 mM ethanolic N719 dye solution overnight for chemical attachment, followed by rinsing with ethanol to remove physisorbed dye. The structure of N719 is given in Figure 2-8.

3.5 Preparation of Counter Electrode

Counter electrodes were made by thermal decomposition of a platinum precursor of 5 mM $H_2PtCl_6 \cdot 6H_2O$ in isopropanol. First of all, two holes for electrolyte injection were drilled through the FTO substrate using a Dremel 200 with a diamond drill bit. Then two drops of platinum precursor solution were spread in the middle of the two holes. Finally, after it had dried, the substrate was heated at 400 ℃ for 30 min to decompose the Pt precursor into Pt metal nanoparticles, resulting in the platinized counter electrode.

3.6 Electrolyte Composition

The iodide/triiodide electrolyte was prepared was prepared with 1 M 1,3-dimethylimidazolium iodide, 50 mM LiI, 30 mM I_2, 0.5 M *tert*-butylpridine, and 0.1 M guanidinium thiocyanate in acetonitrile. EL-HSE high stability electrolyte, purchased from Dyesol, was also used in some experiments.

3.7 Solar Cell Fabrication

The photoanode working electrode was sealed against with the platinized counter electrode on a hot plate at 120 ℃ using a 25 μm-thick Surlyn frame, which melts at a temperature over 100 ℃. The electrolyte was then injected through one of the two holes in the counter electrode, while the inside air exit from the other. Both holes were sealed with Surlyn and a piece of microscope glass. At last, the edge of each electrode was coated with copper tape for a better electrical contact. The schematic is shown in Figure 3-1.

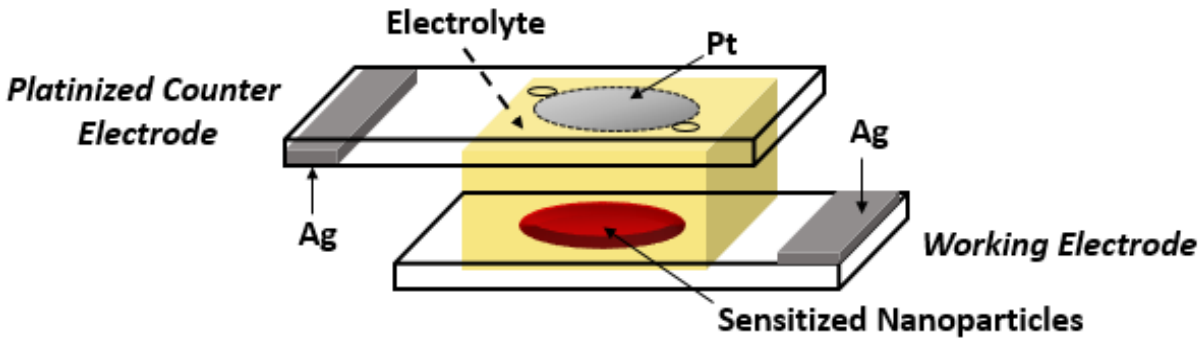

Figure 3-1. Schematic of a DSC including FTO glass coated with sensitized semiconductor nanoparticles, a platinized counter electrode and liquid electrolyte in between

3.8 Solar Cell Characterization

The current density–voltage (*J*–*V*) of a DSC device was measured at standard test conditions of AM 1.5G simulated sunlight with a power of 1000 W/cm^2 (1 sun), produced by a solar simulator (Newport 91160) equipped with a 450 W Xenon lamp (Oriel, USA) and calibrated against a 1 cm^2 reference silicon solar cell with KG5 filter (PV Measurements, Inc., Boulder, CO). The measurement was controlled by a Keithley 2400 digital source meter. The DSC active area was 0.28 cm^2.

CHAPTER 4. ATTACHMENT OF PLATINUM NANOPARTICLES TO A METAL OXIDE SURFACE USING A THIOL-CARBOXYL BIFUNCTIONAL MOLECULE

4.1 Introduction

A variety of assemblies of metallic nanoparticles bound to molecules have attracted intense research interest for electrocatalytic, sensing, biomedical, photovoltaic and other applications. Particular attention has been paid to Au–thiol assemblies.[69, 70, 71, 72] A number of reports have described experimental investigations by techniques such as surface-enhanced Raman scattering (SERS) together with theoretical descriptions generally by density functional theory (DFT) of thiols on Ag and Au substrates.[73, 74, 75, 76] X-ray photoelectron spectroscopy (XPS) has also been widely used in characterizing Au–S as well as other metal–S bondings.[72, 77, 78, 79, 80, 81, 82]

A number of applications of Pt–S couplings have been studied. Platinum nanoparticles (PtNPs) were tethered, via a molecule having sulfur-bearing moieties on both ends, to a gold electrode surface in order to electrocatalyze reduction of H_2O_2 as part of a nitrite sensor.[83] A modified self-assembled thiolipid monolayer (SAM) on platinum electrodes was used as an amperometric cholesterol biosensor.[84] A chemical modification scheme of metal–molecule–metal paves the way for various electronic applications, such as tailoring surface structure with variable terminal functional groups, film thickness and tuning the electronic properties of metal nanoparticles.[85, 86, 87, 88] In addition, Beebe et al. found that Pt forms a contact resistance two orders of magnitude lower than Au with self-assembled monolayers (SAMs) of alkanethiols.[85] The attachment of PtNPs

to dye molecules has been investigated for the reduction of overpotential losses in dye-sensitized solar cells (DSCs).[89]

However, while the Au–S coupling has been thoroughly characterized, there are fewer studies on Pt–S bonding,[90, 91] and only one that we are aware of in which a molecule with a thiol group and a carboxyl group was attached to Pt nanoparticles.[92] The carboxyl group opens a number of applications as it is widely used to couple molecules to various surfaces, especially metal oxides, which serve as inert catalyst supports and as functional materials for sensing and optoelectronic devices, solar cells, water splitting, etc. Dablemont et al. showed that the thiol group in ω-mercaptoundecanoic acid binds to Pt, and that using the carboxyl group on the other end of the molecule, they could attach Pt nanoparticles to an alumina surface.[92]

This study was motivated by preliminary results indicating that some of the initial molecules made by our collaborators, Ian Weiss and Elena Galoppini at Rutgers University-Newark, did not bind to Pt as expected. Those molecules included 4,4′-dimethyl-lipoate-2,2′-bipyridine (dmlb), and Ru complexes having dmlb as a ligand intended to attach the complex to Pt. The dmlb molecule contains a lipoic acid moiety, which includes a disulfide group. In this chapter, we characterized the binding of Pt to the sulfur-bearing molecules dmlb, lipoic acid, and 4-mercaptobenzoic acid (4-MBA) (see Figure 4-1) by Raman spectroscopy, cyclic voltammetry (CV) and X-ray photoelectron spectroscopy (XPS). Lipoic acid and 4-MBA serve as model bifunctional molecules able to couple to metal oxides via carboxyl groups and to Pt via sulfur atoms, in a disulfide group (lipoic acid) or a thiol (4-MBA). With the model compounds, we compared the abilities of these two sulfur-bearing groups to bind to Pt to guide the design of bifunctional dyes.

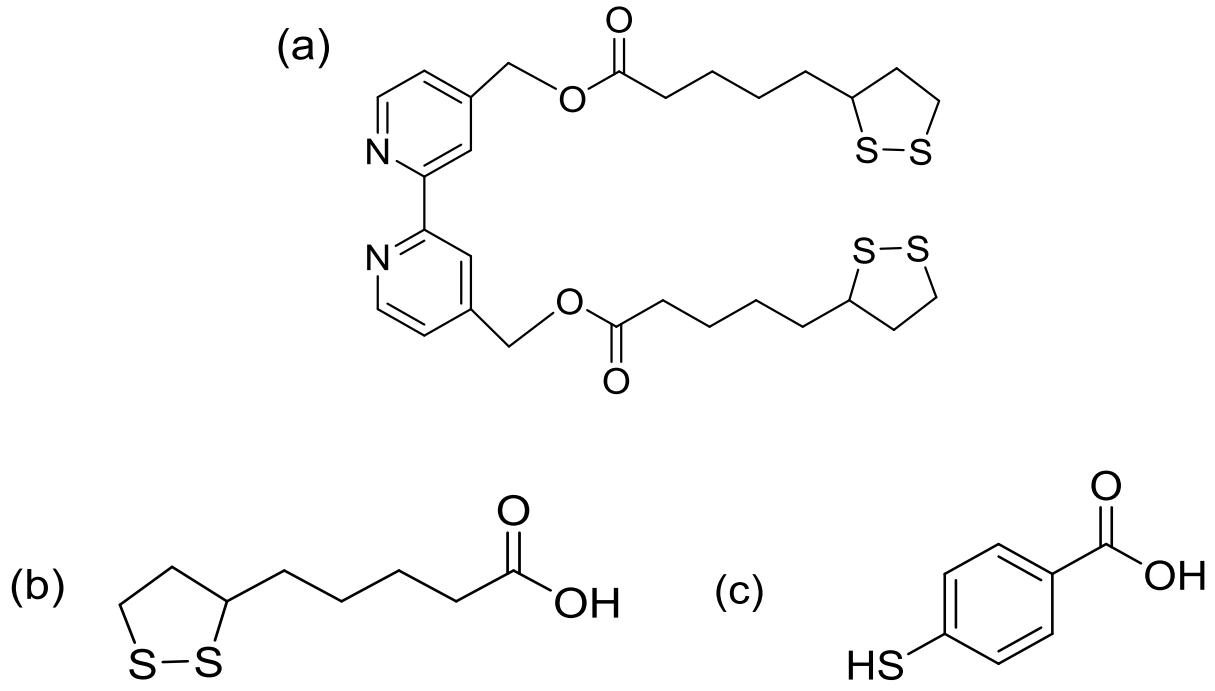

Figure 4-1. Molecule structures of (a) 4,4'-dimethyl-lipoate-2,2'-bipyridine (dmlb), (b) lipoic acid, (c) 4-mercaptobenzoic acid

4.2 Experimental

Materials. All chemicals were purchased from Sigma-Aldrich and were ACS grade or better, except F-doped SnO_2-coated glass (TEC-8, transmission > 80% in the visible spectrum; sheet resistance 8 Ω/sq) was purchased from Hartford Glass Co. The iodide/triiodide electrolyte was purchased from Dyesol (MS005616-10).

Cyclic Voltammetry. Platinum wire electrodes were cleaned by immersing them in aqueous 0.5 M H_2SO_4 and cycling the potential between -1.25 V and +1.2 V versus Ag/AgCl at a scan rate of 100 mV/s until reproducible scans were recorded (about 10-20 cycles). The Pt electrodes were

then removed from solution, rinsed with DI water and allowed to air-dry. The cleaned Pt electrode was immersed in a 1 mM solution of sulfur-bearing molecule in ethanol at room temperature for 3 days. The electrode was then rinsed with ethanol before use as a working electrode.

Cyclic voltammetry measurements were performed with a CHI 600D potentiostat with a three-electrode setup. Pt wires were used as both working and counter electrodes. The reference electrode was Ag/AgCl in a supporting electrolyte of aqueous 0.1 M KCl. The electrodes were immersed in the supporting electrolyte plus 1 mM potassium hexacyanoferrate, $K_3Fe(CN)_6$, and scanned at a rate of 100 mV/s.

Raman Spectroscopy. Platinum nanoparticles were synthesized according to a method by Wang et al.[93] A 50 mL 0.5 M ethylene glycol solution of NaOH was added dropwise to a 50 mL ethylene glycol solution containing 1.93 mmol $H_2PtCl_6 \cdot 6H_2O$, with constant stirring at 400 rpm. The mixture was heated at 160 ℃ for 3 hours, with nitrogen bubbling through the system to remove water, oxygen and any reaction byproducts. After the reaction, a transparent dark-brown homogeneous Pt nanoparticle colloidal suspension was obtained, without any precipitate. The pH of the Pt suspension was adjusted to 3 by adding 0.5 M HCl, inducing aggregation. The suspension was washed by centrifugation at 4000 rpm for 20 min, discarding the supernatant, and resuspension in ethanol. Clean PtNPs were recovered by another centrifugation and mixed with an equal volume of a 1 mM sulfur-bearing molecules in ethanol solution. The mixture was stirred 400 rpm overnight to allow coupling of the S atom to the PtNP surface. It was then centrifuged, refilled with ethanol, centrifuged again, resuspended in ethanol, and deposited on a piece of fluorine-doped tin oxide (FTO)-coated glass (which had been cleaned in a sonicator bath in detergent, DI water and ethanol, in that order), and dried in air at room temperature. This served as the sample for Raman spectra,

which were recorded with a Renishaw 2000 Ramanscope, with the excitation line of an Ar ion laser at 514 nm.

X-ray Photoelectron Spectroscopy (XPS). Nanoparticles of Pt were formed by depositing a solution of 5 mM $H_2PtCl_6 \cdot 6H_2O$ in 2-propanol on cleaned FTO glass followed by heating the sample at 400 °C in air.[94, 95, 96, 97] After cooling to room temperature, the platinized FTO was immersed in a 1 mM sulfur-bearing molecules in ethanol solution overnight. For comparison, another platinized FTO sample was immersed in pure ethanol.

XPS was carried out using a monochromatic Al Kα X-ray source, X-ray beam diameter 100 μm at 25 W, with automatic charge neutralization. The Pt peaks were fit with the $4f_{7/2}$ and $4f_{5/2}$ doublet constrained to have a 4:3 peak area ratio and a peak separation of 3.33 eV. The $2p_{3/2}$ and $2p_{1/2}$ doublet for S was constrained to have a 2:1 peak area ratio and a peak separation of 1.2 eV.

4.3 Results and Discussion

Cyclic voltammetry. The cyclic voltammogram of an unmodified Pt wire (Figure 4-2, black line) in an aqueous supporting electrolyte containing the reversibly reducible Fe(III) complex $K_3Fe(CN)_6$ (1 mM) shows reduction and oxidation peaks corresponding to the potassium ferrocyanide/ferricyanide redox couple. The anodic (E_{pa}) and cathodic (E_{pc}) peak potentials appear at 262 and 188 mV versus Ag/AgCl, respectively, and the half-potential ($E_{1/2}$) is 225 mV versus Ag/AgCl. According to the cyclic voltammograms in Figure 4-2 (blue and red lines), both dmlb and lipoic acid with disulfide groups have little effect on the reactions of ferrocyanide/ferricyanide on a Pt wire. This suggests that dmlb and lipoic acid do not bind to Pt.

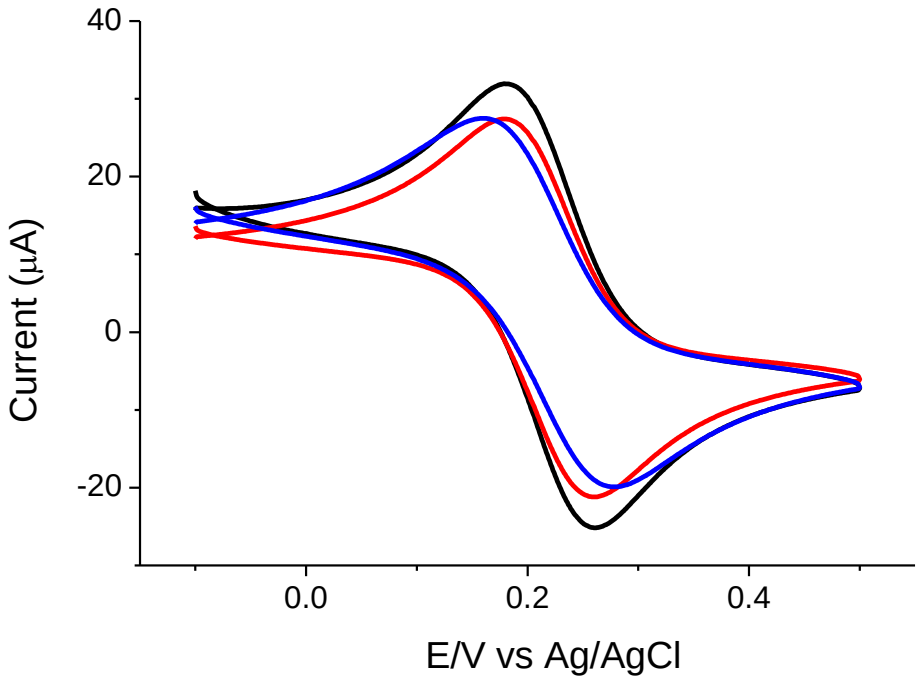

Figure 4-2. Cyclic voltammograms of (black) Pt wire; (red) lipoic acid modified Pt wire; (blue) dmlb modified Pt wire in 1 mM $K_3[Fe(CN)_6]$ in supporting electrolyte, scanned at 0.1 V/s

On the other hand, if the Pt electrode is modified with 4-MBA (Figure 4-3, red line), the oxidation and reduction peak currents are markedly decreased, by 30% - 40%. This decrease can be attributed to steric repulsion of the potassium ferrocyanide/ferricyanide redox couple from the Pt electrode surface due to Pt-bound 4-MBA molecules.

By contrast, a Pt wire modified with benzoic acid (Figure 4-3, blue line), which is analogous to 4-MBA but lacks the thiol moiety, gives a current nearly identical to that of an unmodified Pt electrode. This indicates that the carboxyl group common to benzoic acid and 4-MBA cannot bind to Pt, implying that 4-MBA bonds to the Pt by the SH groups.

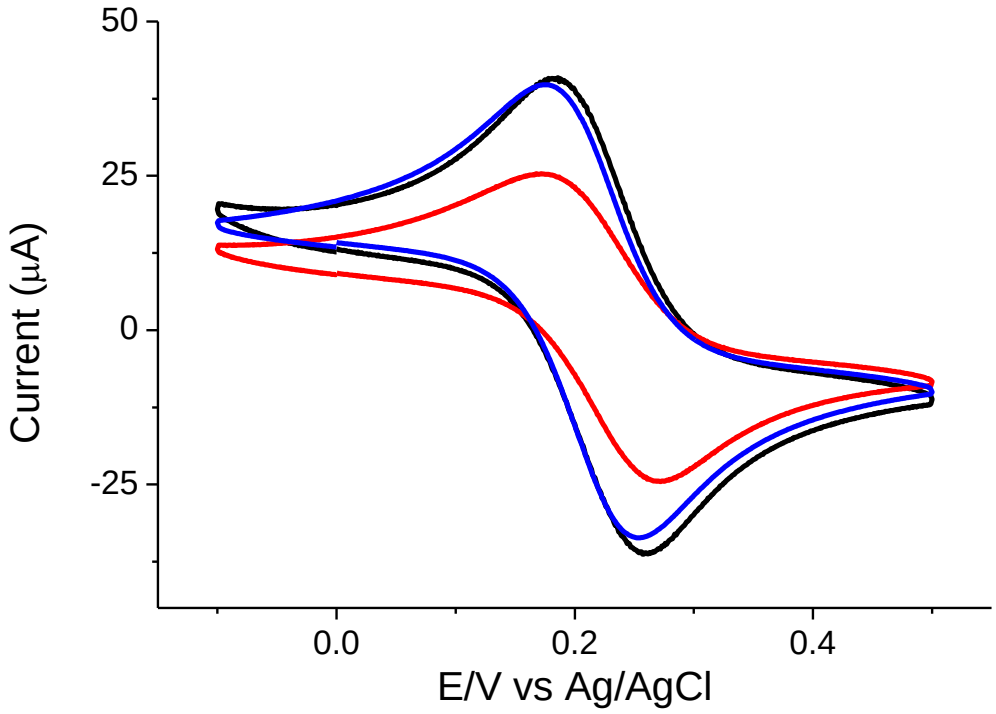

Figure 4-3. Cyclic voltammograms of (black) Pt wire; (red) 4-MBA modified Pt wire; (blue) benzoic acid modified Pt wire in supporting electrolyte containing 1 mM $K_3Fe(CN)_6$, scanned at 0.1 V/s

Raman spectroscopy. For disulfide, the vibrations observed at 430-550 cm^{-1} and 630-790 cm^{-1} are assigned as S-S, and C-S (aliphatic) stretching mode, respectively. In Figure 4-4 a and b, one S-S peak and two C-S peaks on lipoic acid as well as the dmlb can be detected, which show similar results compared to what Ikuta et al. obtained.[98] However, no peak can be observed after exposing these to disulfide molecules to Pt nanoparticles, as shown in Figure 4-5 a and c, indicating that the disulfide group is not binding to Pt. This result agrees with the cyclic voltammetry experiment described above.

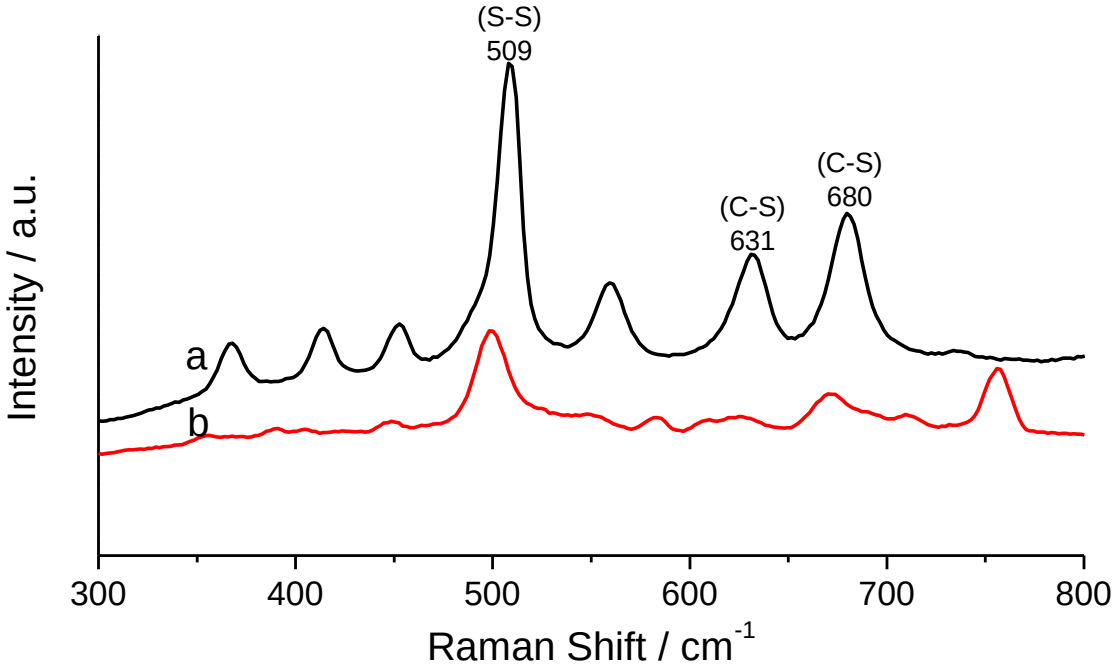

Figure 4-4. Raman spectra for (a) lipoic acid; (b) dmlb powder

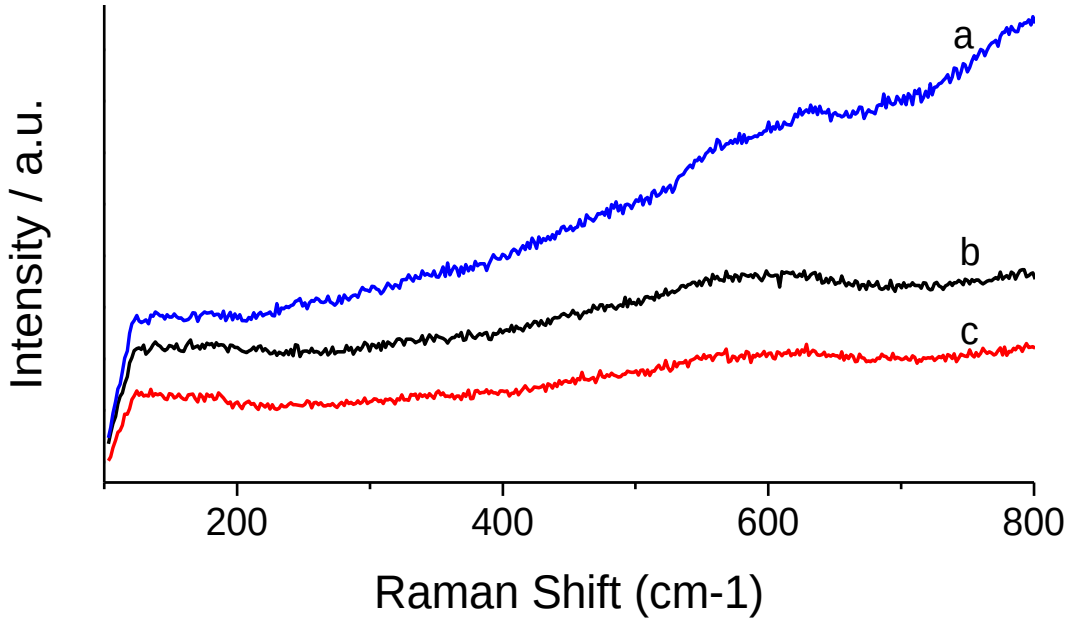

Figure 4-5. Raman spectra for (a) dmlb modified Pt; (b) Pt; (c) lipoic acid modified Pt

A Raman spectrum of 4-MBA powder, shown in Figure 4-6 b, shows two strong peaks at 1098 cm^{-1} and 1598 cm^{-1}, assigned to aromatic benzene ring breathing and stretching vibrational modes, respectively.[73, 99] The carboxyl group is responsible for the bands appearing at 803 cm^{-1}, 1409 cm^{-1} and 1624 cm^{-1}, corresponding to $–COO^-$ bending, and the symmetric stretching of $–COO^-$ and –C=O, respectively.[74, 100] The band at 908 cm^{-1} corresponds to the C–S–H bending vibration.[100, 101] A relatively strong band at 2566 cm^{-1} is assigned to the S–H stretching mode.[73, 74]

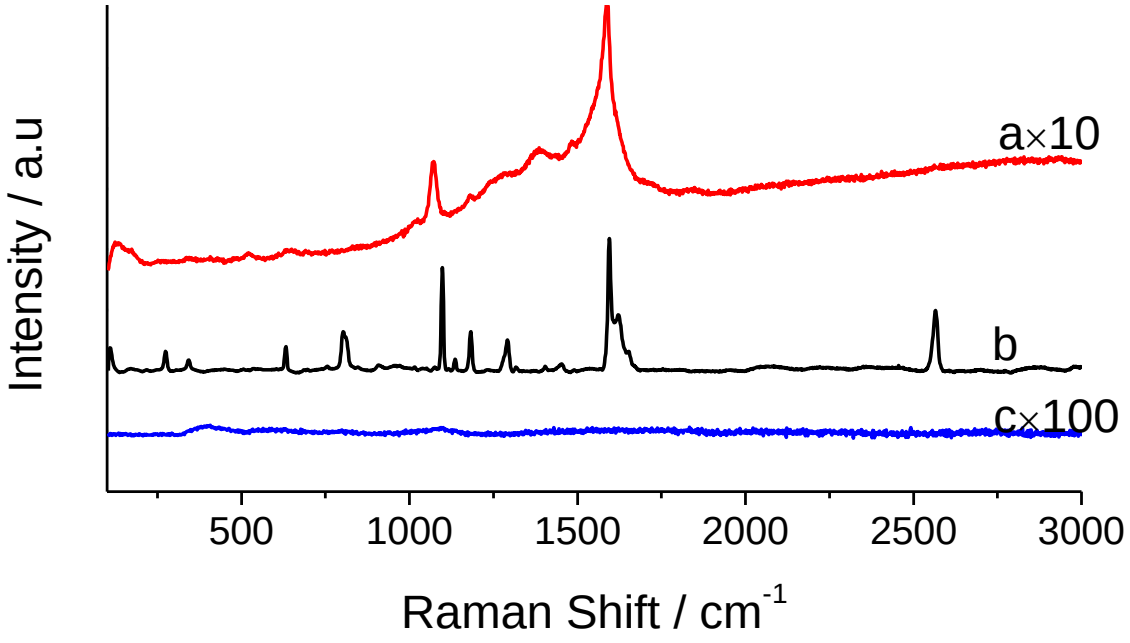

Figure 4-6. Raman baseline-corrected spectra for (a) 4-MBA modified Pt, (b) 4-MBA powder, and (c) Pt on FTO

Platinum nanoparticles were suspended in an ethanolic solution containing 1 mM 4-MBA, then centrifuged out and washed with ethanol. The Raman spectrum of these PtNPs (Figure 4-6a) displays signatures of the molecule 4-MBA. The principal peaks appear at 1071 cm^{-1} and 1588 cm^{-1}, assigned to the aromatic benzene ring breathing and stretching vibrational modes of 4-

MBA.[74, 100, 102] The small but clear bands observed at 524 cm^{-1}, 1290 cm^{-1} and 1485 cm^{-1} are assigned to the ring out of plane bending, the C–H in plane bending and aromatic ring bending, respectively.[99, 100] A shoulder at 1710 cm^{-1} is assigned to the stretching mode of C=O stretching mode, implying the presence of neutral –COOH groups.[73] None of these features appear in a Raman spectrum of PtNPs that were not exposed to 4-MBA (Figure 4-6 c).

Strong signals from the 4-MBA powder spectrum (Figure 4-6 b) that are notably absent from the PtNP/4-MBA spectrum (Figure 4-6 a) include the vibrational bands at 803 cm^{-1}, 908 cm^{-1} and 2566 cm^{-1}, which correspond to the bending mode of $–COO^-$, the C–S–H bending vibration and S–H stretching vibrational mode, respectively. These findings are consistent with 4-MBA that is bound to the PtNPs via the S atom, although they cannot rule out carboxylate binding.

X-ray Photoelectron Spectroscopy (XPS). X-ray photoelectron spectra were taken of a PtNP film formed on an FTO/glass substrate, as is or with adsorbed dmlb and lipoic acid, respectively (binding energy listed in Table 4-1).

From the sulfur perspective, lipoic acid powder itself has a doublet, 161.9 eV and 163.06 eV, which can be defined as S-S bond. After binding with Pt, an extra peak appears at 167.25 eV, which might be the S-Pt peak, but the present area is only 1.81%. The dmlb powder itself has three peaks, and no big differences after binding with Pt.

Table 4-1. Binding energy (eV) of the main XPS S 2p peaks

Sample	Disulfide, S-S		Sulfate
	S $2p_{3/2}$ (eV)	S $2p_{1/2}$ (eV)	S 2p (eV)
Lipoic acid powder	161.9 (49.47%)	163.06 (50.53%)	
dmlb powder	161.96 (30.18%)	162.83 (67.63%)	166.83 (2.20%)
Pt/lipoic acid	162.68 (61.27%)	163.79 (36.92%)	167.25 (1.81%)
Pt/ dmlb	161.70 (47.33%)	162.90 (37.71%)	166.03 (4.99%)

Then, followed the same procedure, X-ray photoelectron spectra were taken of a PtNP film formed on an FTO/glass substrate, as is or with adsorbed 4-MBA. The Pt 4f spectra of the unmodified Pt sample (Figure 4-7a) shows the typical doublet for the 7/2 and 5/2 spin states, with binding energies of 69.50 eV and 72.83 eV, respectively. These peaks are assigned to the pure Pt nanoparticle in the zero-valent state.[103] In contrast, the spectrum of 4-MBA-modified Pt is deconvoluted into two doublets, one at 70.05 eV and 73.38 eV and one at 71.23 eV and 74.56 eV. These correspond to unbound Pt (0) and S-bonded Pt respectively. The binding energies of Pt in 4-MBA-modified Pt is higher than the binding energy of Pt (0) in pure Pt nanoparticles, but is much lower than the binding energy of partially oxidized Pt species.[104] However, the observed binding energies are consistent with literature reports for Pt in contact with S atoms.[90, 105, 106] The intensity of the Pt 4f signal of 4-MBA-modified Pt is roughly half that of the signal on unmodified Pt (under the same instrumental conditions), which is likely due to adsorbed 4-MBA attenuating detection of the Pt 4f electrons.[90]

Regarding the sulfur atoms, the S 2p XPS spectra of 4-MBA powder and 4-MBA-modified Pt are shown in Figure 4-7 c and 4-7 d. An intense doublet of 4-MBA powder at 163.20 eV and 164.40 eV is assigned to the binding energies of S $2p_{3/2}$ and S $2p_{1/2}$, respectively.[72, 79, 80, 107] A weak but broad peak at 168.96 eV is also observed, which indicates some sulfur oxidation. The doublet at 161.84 eV and 163.04 eV is shown in the S 2p region of 4-MBA-modified Pt, revealing the formation of Pt–S bond. This negative shift in binding energy of S 2p in contact with Pt or other metals was also reported in literature.[72, 79, 80, 107] Taken together, the XPS spectra shown in Figure 4-7 clearly indicate bonding between the Pt nanoparticles and the S atom in 4-MBA.

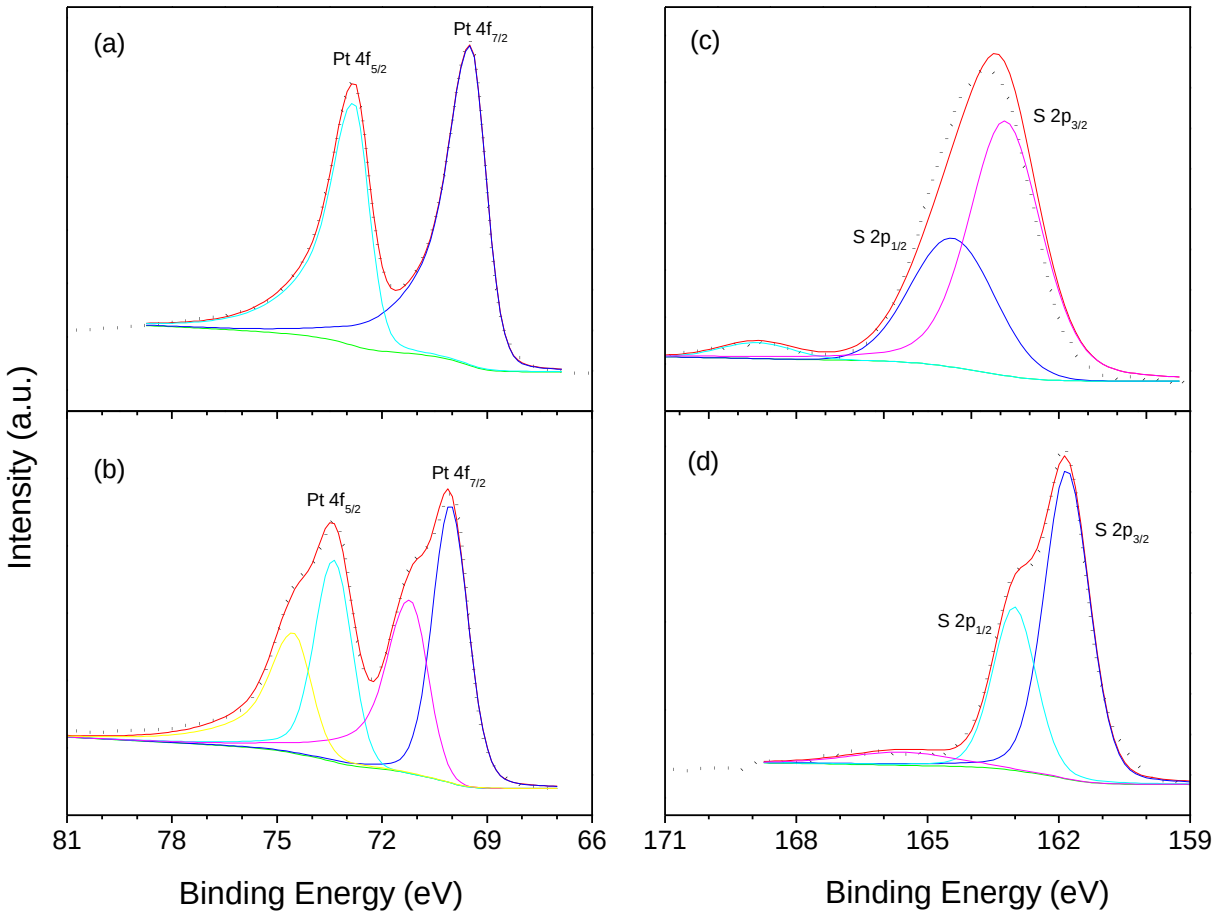

Figure 4-7. XPS Pt 4f spectra (a) pure Pt, (b) 4-MBA modified Pt; XPS S 2p spectra of (c) 4-MBA powder, (d) 4-MBA modified Pt

4.4 Conclusion

The formation of organometallic assemblies between Pt metal and the S atoms of 4-mercaptobenzoic acid (4-MBA) is confirmed by three different techniques: cyclic voltammetry (CV), Raman spectroscopy and X-ray photoelectron spectroscopy (XPS). From cyclic voltammetry, the largely decreased intensity of the reduction and oxidation peaks of the potassium ferrocyanide/ferricyanide redox couple between the 4-MBA-modified and bare Pt electrode shows the electrochemical blocking effect caused by the binding of 4-MBA to the Pt surface, which is not observed with benzoic acid. From Raman spectra, the complete absence of the S–H stretching vibrational mode on 4-MBA-modified Pt nanoparticle is consistent with the molecules' being sulfur-bonded to the nanoparticle surface. The emergence of new S and Pt peaks in XPS spectra when 4-MBA and Pt are brought into contact suggests the formation of Pt–S bonds. Therefore, 4-MBA binds to Pt via the thiol group while the carboxyl group is left free (Figure 4-8). However, neither the 4,4'-dimethyl-lipoate-2,2'-bipyridine nor the disulfide moiety of lipoic acid could bind to Pt as strongly as the thiol group of 4-MBA.

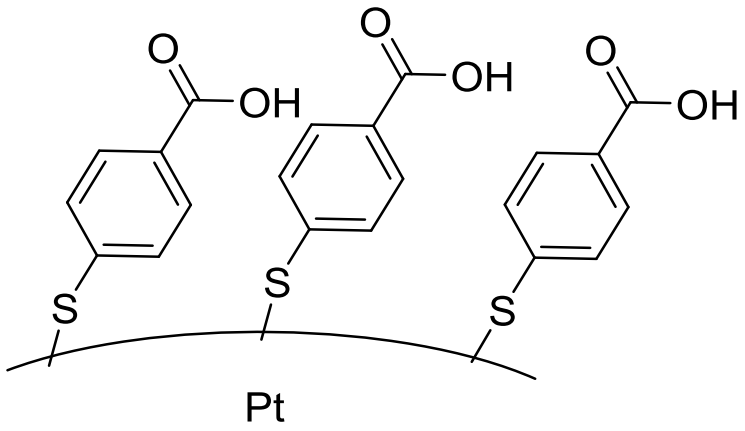

Figure 4-8. Pt binding to 4-mercaptobenzoic acid through a Pt–S bond

CHAPTER 5. DYE-ANCHORED PLATINUM NANOCATALYSTS FOR DYE-SENSITIZED SOLAR CELLS

5.1 Introduction

5.1.1 Synthesis of Platinum Nanoparticles

Platinum nanoparticles can be synthesized with particle sizes between 2 nanometers (nm) and 100 nm, depending on the reaction conditions. The smaller particle size correlates to a higher surface area per mass of the metal. They commonly exhibit in the form of a suspension or colloid, which generally defined as a stable dispersion of nanoparticles in a fluid medium. Due to their outstanding chemical and physical properties, tunable particle sizes, the potential applications of Pt nanoparticles have been developed in a wide variety of areas, such as fuel cells, electronics, catalytic, photovoltaic and biological applications.[108, 109, 110, 111, 112, 113]

Various methods have been developed to investigate platinum nanoparticles with different sizes and shapes according to specific usage.[114, 115, 116] Our previous colleague, Guangliang Liu, compared three methods of synthesizing Pt nanoparticles in terms of getting particle sizes with diameters in the range of 1-3 nm for a good catalytic performance and maintaining the colloid stability at the same time.[117] Method 1 is a modified procedure by Wang et al.,[93] which reduces the Pt precursor, hexachloroplatinic acid hexahydrate ($H_2PtCl_6 \cdot 6H_2O$) or platinum(IV) chloride ($PtCl_4$), in ethylene glycol with sodium hydroxide (NaOH). Methods 2 and 3 are based on phase-transfer synthesis of Pt(IV) from water to toluene by reduction with a reducing agent ($NaBH_4$). The two methods differ in the sequence of adding a stabilizer (an alkylamine or alkanethiol) and the reducing agent.

After a thorough comparison of those three methods,[117] it was found that the Pt nanoparticles made by Method 1 (Figure 5-1) have the smallest particle size (1.6 nm) compared to the other two methods, and are highly stabilized in a suspension of ethylene glycol which can be stored for a long time without aggregation or precipitation. In addition, it is also the simplest method among those three. Therefore, Method 1 would be used in the further study.

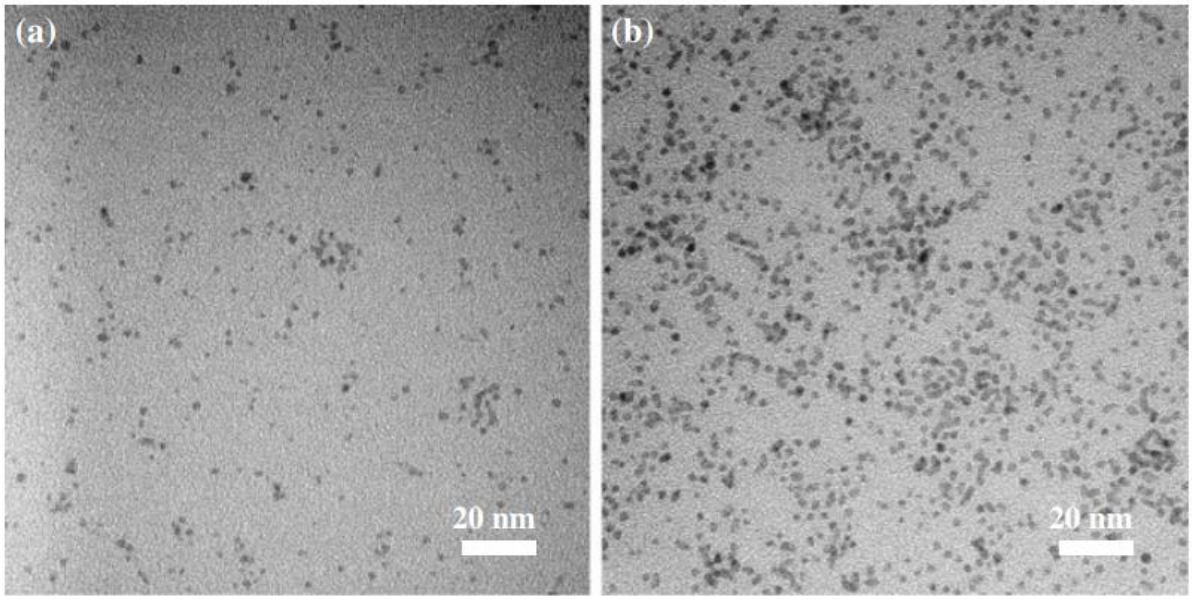

Figure 5-1. TEM images of Pt NPs dispersed in ethylene glycol prepared by Method 1 using a) $H_2PtCl_6 \cdot 6H_2O$, b) $PtCl_4$ [117]

5.1.2 Impact of Voltage Loss and Pt Nanocatalyst

Electrochemical potential of the reduced and oxidized dye plays an important rule of converting photons to electrons in a DSC since the energy level of the dye should match between the TiO_2 and the electrolyte. On one hand, the excited state level of the dye should be higher in energy than the conduction band of TiO_2, allowing electron injection. On the other hand, the oxidized state

level of the dye should be more positive than potential of the iodide/triiodide redox couple in the electrolyte, allowing dye regeneration.[13]

Pt nanoparticles have been commonly used as a catalyst for the reduction of triiodide to iodide reaction on the counter electrode in a DSC device, due to the high electrocatalytic activity of Pt and its stability against corrosion by iodide/triiodide.[118] By introducing Pt nanoparticles in the iodide/triiodide electrolyte, it is hoped that the intermediate species $I_2^{\cdot-}$ can be avoided, which allows the iodide oxidation to triiodide to occur as $3I^- \rightarrow I_3^- + 2e^-$, avoiding a large loss in potential energy. The overall device efficiency could exceed 15% if this overpotential loss could be halved.[16]

Previously in Chapter 4, we have demonstrated the successful formation of organometallic assemblies between Pt metal and the S atoms of 4-MBA. However, in this study, we first of all, anchored the model molecule, 4-MBA, to a TiO_2 surface, bound Pt nanoparticles to them, formed a demo system, TiO_2–4MBA–Pt, and also measured the catalytic capability of Pt in this assembly. Then we made the assembly with our bifunctional dye to replace the 4MBA, formed TiO_2–dye–Pt and built DSC devices.

5.2 Experimental

5.2.1 Preparation of Pt Nanoparticles

Platinum nanoparticles were synthesized according to the method developed by Wang et al.[93] A 50 mL 0.5 M ethylene glycol solution of NaOH was added dropwise to a 50 mL ethylene glycol solution containing 1.93 mmol $H_2PtCl_6 \cdot 6H_2O$, with constant stirring at 400 rpm. The mixture was

heated at 160 ℃ for 3 hours, with nitrogen bubbling through the system to remove water, oxygen and other reaction byproducts.

The mechanism was suggested as follows:[119]

$$CH_2OHCH_2OH \rightarrow CH_3CHO + H_2O \quad (5)$$

$$2CH_3CHO + (PtCl_6)^{2-} + 6OH^- \rightarrow 2CH_3COO^- + Pt + 6Cl^- + 4H_2O \quad (6)$$

where reaction (5) is thermal decomposition of the solvent to acetaldehyde, and reaction (6) is reduction of the Pt precursor by acetaldehyde to give acetate. In addition, the function of the sodium hydroxide is to keep the acetate deprotonated for capping the Pt nanoparticles.

The resulting acetate in reaction (6) was used to stabilize the produced Pt nanoparticles. Their particle size was measured by dynamic light scattering (DLS), shown in Figure 5-2. The Pt nanoparticles exhibited a uniform size distribution by number with a mean radius of less than 1 nm.

After the reaction, a transparent dark-brown homogeneous Pt nanoparticle colloidal suspension was obtained, without any precipitate. The pH of the Pt suspension was adjusted to 3 by adding 0.5 M HCl, inducing aggregation. The suspension was washed by centrifugation at 4000 rpm for 20 min, discarding the supernatant, and resuspended in ethylene glycol.

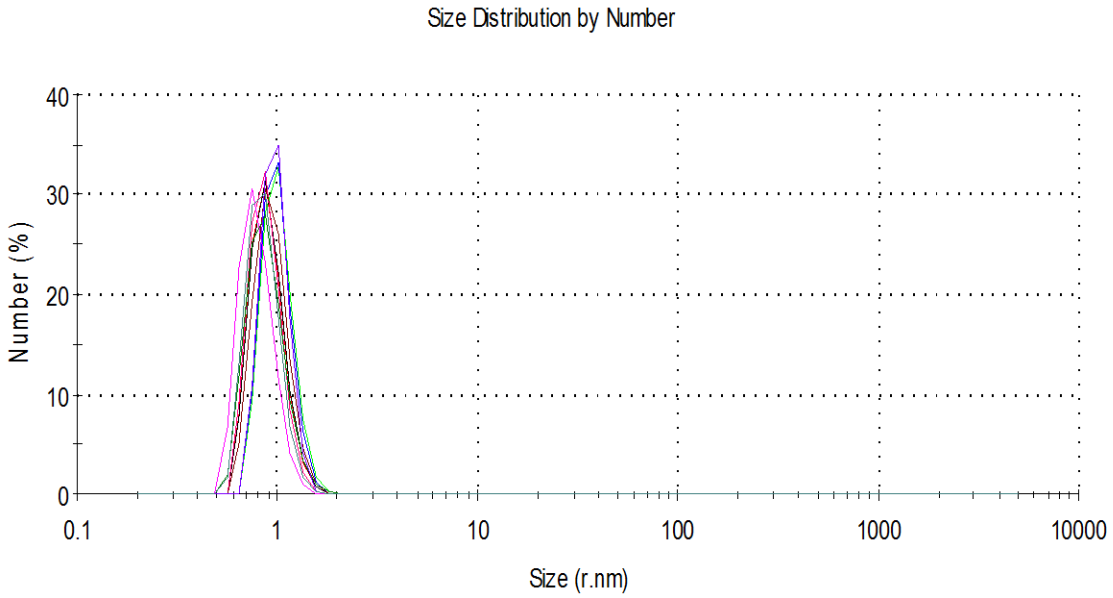

Figure 5-2. DLS plot of the Pt nanoparticle size distribution by number

5.2.2 Characterization of Catalysis

Cyclic Voltammetry. 0.5 mM 4-MBA were added to a 0.5 mM of Pt NPs redispersed ethanolic solution described above, and stirred overnight. A compact TiO_2 film, which was deposited on a FTO substrate by spray pyrolysis, using a 20 mM titanium diisopropoxide bis(acetylacetonate) in 2-propanol solution at 450 °C for 30 min was immersed in the 4-MBA-Pt ethanolic solution overnight. For comparison, another spray pyrolysed TiO_2 film was immersed in a bare Pt ethanolic solution.

The electrochemistry was investigated in acetonitrile containing 0.5 M $TBAPF_6$ with and without iodide/triiodide electrolyte (100:1 v/v) as supporting electrolyte, and scanned at a rate of 100 mV/s. Pt wire was used as the counter electrode. The Pt-exposed TiO_2 films were used as working electrodes. The reference electrode was Ag/Ag^+.

EDX. The Pt/Ti atomic ratio of the Pt-exposed TiO_2 films was analyzed by Energy-dispersive X-ray spectroscopy (EDX), which was conducted on an FEI Quanta FEG250 SEM in high vacuum mode operated at the accelerating voltage of 120 kV with a Cu Kα X-ray source. Five different EDX spots were analyzed for each of two samples.

5.2.3 Synthesis and Characterization of Dye Molecules

The bifunctional dye Ru(dcb)(4MA)$(NCS)_2$, where dcb = 4,4′-dicarboxylic acid-2,2′-bipyridine and 4MA = 4,4'-di-4-mercaptobenzoicanalide-bipyridine (Figure 5-3 a), was synthesized by our collaborators, Ian Weiss and Prof. Elena Galoppini at Rutgers University-Newark. Two reference dyes were used, which have carboxyl groups but no thiols. One is Ru(dcb)(dnb)$(NCS)_2$, also known as Z907,[120] where dnb = 4,4′-dinonyl-2,2′-bipyridine (Figure 5-3 b). The other is Ru(dcb)(4A)$(NCS)_2$, where 4A = 4,4'-dibenzoicanalide-bipyridine (Figure 5-3 c), which is identical to the bifunctional dye except that it lacks the thiol groups.

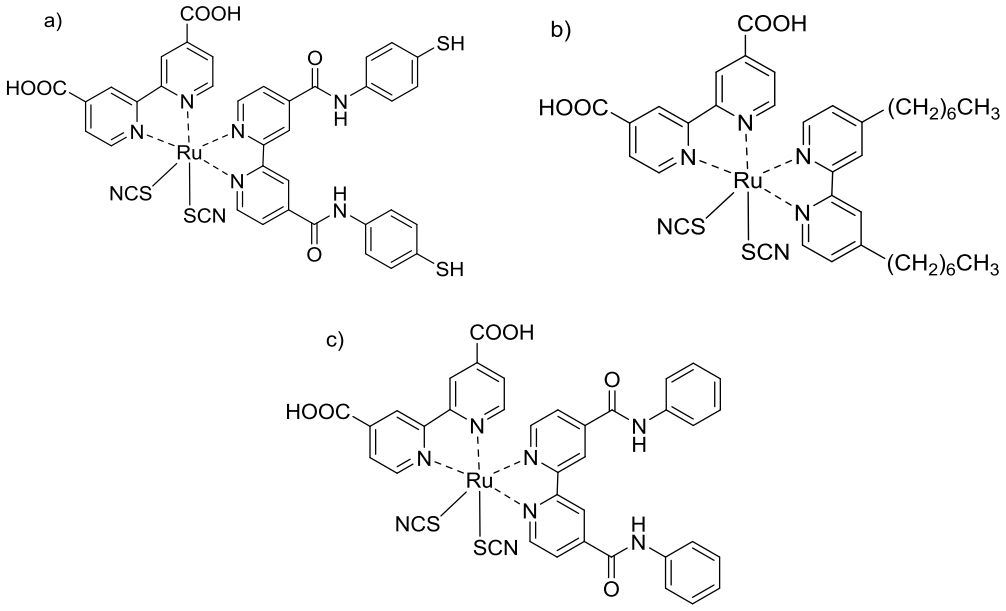

Figure 5-3. Molecular structures of dyes a) Ru(dcb)(4MA)$(NCS)_2$, b) Ru(dcb)(dnb)$(NCS)_2$, c) Ru(dcb)(4A)$(NCS)_2$

Both reaction schemes are shown in Scheme 5-1.

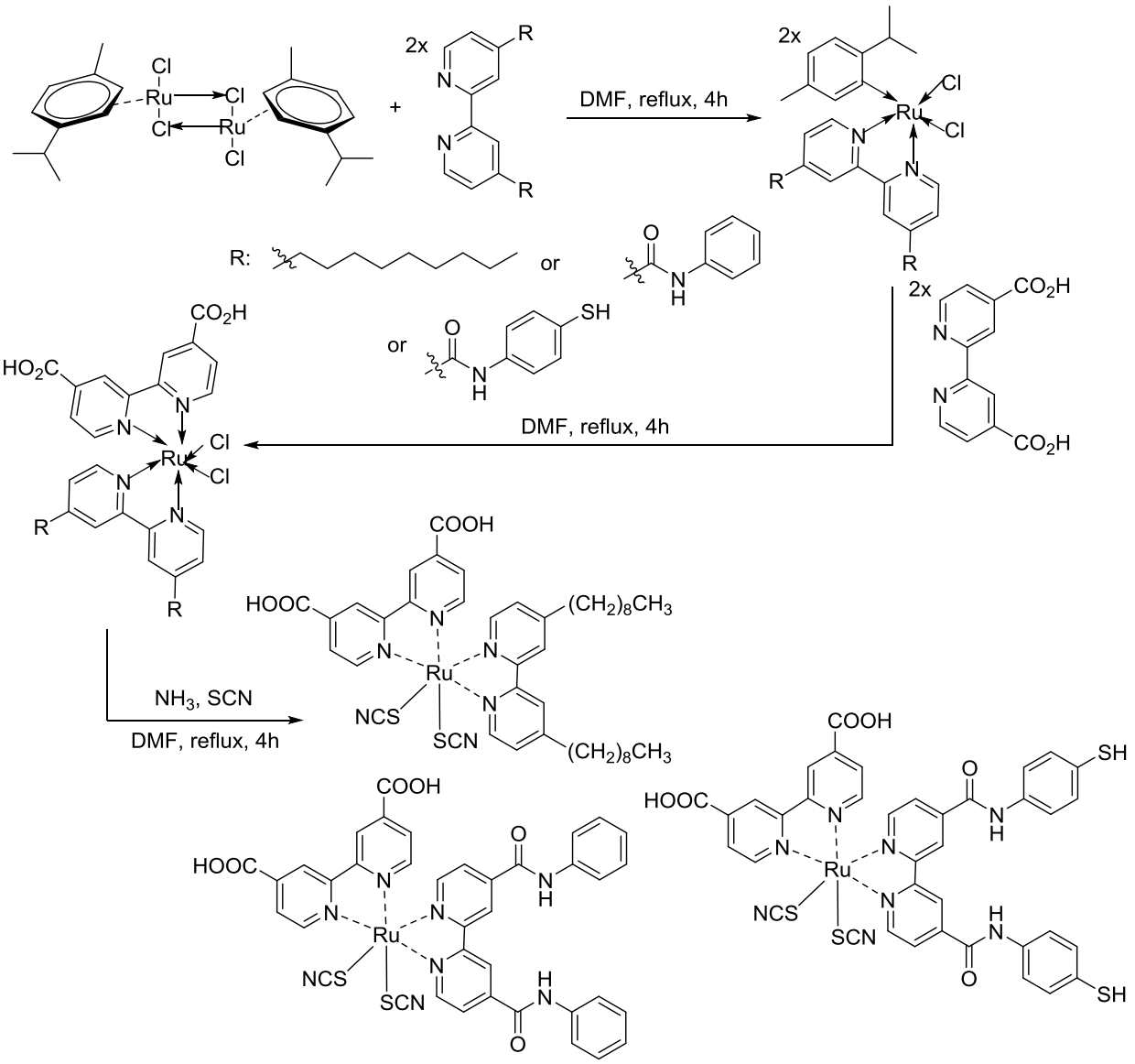

Scheme 5-1. Synthetic scheme for Ru(dcb)(dnb)$(NCS)_2$, Ru(dcb)(4A)$(NCS)_2$ and Ru(dcb)(4MA)$(NCS)_2$

5.2.4 Dye-Sensitized Solar Cell Fabrication and Characterization

Devices made at École polytechnique fédérale de Lausanne (EPFL)

NCS-10 glass (10 Ω/sq) was used as the substrate for the working electrode, which was cleaned in detergent for 45 min in ultrasonic bath, followed by rinsing with DI water and ethanol, a 15 min ozone treatment, and $TiCl_4$ pre-treatment (150 mL of DI water with 3 mL of 2 M $TiCl_4$ stock solution for 30 min at 70℃) twice.

The cleaned substrated was coated with an 8 μm thick TiO_2 film with a particle size of 18 nm and a 4 μm thick scattering layer composed of 400 nm sized TiO_2 particles to form the working electrode. The film was made by screen printing the TiO_2 paste, followed by sintering at 500 ℃ for 30 min, then post-treatment by $TiCl_4$ solution. The thickness of the film was measured by the profilometer. The counter electrode and electrolyte fabrication methods are the same as the recipe listed in Chapter 3.

The dye solutions were 0.2 mM in *tert*-butanol/acetonitrile (1:1). The TiO_2 films were dipped in the dye solution for 18 hours to complete the loading with sensitizers, followed by another 18 hours in 0.1 mM of Pt suspension in ethylene glycol if necessary. Samples not exposed to Pt were still immersed in ethylene glycol to control for any effects from that solvent.

Devices made at UConn

The devices made at UConn were followed the steps mentioned in Chapter 3.

5.3 Results and Discussion

Catalysis. As shown in Figure 5-4, the cyclic voltammogram of 4MBA-Pt and Pt-modified TiO_2 electrodes in supporting electrolyte with iodide/triiodide redox couple from -0.2 V to -1.5V (vs. Ag/Ag^+) exhibits multiple reduction peaks. The first peak at around -0.9 V does not appear in a solution without the iodide/triiodide electrolyte (Figure 5-5) and is assigned to reduction of triiodide to iodide. The subsequent reduction peaks are attributed to a combination of reductions with both the redox electrolyte and the solvent, as some reduction current is seen also in Figure 5-5. Only small oxidation currents are observed under any conditions because the TiO_2 film is insulating at potentials that are well positive of its conduction band. The analysis was repeated with a second set of samples and gave the same results.

Focusing on the features near -0.9 V, which are due to reduction of triiodide to iodide, there is negligible faradaic current on a bare TiO_2 surface. This reaction is known to be slow on TiO_2, which is why iodide/triiodide is a good redox couple for dye-sensitized solar cells. PtNPs at the TiO_2/solution interface catalyze this reaction, as seen in Figure 5-4. Notably, compared to TiO_2 exposed to bare PtNPs, loading TiO_2 with 4-MBA-bound PtNPs results in a higher peak current and earlier onset of this reduction peak, indicating enhanced catalytic activity.

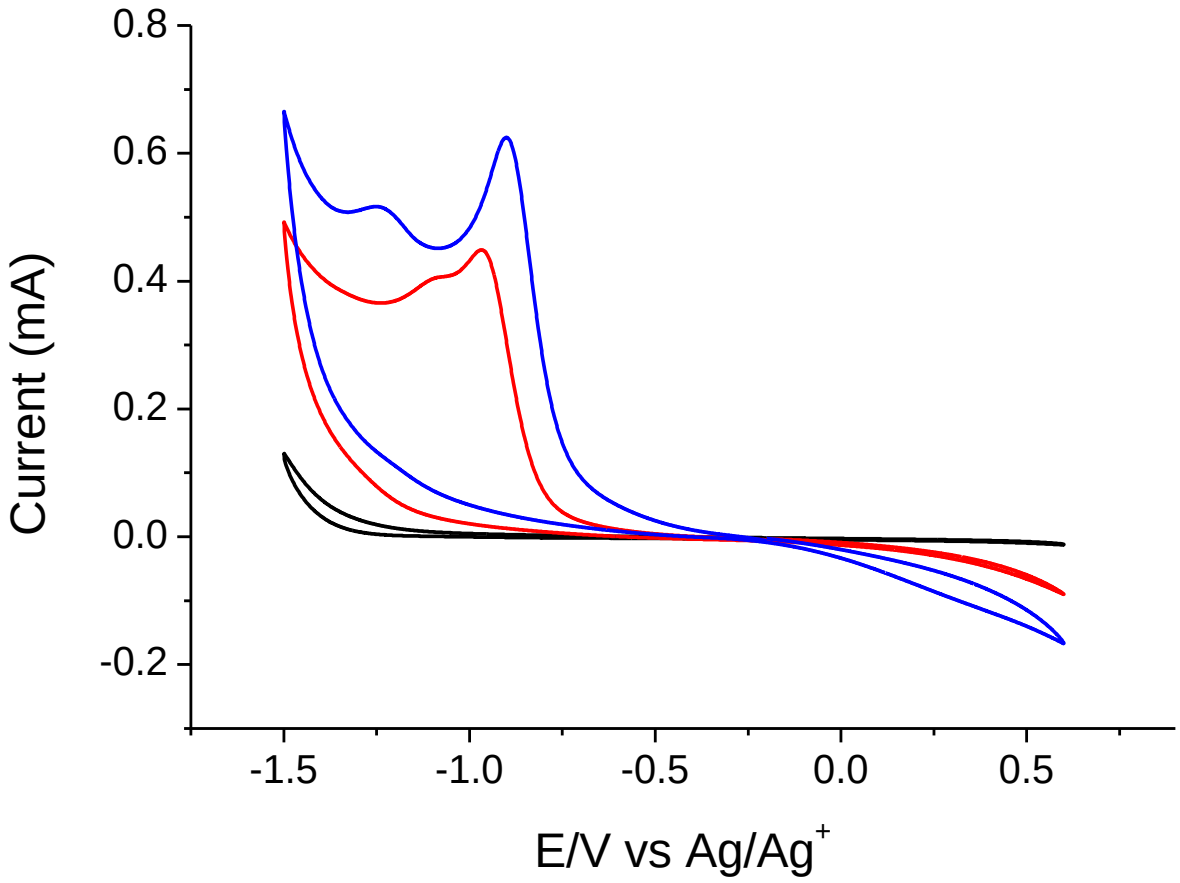

Figure 5-4. Cyclic voltammetry of (black) spray pyrolysed TiO_2 film; (red) Pt modified TiO_2 film; (blue) 4MBA-Pt modified TiO_2 film as working electrodes in supporting electrolyte of 0.5 M $TBAPF_6$ in acetonitrile with iodide/triiodide electrolyte, scanned at 0.1 V/s

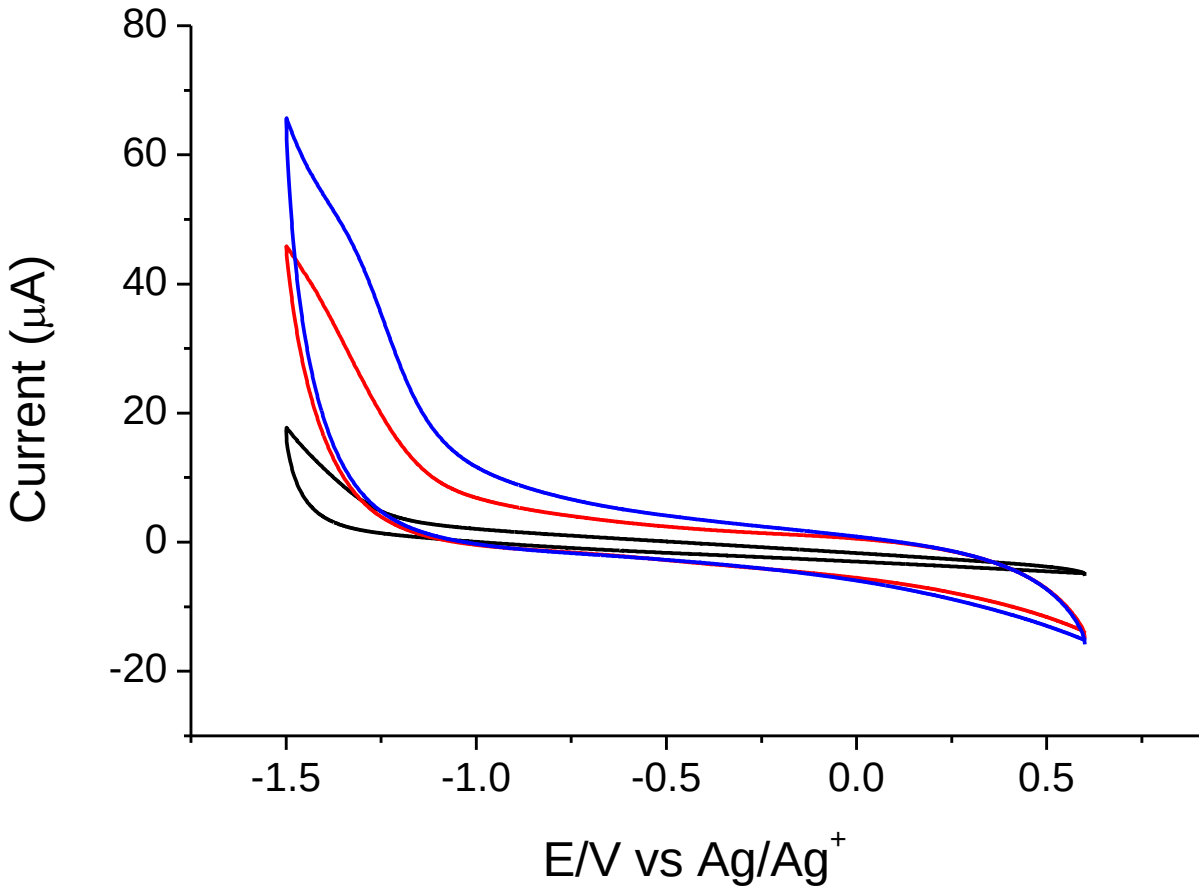

Figure 5-5. Cyclic voltammetry of (black) spray pyrolysed TiO_2 film; (red) Pt modified TiO_2 film; (blue) 4MBA-Pt modified TiO_2 film as working electrodes in supporting electrolyte of 0.5 M $TBAPF_6$ in acetonitrile without iodide/triiodide electrolyte, scanned at 0.1 V/s

To assess whether the difference in catalytic activity was due to the amount of Pt and the TiO_2 surface or to other factors, EDX was used to measure the Pt:Ti atom ratio. The value was 0.59 $\pm$ 0.03 for 4-MBA-Pt on TiO_2 and 0.54 $\pm$ 0.03 for bare Pt on TiO_2. The difference between the means is statistically significant at the 95% confidence level. This slight increase (9%) in Pt loading enabled by 4-MBA binding is unlikely to explain the resulting 38% increase in peak current for triiodide reduction. We speculate that the remaining effect of 4-MBA may be due either to better

electronic coupling of TiO_2 to Pt or to a more favorable binding morphology, i.e., perhaps bare PtNPs tend to cluster on the surface whereas 4-MBA-PtNPs are more likely to bind as individual particles, having higher surface area and hence catalytic activity. These will be the subjects of further investigations. For now, this result demonstrates that 4-MBA can be used to bind to TiO_2 and increase the former's catalytic activity.

Current–Voltage *(J-V)* Characteristics

Devices made at EPFL

The device performance of the reference dye $Ru(dcb)(dnb)(NCS)_2$ and the bifunctional dye $Ru(dcb)(4MA)(NCS)_2$ in the condition with and without Pt nanoparticles were summarized in Table 5-1. These devices were fabricated in the Laboratory of Photomolecular Science (LSPM) in EPFL during my visit in January 2018.

For the reference dye $Ru(dcb)(dnb)(NCS)_2$, shown in Figure 5-6, a dramatic efficiency decrease was observed in the device with Pt nanoparticles compared to the ones without, due to the decrease in both J_{sc} and V_{oc}, likely due to Pt NPs physisorbed directly to the TiO_2 surface causing fast recombination between electrons in the TiO_2 and triiodide.

Table 5-1. Current density (J_{sc}), open-circuit voltage (V_{oc}), fill factor (FF) and efficiency of solar cell devices under different conditions

	J_{sc} (mA/cm^2)	V_{oc} (V)	FF	Efficiency (%)
Ru(dcb)(dnb)$(NCS)_2$	7.25	0.56	0.75	3.08
Ru(dcb)(dnb)$(NCS)_2$ + Pt	4.30	0.48	0.72	1.50
Ru(dcb)(4MA)$(NCS)_2$	5.32	0.54	0.77	2.28
Ru(dcb)(4MA)$(NCS)_2$ + Pt	6.59	0.56	0.75	2.77

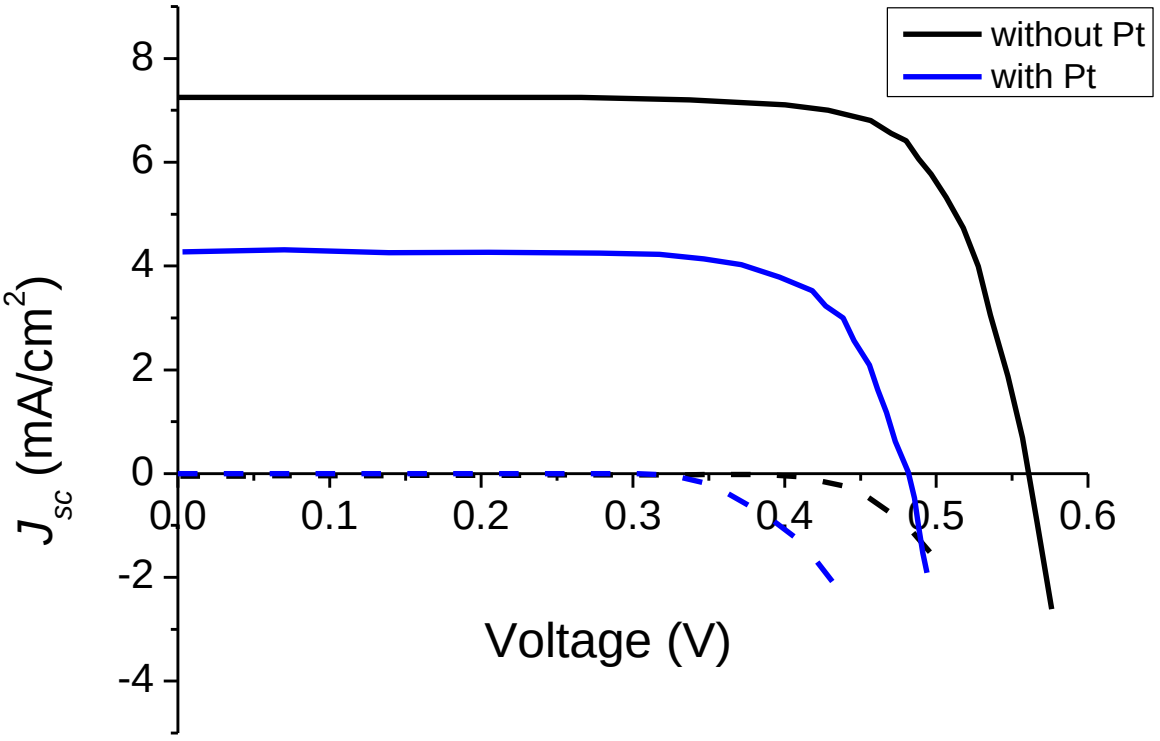

Figure 5-6. Current-voltage characteristics of solar cells under one sun of Ru(dcb)(dnb)$(NCS)_2$ (black) and Ru(dcb)(dnb)$(NCS)_2$-Pt (blue), under sunlight (solid) and in darkness (dashed)

Regarding the bifunctional dye Ru(dcb)(4MA)$(NCS)_2$, the efficiency of the DSC devices with Pt nanoparticles were enhanced by 21% due to the increased J_{sc}, in comparison of the ones without. No changes were observed in terms of V_{oc} in both conditions, or in the *J-V* curve in the dark (Figure 5-7), indicating no increase in recombination between TiO_2 and the electrolyte. This suggests that the Pt nanoparticles were not bound to the TiO_2 surface, but only to the thiol group on the bifunctional dye. As a result, the Pt nanoparticles could help to improve the solar power efficiency in the DSC device with the bifunctional dye. This may be due to Pt catalysis accelerating the regeneration (reduction) of oxidized dye molecules by iodide.

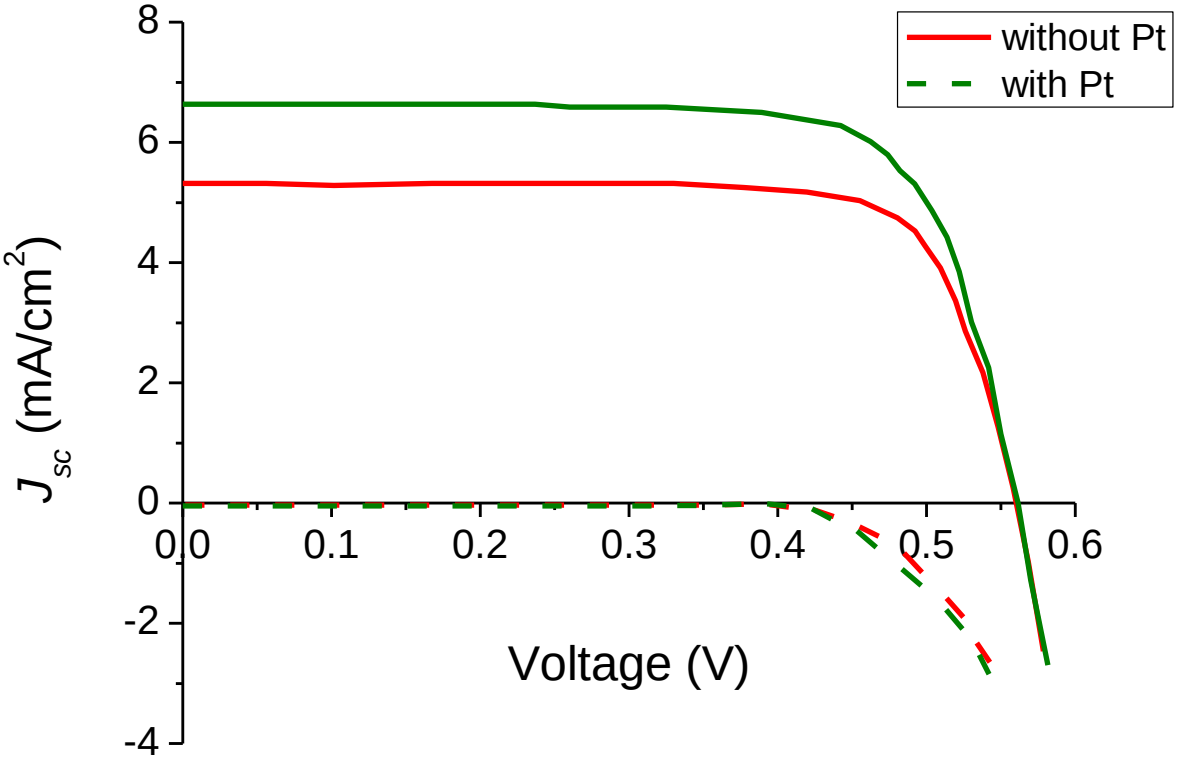

Figure 5-7. Current-voltage characteristics of solar cells under one sun of Ru(dcb)(4MA)$(NCS)_2$ (red) and Ru(dcb)(4MA)$(NCS)_2$-Pt (green), under sunlight (solid) and in darkness (dashed)

Device made in UConn

Solar cell devices were fabricated in our lab at UConn, by using a different reference dye with phenyl-terminated ligands lacking the thiol group, $Ru(dcb)(4A)(NCS)_2$ (structure shown in Figure 5-3c) and a new batch of more purified bifunctional dye, $Ru(dcb)(4MA)(NCS)_2$.

The device performance of these dye molecules with and without Pt nanoparticles were summarized in Table 5-2 and the current-voltage curves were shown in Figure 5-8 and Figure 5-9, respectively. Based on the results, a significant efficiency decrease in both the reference dye, $Ru(dcb)(4A)(NCS)_2$, and the bifunctional dye, $Ru(dcb)(4MA)(NCS)_2$, were observed in the system with Pt nanoparticles compared to the ones without. Especially, the Pt nanoparticles brought a rapid decrease in voltage with both dye molecules, indicating a fast recombination between the TiO_2 surface and Pt nanoparticles, regardless of the existence of a thiol group on a dye molecule. After involving Pt nanoparticles, the device performances of both reference dye and the bifunctional dye had similar results in all parameters (J_{sc}, $V_{ov,}$ FF and efficiency).

Table 5-2. Current density (J_{sc}), open-circuit voltage (V_{oc}), fill factor (FF) and efficiency of solar cell devices under different conditions

	J_{sc} (mA/cm^2)	V_{oc} (V)	FF	Efficiency (%)
$Ru(dcb)(4A)(NCS)_2$	3.36	0.65	0.67	1.44
$Ru(dcb)(4A)(NCS)_2$ + Pt	4.21	0.31	0.39	0.50
$Ru(dcb)(4MA)(NCS)_2$	6.14	0.64	0.65	2.58
$Ru(dcb)(4MA)(NCS)_2$ + Pt	4.21	0.30	0.35	0.44

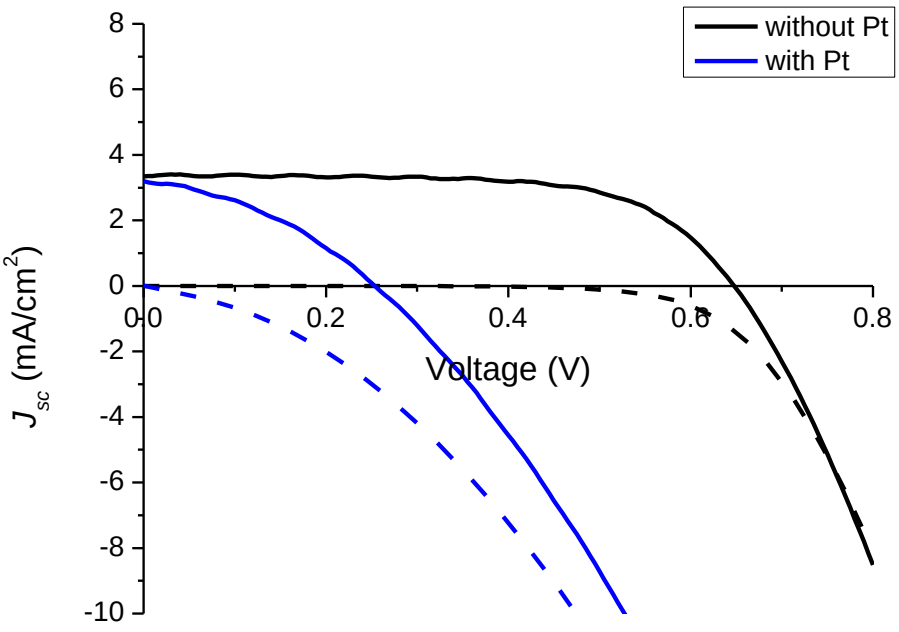

Figure 5-8. Current-voltage characteristics of solar cells under one sun of Ru(dcb)(4A)$(NCS)_2$ in black and Ru(dcb)(4A)$(NCS)_2$-Pt in blue, under sunlight (solid) and in darkness (dashed)

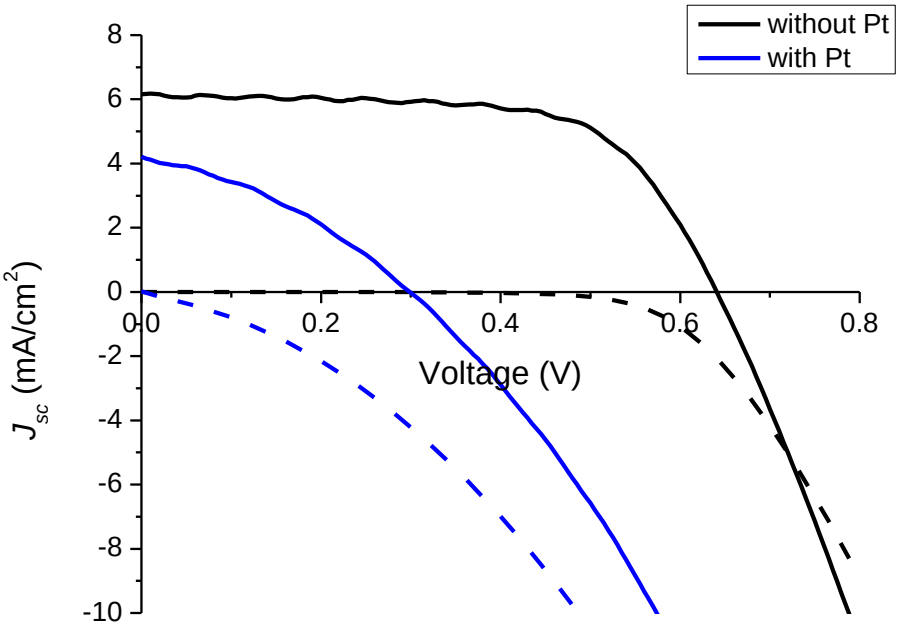

Figure 5-9. Current-voltage characteristics of solar cells under one sun of Ru(dcb)(4MA)$(NCS)_2$ in black and Ru(dcb)(4MA)$(NCS)_2$-Pt in blue, under sunlight (solid) and in darkness (dashed)

Comparison

Compared to the devices made in EPFL with those made in UConn, the efficiencies of both reference dyes have shown significant decrease with Pt nanoparticles involved, in both current and voltage, in comparison with the system without Pt nanoparticles. However, from the perspective of the bifunctional dye, Ru(dcb)(4MA)$(NCS)_2$, instead of seeing an improvement in efficiency with the assembly of bifunctional dye-Pt, an opposite result has seen from the devices made in UConn. There are several possible reasons for this discrepancy.

First of all, the solvents of the dye bath are different in the two labs. The solvent used in EPFL was *tert*-butanol/acetonitrile (1:1), whereas the solvent used in UConn was ethanol. The former solvent appeared more able to dissolve the dye. If the dye solvent results in better dye dissolution and/or better dye loading of the TiO_2 surface, it would leave less bare TiO_2 exposed for Pt NPs to physisorb to directly.

Secondly, the two experiments used two different batches of the bifunctional dye, which had been through different degrees of purification, with the batch used at UConn believed to be more pure than the one used at EPFL.

In addition, there are some other differences between different labs, which can also make the results different. For example, the TiO_2 films are made and treated differently. Screen-printed TiO_2 films with before-and-after $TiCl_4$ treatments were made in EPFL, and doctor bladed TiO_2 films without $TiCl_4$ treatment were made in UConn. The electrolytes are slightly different, homemade at EPFL and commercialized from Dyesol at UConn.

Therefore, more experiments need to be done in order to figure out the influence of the Pt nanoparticles in a DSC system with a bifunctional dye.

5.4 Conclusions

The formation of a model system, TiO_2–4MBA–Pt, is confirmed in Chapter 4 by three different techniques: cyclic voltammetry (CV), Raman spectroscopy and X-ray photoelectron spectroscopy (XPS). This chapter further demonstrated the catalytic performance of this demo assembly. The results suggest that the thiol group of 4-MBA binds to Pt, act as a catalyst, either as films or nanoparticles, while the carboxyl group remains available for attachment to other surfaces such as TiO_2, shown in Figure 5-10.

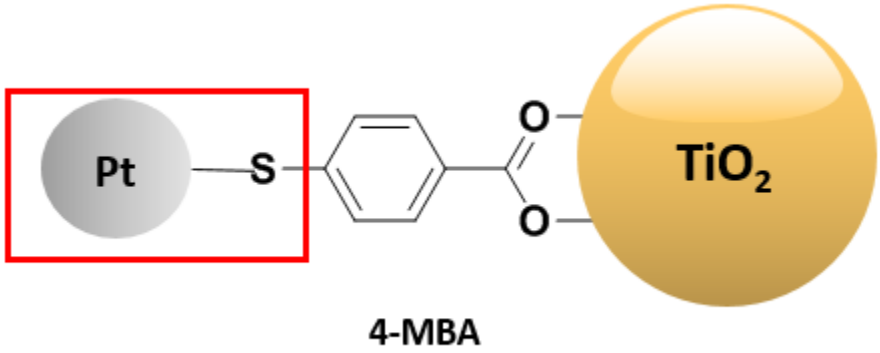

Figure 5-10. 4-MBA bonds through a thiol linkage to a Pt

In addition, a bifunctional N3-type complex, Ru(dcb)(4MA)$(NCS)_2$, with one bipyridyl ligand modified with 4-mecaptobenzoic acid units to bind to the Pt nanoparticles, and another bipyridyl ligand modified with –COOH groups to attach to the TiO_2 surface, was synthesized. The results obtained from the lab in EPFL were that the performance of the bifunctional dye, Ru(dcb)(4MA)$(NCS)_2$, was improved by binding through a Pt–S bond, whereas the reference dye, Ru(dcb)(dnb)$(NCS)_2$, had its performance significantly decreased by Pt loading. However, the results from UConn gave the same degradation of performance of the bifunctional dye upon Pt

loading as the reference dye. Future work will be needed to determine what conditions allow the improvement of bifunctional dye performance by Pt without the recombination losses due to Pt NPs in direct contact with TiO_2.

CHAPTER 6. ELECTRONIC EFFECTS OF MODIFYING *MESO*-TETRAKIS(PENTAFLUOROPHENYL)PORPHYRIN DERIVATIVES

6.1 Introduction

Key to the increase of efficiency in porphyrin-based DSCs was the development of non-aggregating porphyrins with high extinction coefficient absorption spectra reaching into the NIR, such as porphyrin **1** and **2** shown in Figure 6-1**.**[30, 34] However, the syntheses of these and related systems is complex and inefficient, inhibiting the progress in the understanding of the correlation of molecular design and photovoltaic performance.[121] Recently tested hydroporphyrins were promising but they were also prepared by multi-step, non-trivial total syntheses.[122]

Dyes containing pentafluorophenyl (C_6F_5) groups are particularly appealing in this context.[123] The parent porphyrins, *meso*-tetrakis(pentafluorophenyl)porphyrin (T^FPP, **5**) is well known and commercially available.[124] Scheme 6-1 showed the synthetic scheme of our interested porphyrin derivative sensitizers by our collaborators, Nisansala Hewage and Prof. Christian Brückner. [125]

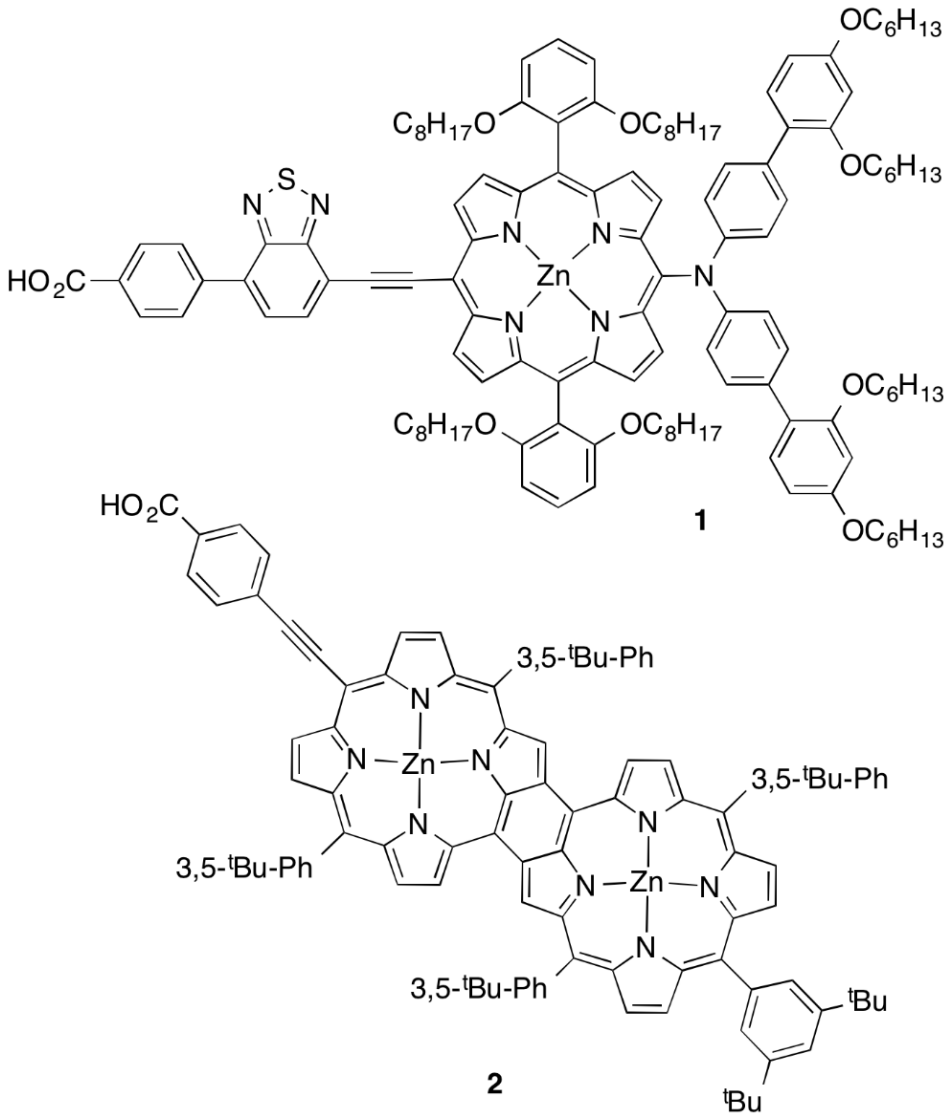

Figure 6-1. Molecular structures of push-pull architecture porphyrin **1** and π-extended porphyrin **2**

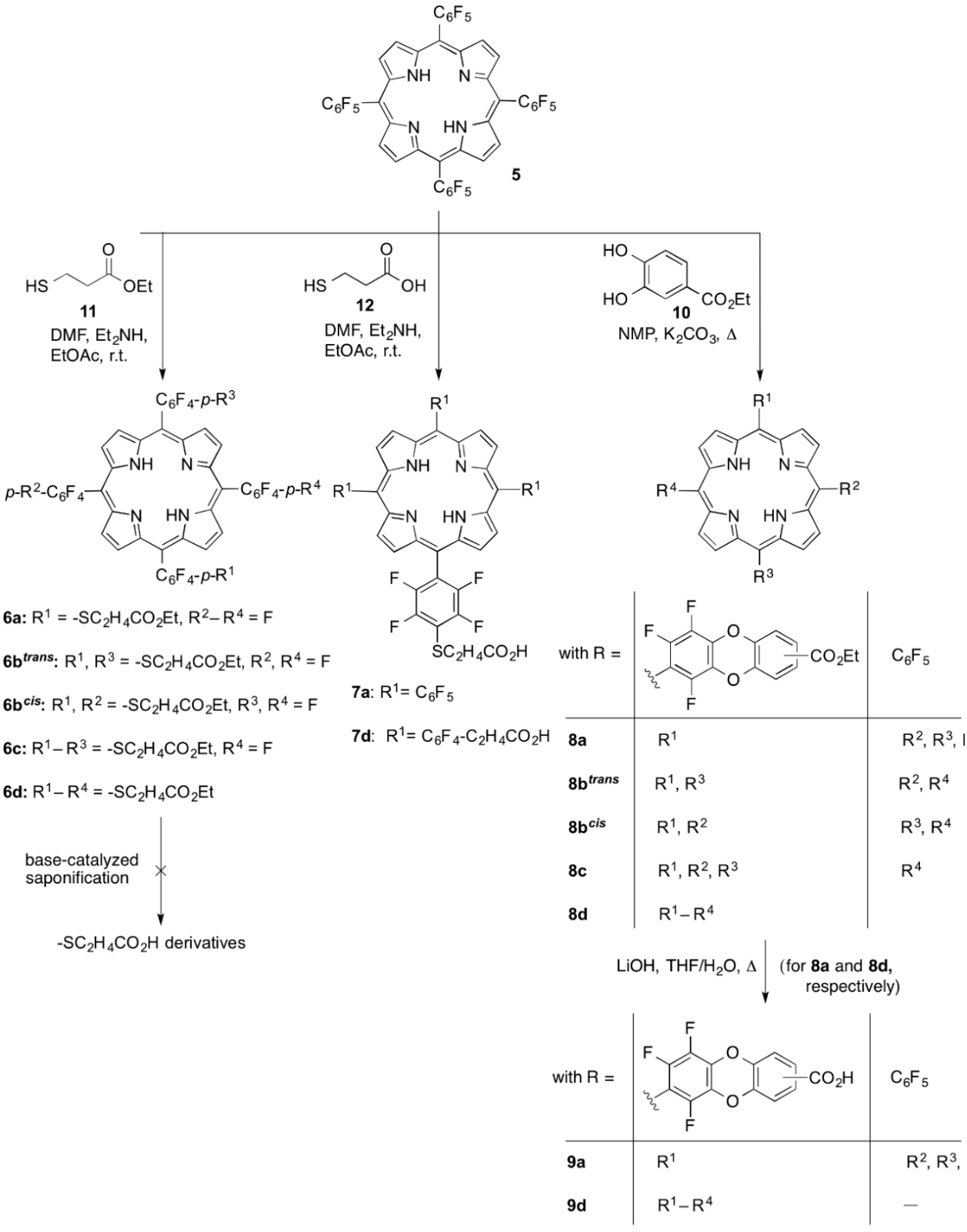

Scheme 6-1. Synthesis scheme of all derivatives prepared

Regardless of the type of dye, carboxylic acid groups are by far the most common anchoring group for dye attachment to TiO_2 or other metal oxide surfaces (Scheme 6-2).[48, 126, 127, 128] However, from a practical point of view, the synthesis of porphyrinoid dyes with a single or multiple carboxylic acid groups is associated with practical difficulties since conventional bulk silica gel column chromatography techniques are difficult to apply to (poly)carboxylates. This suggests the unveiling of the carboxyl functionality at a very late stage of the dye synthesis, such as by synthesis of protected carboxyl derivatives that are deprotected directly prior to attachment to the semiconductor.[129]

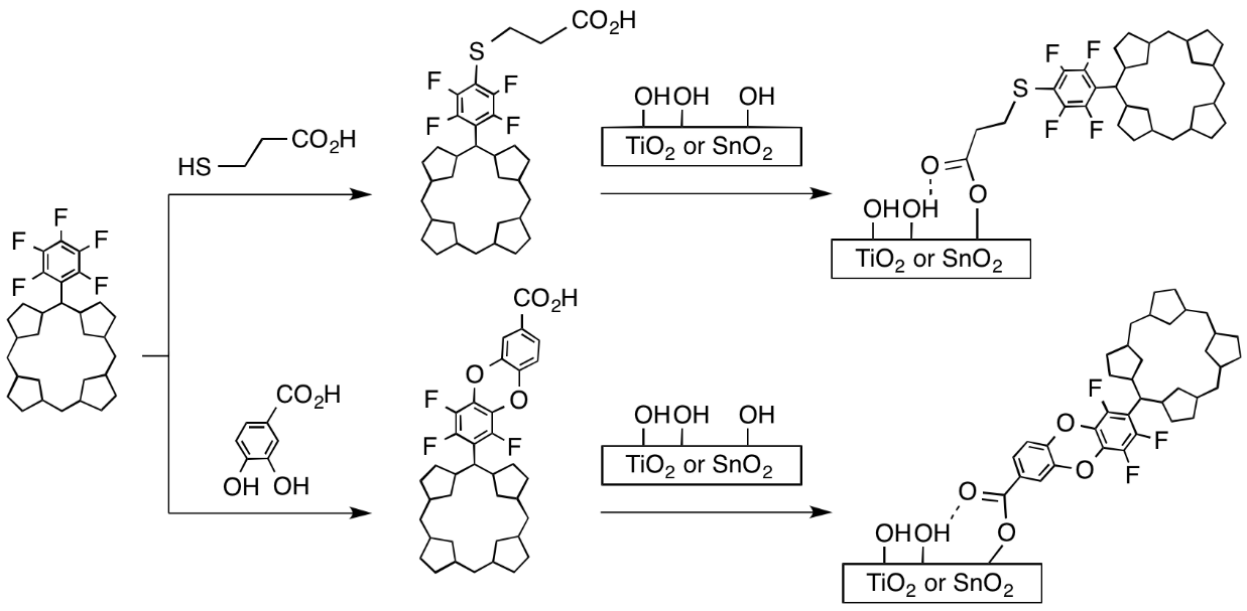

Scheme 6-2. Mercatopropionic acid and 3,4-dihydroxybenzoic acid derivatizations investigated

6.2 Sample Preparation and Characterization

Cyclic Voltammetry. Cyclic voltammetry experiments were recorded on a CHI600D electrochemistry system with a standard three-electrode cell assembly. The supporting electrolyte was 0.1 M $TBAPF_6$ dissolved in dry CH_2Cl_2. Pt wires were employed as both working and counter electrodes; an Ag/Ag^+ couple was used as the reference electrode. All concentrations of dye solutions were maintained at 1 mM, and scanned at a scan rate of 200 mV/s. Prior to scanning, the solutions were sparged 5-10 min with a stream of purified N_2.

UV-Vis Measurements. UV-vis spectra were recorded on a Cary 50 spectrophotometer and fluorescence emission spectra on a Cary Eclipse fluorimeter.

TiO_2 Films. TiO_2 thin films were fabricated on microscope slides by spin coating 100 μL of TiO_2 paste (DSL 90-T, diluted 1:1 with terpineol) at 1000 rpm for 30 s, followed by sintering at 500 ℃ for 30 min. The TiO_2 films were then dipped into 0.3 mM dye solutions in ethanol for 24 h. Then rinsed with ethanol twice to remove physisorbed dyes, and dried with a flow of N_2 at ambient temperature.

6.3 Results and Discussion

Electronic Effects. To assess the electronic influence of the varying degrees of thiol- and catechol-substitutions on the porphyrin chromophore, we determined their UV-vis and fluorescence emission spectra and their reduction potentials by cyclic voltammetry (CV), and compared the data to literature-known data of the parent porphyrin **5**.[123, 130] Since most compounds only shown ill-resolved quasi-reversible and irreversible oxidations, thus omitted from detailed discussion. All cyclic voltammograms and the corresponding absorption combined with fluorescence graphs of each porphyrin derivatives were listed in Figure 6-2.

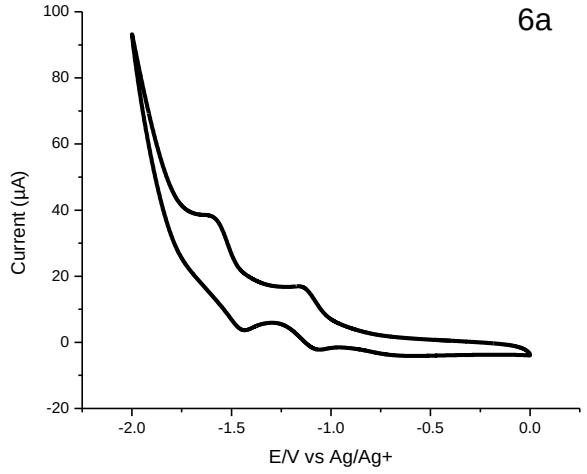
6a
Current (μA)
E/V vs Ag/Ag+

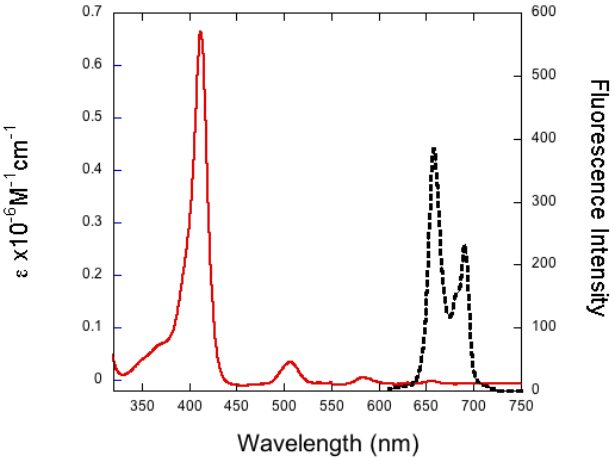
ε x10-6M-1cm-1
Fluorescence Intensity
Wavelength (nm)

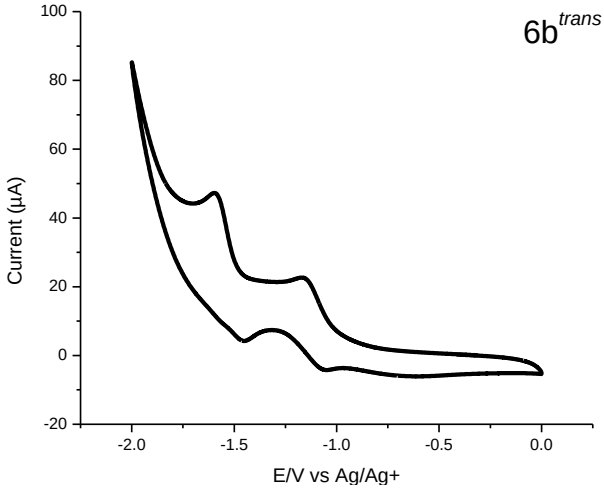
6btrans
Current (μA)
E/V vs Ag/Ag+

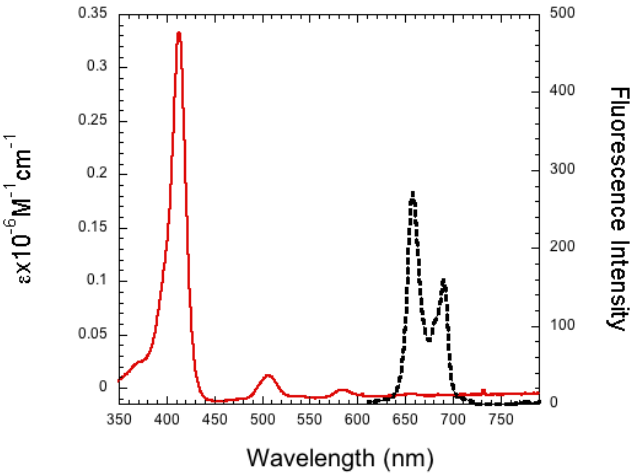
εx10-6M-1cm-1
Fluorescence Intensity
Wavelength (nm)

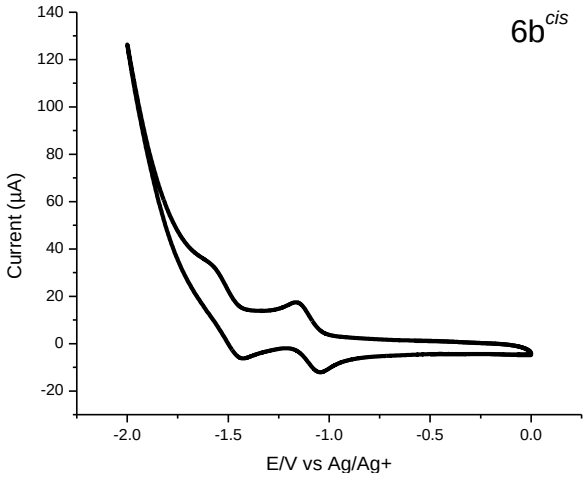
6bcis
Current (μA)
E/V vs Ag/Ag+

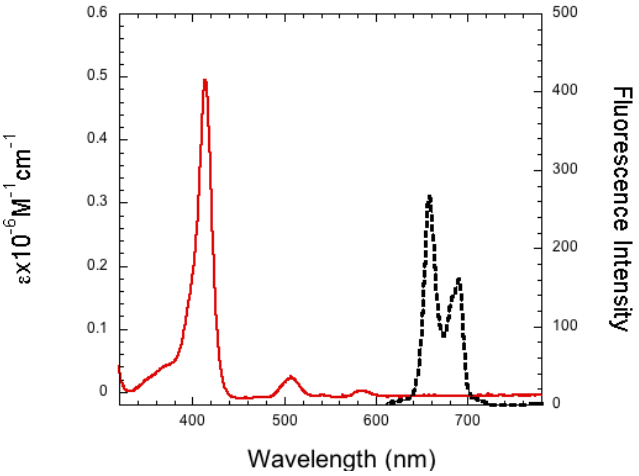
εx10-6M-1cm-1
Fluorescence Intensity
Wavelength (nm)

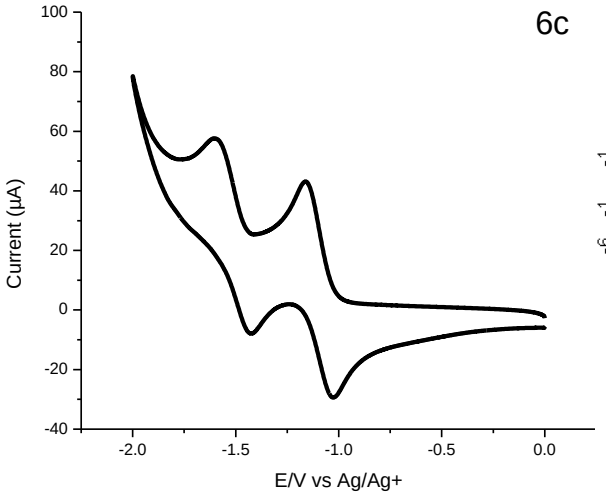
6c
Current (μA)
E/V vs Ag/Ag+

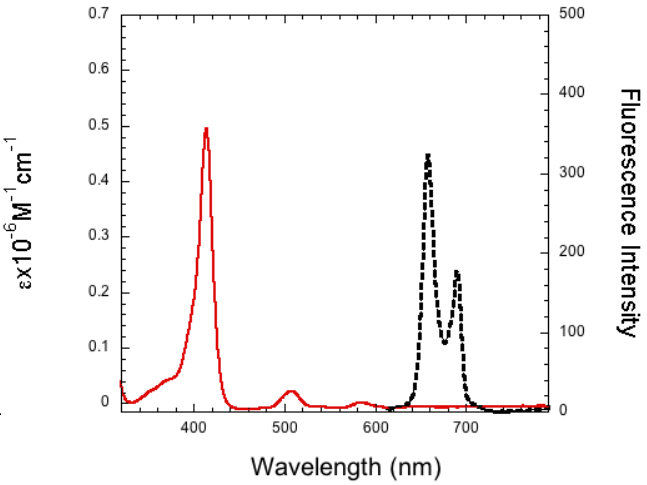
εx10-6M-1cm-1
Fluorescence Intensity
Wavelength (nm)

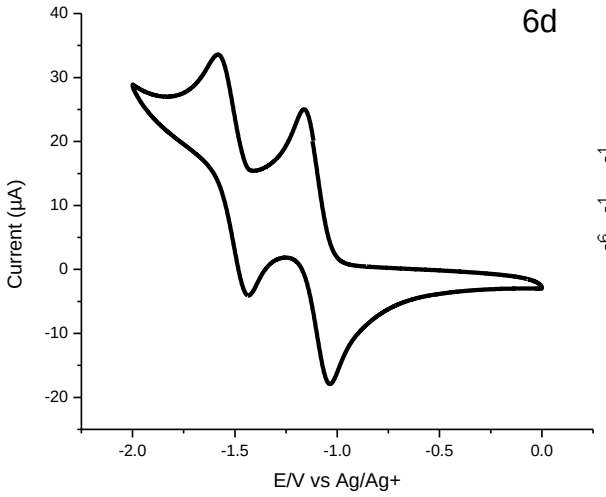
6d
Current (μA)
E/V vs Ag/Ag+

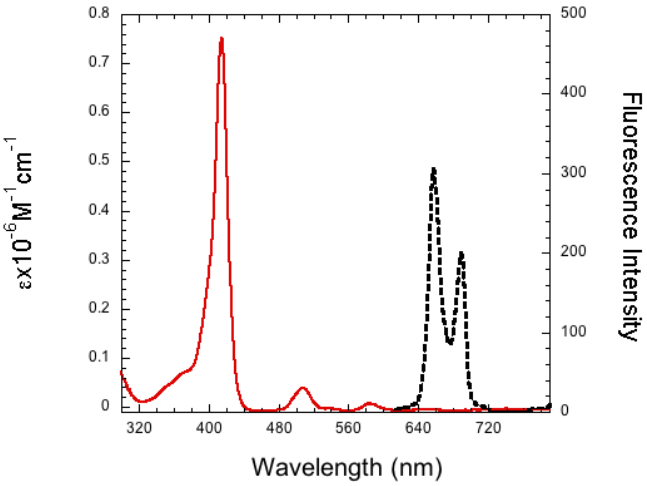
εx10-6M-1cm-1
Fluorescence Intensity
Wavelength (nm)

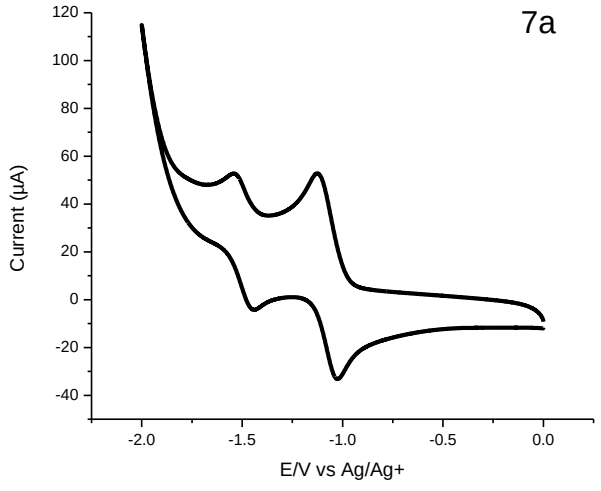
7a
Current (μA)
E/V vs Ag/Ag+

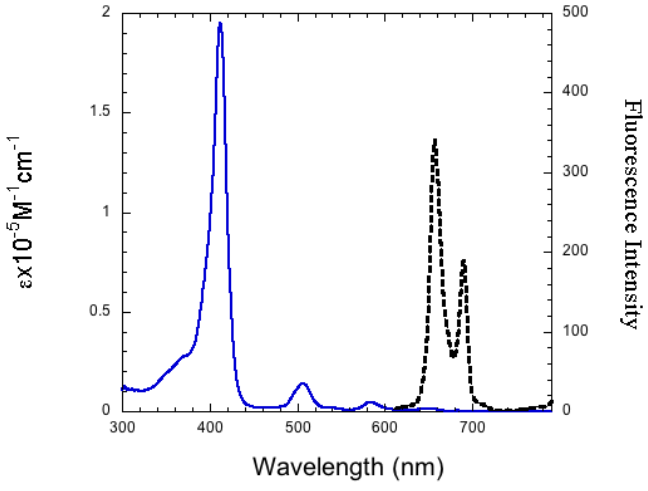
εx10-5M-1cm-1
Fluorescence Intensity
Wavelength (nm)

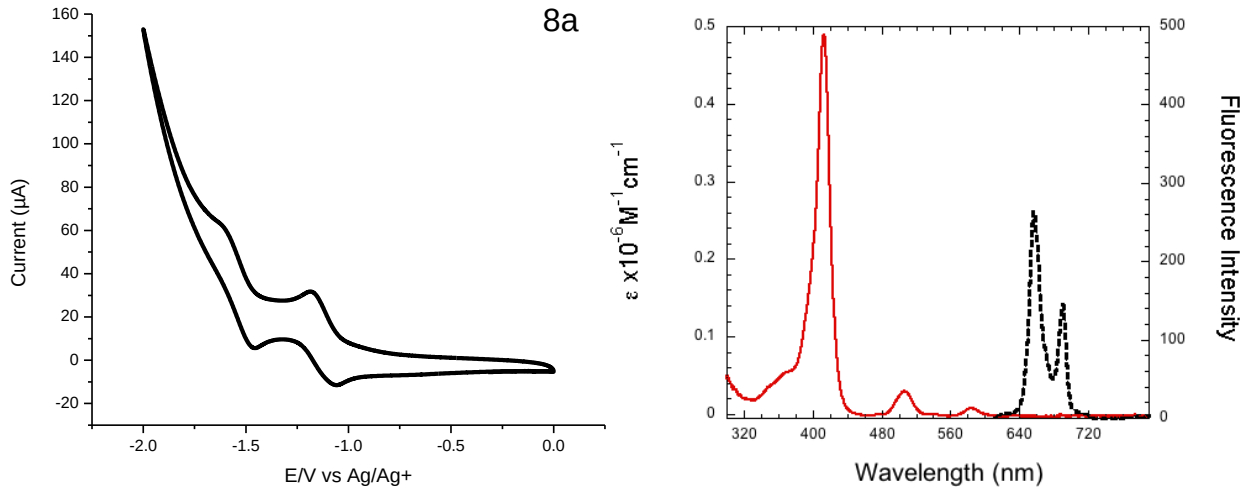
8a
Current (μA)
E/V vs Ag/Ag+
ε x10-6M-1cm-1
Fluorescence Intensity
Wavelength (nm)

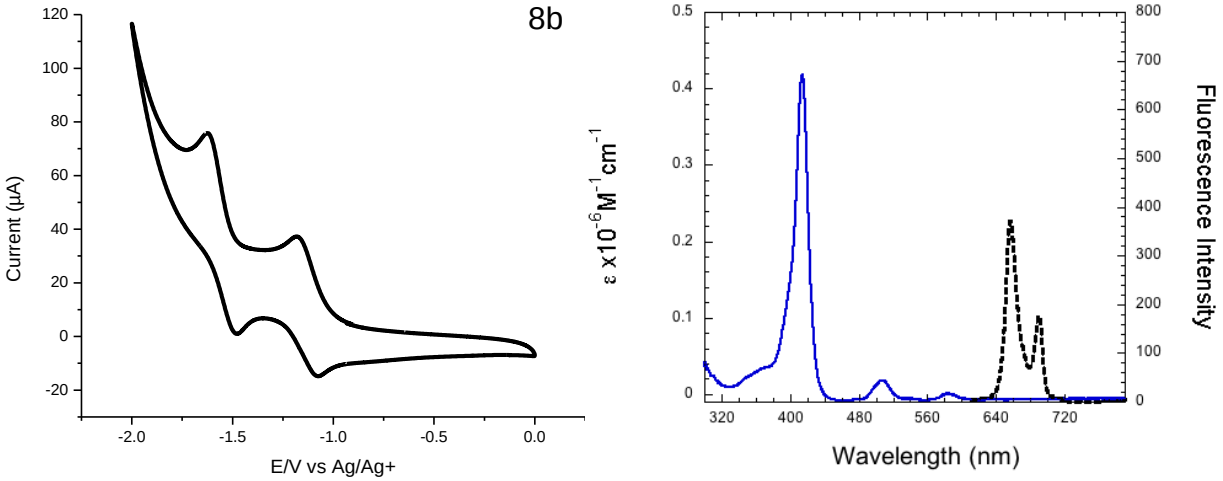
8b
Current (μA)
E/V vs Ag/Ag+
ε x10-6M-1cm-1
Fluorescence Intensity
Wavelength (nm)

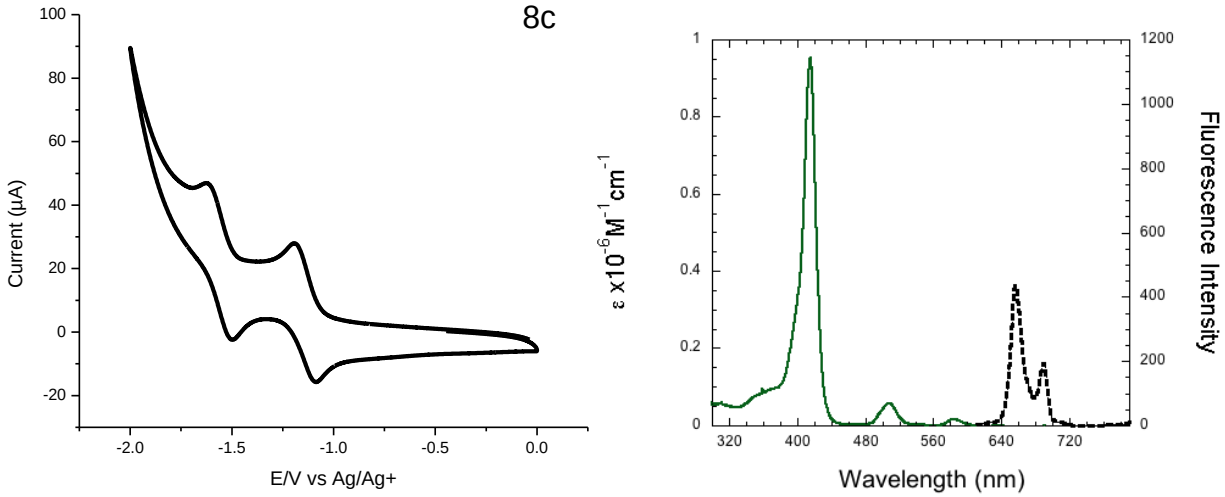
8c
Current (μA)
E/V vs Ag/Ag+
ε x10-6M-1cm-1
Fluorescence Intensity
Wavelength (nm)

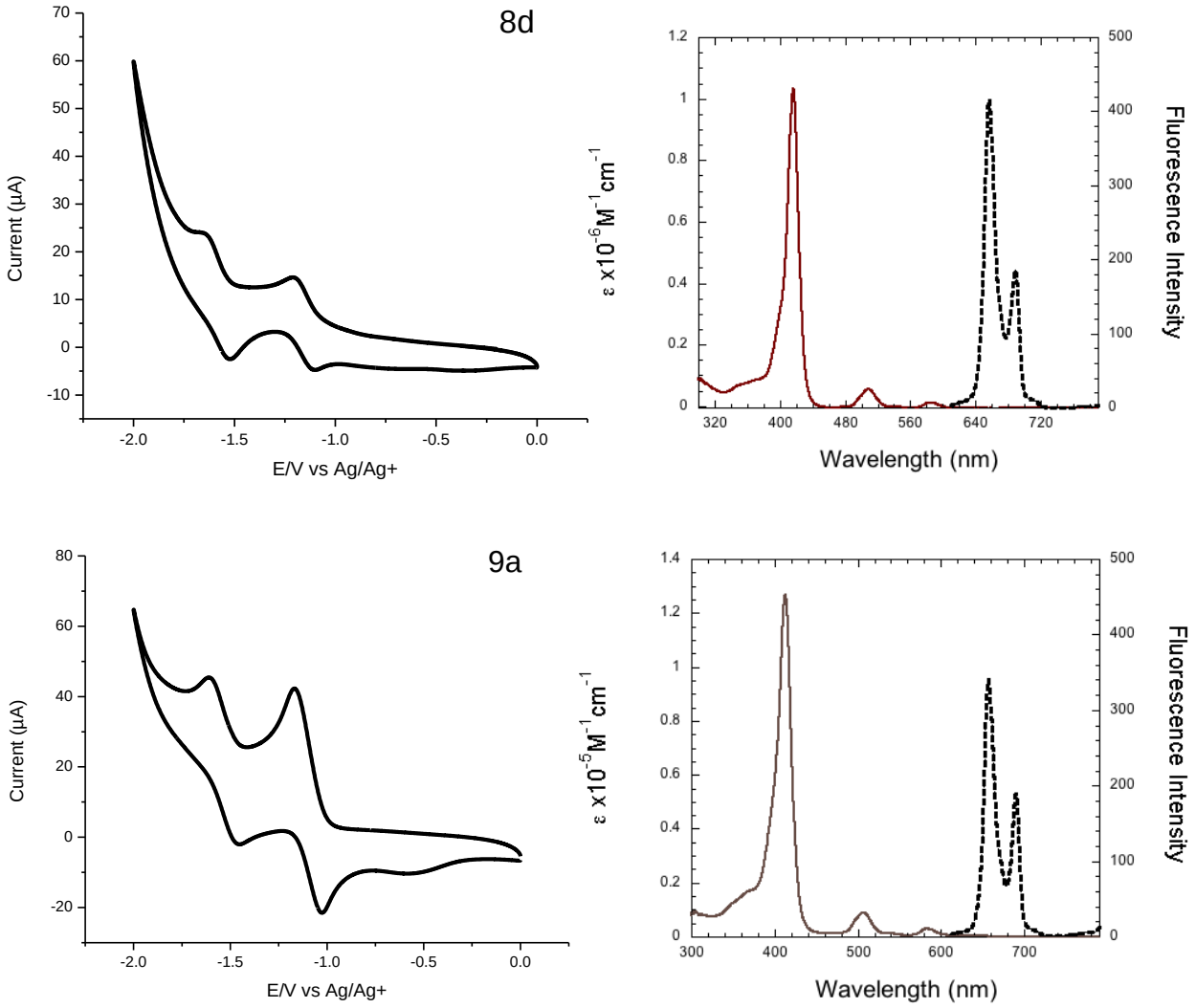

Figure 6-2. Cyclic voltammograms of porphyrin compounds indicated and their corresponding absorption and fluorescence graphs

Based on the cyclic voltammograms (Figure 6-3), all compounds showed similar reduction potentials, which were all similar to the parent compound, $T^{F}PP$, indicating the limited influence of electronic properties upon substitution. The electrochemistry of monosubstituted acids and esters were analyzed and no significant changes were observed as the result of the change of functionality. The reduction potentials of each dye molecule were calculated by cyclic voltammetry, which are all listed in Table 6-1 and Table 6-2.

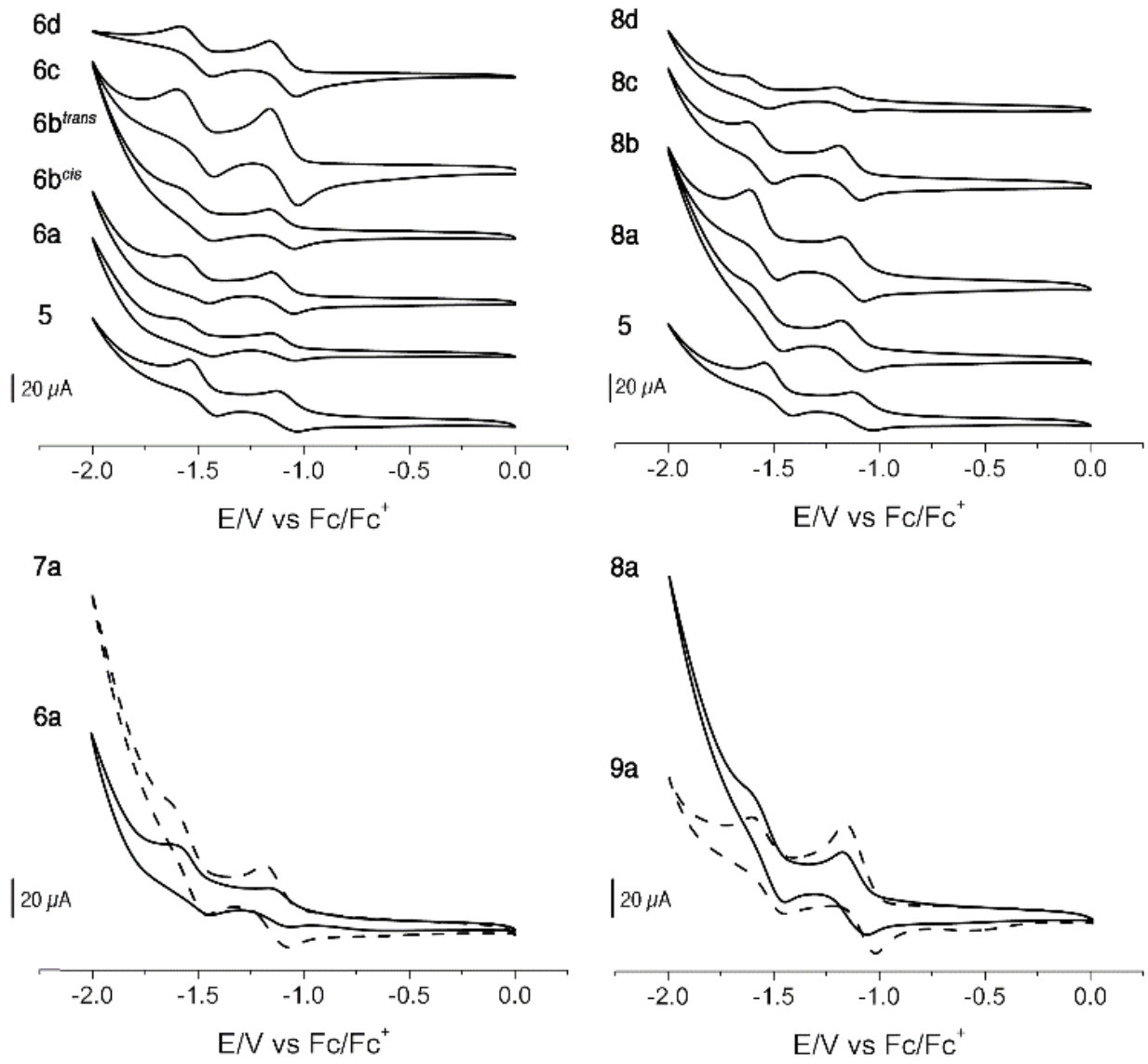

Figure 6-3. Cyclic voltammograms of the compounds indicated. Conditions: 1 mM porphyrin 0.1 M $TBAPF_6$ in dry CH_2Cl_2. Pt working and counter electrodes, 200 mv/s scan speed.

Table 6-1. UV-vis absorption, fluorescence emission

Compound	Absorption/nm (log ε/M^{-1} cm^{-1})	Fluorescence emission/nm (rel, I)
5	411 (5.64), 506 (4.41), 582 (3.78)	642, 707 (1:2)
6a	412 (5.82), 507 (4.53), 584 (3.69)	641, 706 (1:2)
6b^{trans}	413 (5.52), 507 (4.08), 585 (3.70)	642, 706 (1:2)
6b^{cis}	415 (5.88), 508 (4.59), 582 (3.84)	643, 706 (1:2)
6c	414 (5.69), 507 (4.34), 584 (3.30)	643, 707 (1:2)
6d	415 (5.87), 508 (4.59), 583 (3.84)	645, 707 (1:2)
7a	412 (5.29), 506 (4.15), 583 (3.65)	642, 707 (1:2)
8a	415 (5.37), 505 (4.25), 585 (3.81)	641, 708 (1:2)
8b	415 (5.10), 510 (3.91), 585 (3.45)	643, 707 (1:2)
8c	415 (5.49), 510 (4.40), 585 (3.92)	643, 707(1:2)
8d	415 (5.31), 510 (4.13), 585 (3.63)	644, 707(1:2)
9a	413 (5.10), 506 (3.95), 583 (3.48)	641, 707 (1:2)

Table 6-2. Reduction potentials as determined by CV of the derivatives investigated

Compound	Reduction Potentials/V		
	$E_{red1}^{1/2}$	$E_{red2}^{1/2}$	ΔE
5	-1.292	-1.753	0.46
6a	-1.324	-1.740	0.42
6b^{trans}	-1.324	-1.794	0.47
6b^{cis}	-1.318	-1.734	0.42
6c	-1.307	-1.728	0.42
6d	-1.315	-1.727	0.41
7a	-1.289	-1.703	0.41
8a	-1.712	-1.761	0.42
8b	-1.688	-1.758	0.42
8c	-1.712	-1.777	0.42
8d	-1.769	-1.809	0.43
9a	-1.313	-1.703	0.43

Binding to Metal Oxide Surfaces. The ability of the carboxyl modified porphyrin to adhere to semiconductor surface was also been studied. The immediate dark brown colors shows of the TiO_2 surface combined with the UV-vis spectra of the solid samples prepared in dilute solutions indicating that the acid derivatives bind to the metal oxide surfaces (Figure 6-4). This makes it possible to test these molecules as dyes in DSC devices.

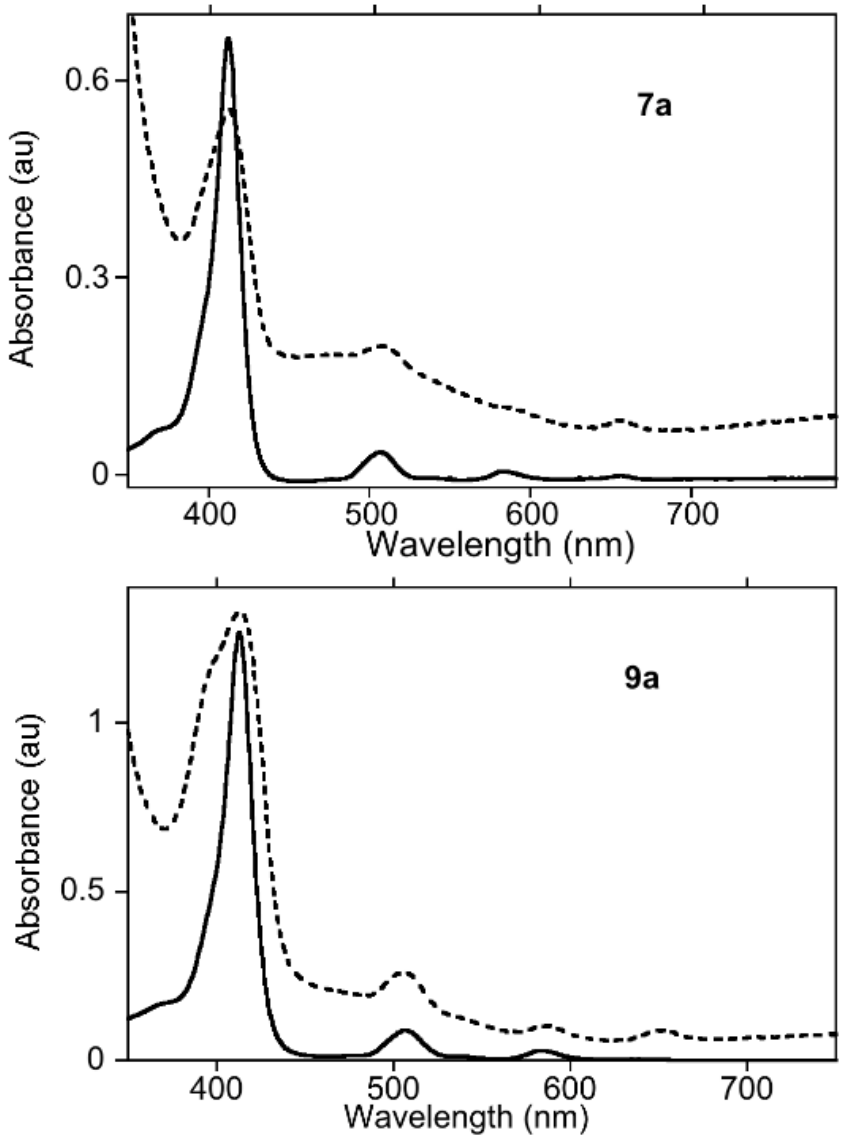

Figure 6-4. Normalized UV-vis spectra of 7a (top) and 9a (bottom) in CH_2Cl_2 (solid trace) and adsorbed onto TiO_2 nanoparticles (dotted trace) on an FTO-covered glass slide

Dye-Sensitized Solar Cell Device Performance. Dye-sensitized solar cells were made using the porphyrin derivatives. The current-voltage curves were shown in Figure 6-5 and the efficiencies were shown in Table 6-3. Comparing the redox potentials of these porphyrin compounds (between -1.29 V and -1.77 V) with that of the conduction band of TiO_2 (-0.57 V), there is a large energy difference between the excited dye (LUMO) and the conduction band energy level of TiO_2 (electron injection overpotential) for dye injection, which explains the low efficiencies of the DSC devices made by those porphyrin derivatives.

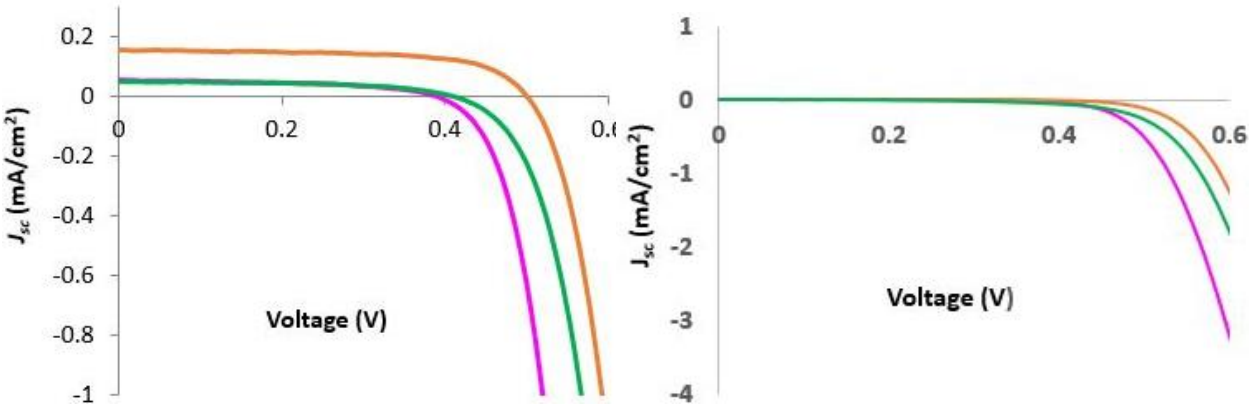

Figure 6-5. Current-voltage of solar cells under one sun (left) and dark (right), with different modified T^FPP derivatives, (orange) **6a**, (green) **6b**, and (pink) **6c** on TiO_2 working electrodes

Table 6-3. Current density (J_{sc}), open-circuit voltage (V_{oc}), fill factor (FF) and efficiency of solar cell devices with different modified T^FPP derivatives on TiO_2 working electrodes

	J_{sc} (mA/cm^2)	V_{oc} (V)	FF	Efficiency (%)
6a	0.07	0.39	0.49	0.01
6b	0.18	0.50	0.67	0.06
6c	0.07	0.41	0.54	0.01

6.4 Conclusions

Due to the energy mismatch between our modified T^FPP derivatives and semiconductor materials, TiO_2, these porphyrin derivative dye molecules do not perform well in DSCs. But this research finds that for a same chromophore, electrochemical potentials are essentially identical between ester and their corresponding acid. In addition, among these porphyrin compounds, different numbers of substituents are not affecting the energy levels of a dye. This at least suggests that if porphyrins with suitable electronic properties are identified, those properties are not perturbed by adding the groups necessary to bind the molecule to a TiO_2 surface for use in a DSC device.

CHAPTER 7. ELECTRONIC STRUCTURE OF SERIES OF *MESO*-PENTAFLUOROPHENYL-SUBSTITUTED CHLORINS AND BACTERIOCHLORINS THROUGH CHROMENE-ANNULATION

7.1 Synthesis of *meso*- C_6F_5-substituted chlorindiol and bacteriochlorintetraols

Our collaborator, Prof. Brückner's group,[1] and others, [131, 132] described the OsO_4-mediated dihydroxylation of *meso*-arylporphyrins to generate the corresponding dihydroxychlorins and tetrahydroxybacteriochlorins.[133] Using *meso*-C_6F_5-substituted porphyrin **4**, chlorin diol **5** and the two regioisomeric bacteriochlorins **6-*Z*** and **6-*E*** were thus formed (Scheme 7-1).[1, 2] The two bacteriochlorins are differentiated by the relative orientation of the two *cis*-*vic*-diol functionalities that may be facing the same side defined by the idealized planar macrocycle (**6-*Z***), or opposing sides (**6-*E***). They also described a way to modify *meso*-C_6F_5-substituted dihydroxychlorin **5** and the two bacteriochlorins **6-*Z*** and **6-*E*** using intramolecular S_NAr displacements of an *o*-F of the *meso*-C_6F_5 groups by the neighboring alcohols, forming chromene-annulated chlorin **7** or chromene-annulated bacteriochlorins **8-*Z*** and **8-*E***, respectively (Scheme 7-1).[2, 134]

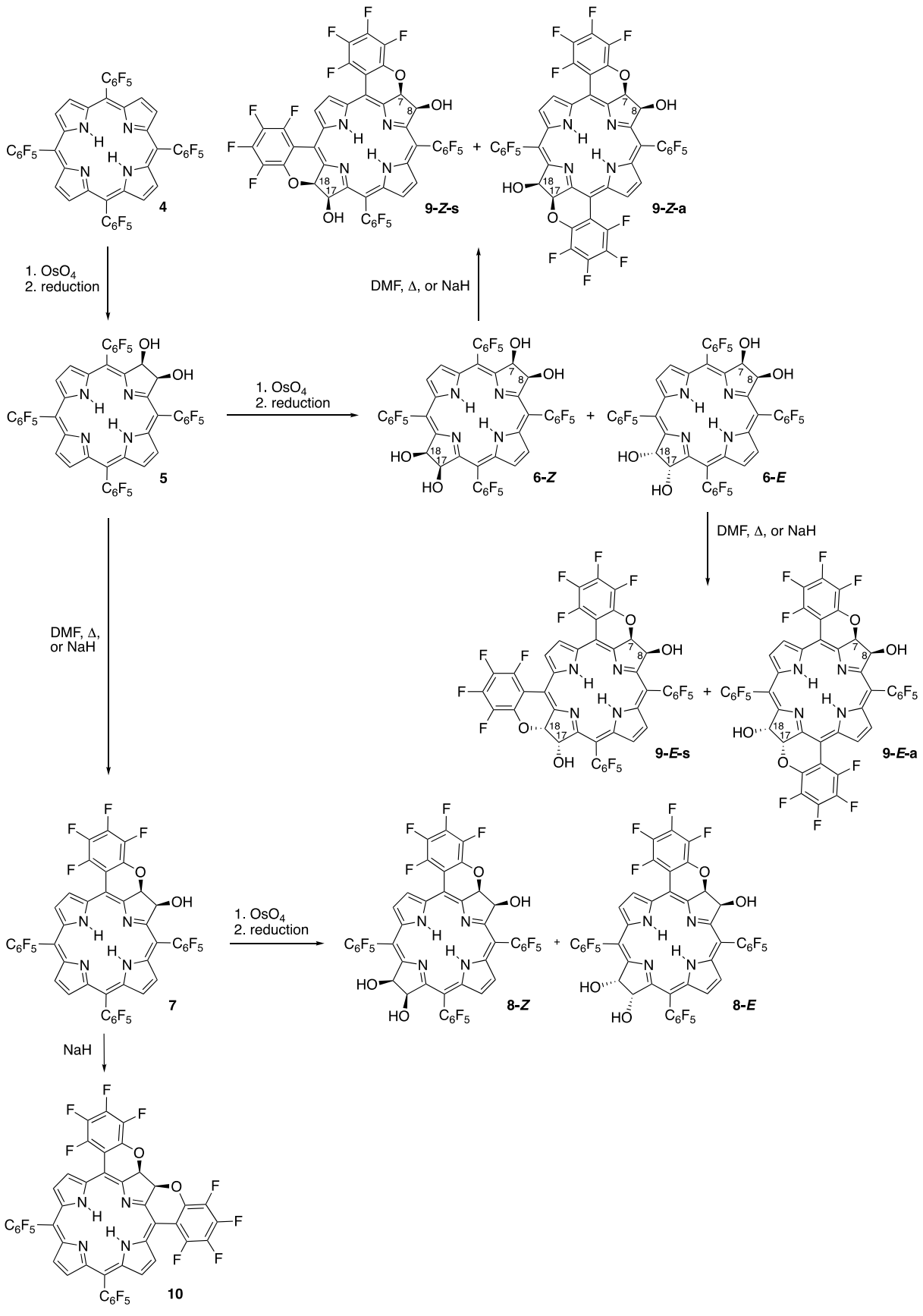
4
1. OsO4
2. reduction
5
1. OsO4
2. reduction
6-Z
6-E
DMF, Δ, or NaH
9-Z-s
9-Z-a
DMF, Δ, or NaH
9-E-s
9-E-a
DMF, Δ,
or NaH
7
1. OsO4
2. reduction
8-Z
8-E
NaH
10

Scheme 7-1. Syntheses of chlorindiol **5** and bacteriochlorintetraols **6-Z** and **6-E** by OsO_4-mediated dihydroxylation of porphyrin **4**,[1] and generation of mono-chromene-annulated chlorin **7**[2] and stereoisomeric bacteriochlorins **8-Z** and **8-E**, and the regioisomeric bis-chromene-annulated bacteriochlorins **9**.[134]

7.2 Characterization

UV-vis. The optical data of all chromophores compared were recorded in CH_2Cl_2 at ambient temperature on a Cary 50 UV-vis absorption spectrophotometer or Cary Eclipse fluorescence spectrophotometer.

Electrochemistry. The CV measurements of all the porphyrins were recorded on a CHI 600D electrochemical analyzer, with a standard three-electrode cell assembly. The supporting electrolyte was 0.1 M tetrabutylammonium hexafluorophosphate ($TBAPF_6$) dissolved in dry CH_2Cl_2. Platinum wires served as working and counter electrodes. An Ag/Ag^+ couple was used as the reference electrode. All porphyrins were measured at a concentration of ~1 mM and at a scan rate of 200 mV/s. Prior to scanning, the solutions were sparged with purified N_2 for 5 min.

7.3 Results and Discussion

UV-vis Spectra. The general appearance of the UV-vis absorption spectra of the chromene-annulated hydroporphyrins clearly reflect their nature as chlorins or bacteriochlorins (Figure 7-1, Table 7-1).[2, 134] The effects of the chromene-annulation are clearly visible within each class of hydroporphyrins: Chlorins of type **7** or **10** are characterized by red-shifted optical spectra when

compared to the non-annulated starting materials (16 nm for the conversion of chlorin **5** to mono-fused **7** and an additional 8 nm for the second fusion in **10**).

The optically observed red-shifts among the bacteriochlorin series upon chromene-annulation are larger than in the chlorin series (mono-fused bacteriochlorin **8-*Z*** shows a ~13 nm red-shift compared to the parent bacteriochlorin **7**, while double chromene-annulation leads to a 29/32 nm red-shift for **9-*Z*-*s*/9-*Z*-*a***). This is likely because hydroporphyrinoid flexibility increases with their increasing degree of saturation.[135] Thus bacteriochlorins are susceptible to larger deformations upon annulation, and these deformations tend to lift the HOMO levels.[136, 137] In addition to the lowered LUMO levels this results in a larger red-shift per annulation in the bacteriochlorins compared to the chlorins. Small but clearly distinguishable differences seen between the absolute positions of the frontier orbitals in the two regioisomers are interpreted to be the result of their differing conformations.[134]

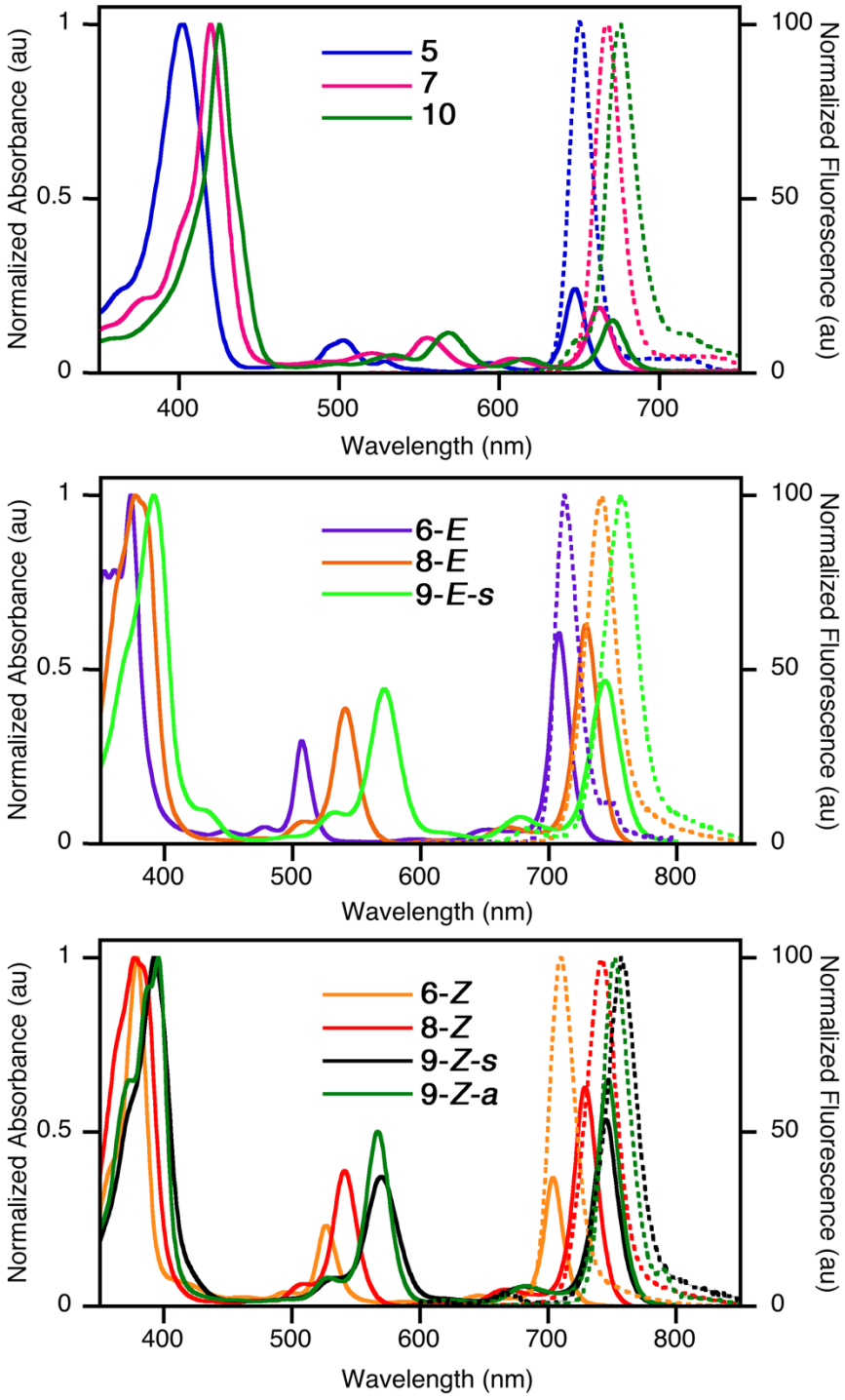

Figure 7-1. Overlay of the UV-vis absorption and normalized fluorescence emission spectra spectra (CH_2Cl_2, 25°C) of the hydroporphyrins indicated; $\lambda_{excitation} = \lambda_{Soret}$.

Table 7-1. Optical parameters of the compounds investigated

Compound[a]	**UV-vis Absorption Spectrum λ_{max} ($Q_y(0,0)$/ nm (log ε)**	**Fluorescence Emission λ_{max}/nm ($\lambda_{excitation} = \lambda_{Soret}$)**	**Q-state energy**[c] **(eV)**	**Fluorescence Emission Quantum yield (φ)**	**Fluorescence Lifetime ± 10% (ns)**
P **4**[b]	654 (2.63)	657	1.89	0.13	9.3
C diol **5**	647 (4.63)	649	1.91	0.34	6.9
Mono-fused C diol **7**	663 (4.70)	668	1.89	0.17	3.1
Bis-fused C diol **10**	671 (4.50)	676	1.84	0.20	3.6
BC tetraol **6-*Z***	708 (4.74)	712	1.75	0.01	4.0
BC tetraol **6-*E***	716 **(**4.32)	728	1.72	0.01	3.2
Mono-fused BC **8-*Z***	729 (5.02)	740	1.69	0.06	3.0
Mono-fused BC **8-*E***	729 (5.05)	740	1.69	0.06	3.3
Bis-fused BC **9-*Z*-*s***	745 (5.05)	760	1.65	0.05	3.6
Bis-fused BC **9-*E*-*s***	746 (4.98)	761	1.65	0.03	2.7
Bis-fused BC **9-*Z*-*a***	748 (5.06)	759	1.65	0.06	2.9

[a] All values in CH_2Cl_2 at ambient T [b] From ref. 55. [c] Average energy of the $Q_y(0,0)$ absorption and fluorescence bands

P = porphyrin, C = chlorin, BC = bacteriochlorin

DFT Calculations. The DFT-computed electronic structures of the investigated chlorins and bacteriochlorins shown in Table 7-2 and Figure 7-2 were confirmed by one of our collaborators, Matthew J. Guberman-Pfeffer in Prof. Gascon's group.

Table 7-2. Computed HOMO and LUMO energies (in eV) as per DFT

Compound[a]	**HOMO-1**	**HOMO**	**LUMO**	**LUMO+1**	**HOMO-LUMO gap**
C diol **5**	-6.36	-6.17	-3.56	-3.06	2.61
Mono-fused C diol **7**	-6.28	-6.17	-3.66	-3.07	2.51
Bis-fused C diol **10**	-6.21	-6.11	-3.72	-3.14	2.39
BC tetraol **6-*Z***	-6.46	-6.01	-3.74	-2.62	2.26
BC tetraol **6-*E***	-6.46	-6.01	-3.75	-2.62	2.26
Mono-fused BC **8-*Z***	-6.37	-6.00	-3.85	-2.63	2.15
Mono-fused BC **8-*E***	-6.35	-6.01	-3.84	-2.64	2.17
Bis-fused BC **9-*Z*-*s***	-6.24	-5.94	-3.85	-2.58	2.09
Bis-fused BC **9-*E*-*s***	-6.23	-5.93	-3.86	-2.59	2.08
Bis-fused BC **9-*Z*-*a***	-6.20	-5.91	-3.82	-2.68	2.09

[a] C = chlorin, BC = bacteriochlorin

As generally observed for bacteriochlorins compared to chlorins,[138] and reflected in the differing UV-vis spectra of these two hydroporphyrin classes (Figure 7-1 and Table 7-1), their HOMO-LUMO gap is narrowed because of a significant lowering of the LUMO and a minor lifting of the

HOMO, whereas the LUMO+1 is significantly lifted (giving rise to the generally blue-shifted Soret band of the bacteriochlorins).[138] The experimentally obtained HOMO-LUMO energy gaps are comparable to the literature data (1.35-1.45 eV for the bacteriochlorins and 1.72-1.98 eV for the chlorins),[139, 140, 141] indicating that the HOMO-LUMO energy gap of the hydroporphyrins is not much affected by the presence of the *meso*-pentafluorophenyl groups. However the absolute position of the frontier orbitals is somewhat lowered, as also observed for the parent porphyrins.[123] The increasing number of chromene-annulations leads to successive destabilization of the HOMO as well as stabilization of the LUMOs (as seen, e.g., in the series **5** $\rightarrow$ **7** $\rightarrow$ **10**). The frontier orbital levels of the comparable regioisomeric *E*- and *Z*-series (e.g. **9-*E*-*s*** vs. **9-*Z*-*s***) are essentially identical, but the isomers within each series (e.g. **9-*E*-*s*** vs. **9-*E*-*a***) differ slightly on account of their slightly differing conformations.[134] Overall, the DFT calculations faithfully reproduce the experimental electrochemical data presented in detail below and trends observed by UV-vis spectroscopy.

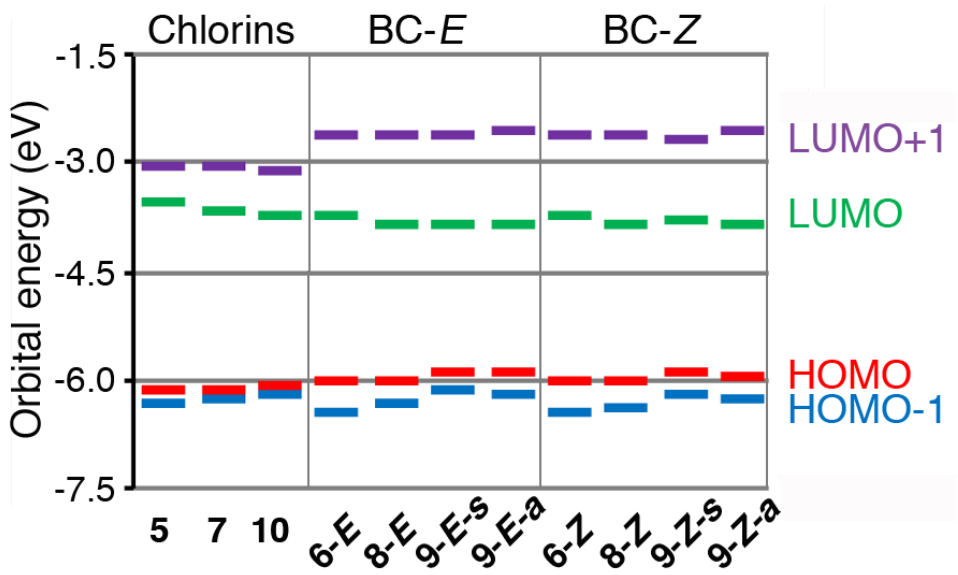

Figure 7-2. Graphical representation of the frontier energy levels of the hydroporphyrins calculated

Electrochemistry. Cyclic voltammograms for all compounds were recorded (Figure 7-3) and relative HOMO-LUMO band gap energies were calculated based on the electrochemical data (Table 7-3). Except for bacteriochlorin tetraol **6-*E*** and bis-linked bacteriochlorin **9-*Z*-a**, all compounds undergo two reversible reductions forming stable radical anions and dianions. The bacteriochlorins **6-*E*** and **9-*Z*-a** show only quasi-reversible or fully irreversible reductions; these compounds are thus omitted from detailed discussion. We previously observed the surprisingly distinct chemical reactivity and conformations of the two bacteriochlorin tetraol isomers **6-*E*** and **6-*Z***.[1] For chlorins **5**, **7**, and **8-*E*,** the first oxidation couples are reversible, however other compounds only show ill-resolved quasi-reversible or irreversible oxidations, a common observation for free-base porphyrins and hydroporphyrins.[142] The derived general lower LUMO and higher HOMO levels of the bacteriochlorins compared to the chlorins are as expected based on the nature of the hydroporphyrins.[138] Thus, chromene-annulation also does not change the native electrochemical characteristics of the parent hydroporphyrins.

In comparison of the HOMO-LUMO energy gaps between electrochemical measurements and DFT calculations, shown in Figure 7-4, we find that the optical and electrochemical energy gaps are similar to each other (differences within 0.2 eV), while the computed energy gap was over-estimated by 0.5-0.9 eV, which is within the acceptable energy difference ranges between the evaluated and experimental measurements based on pervious literatures.[143, 144]

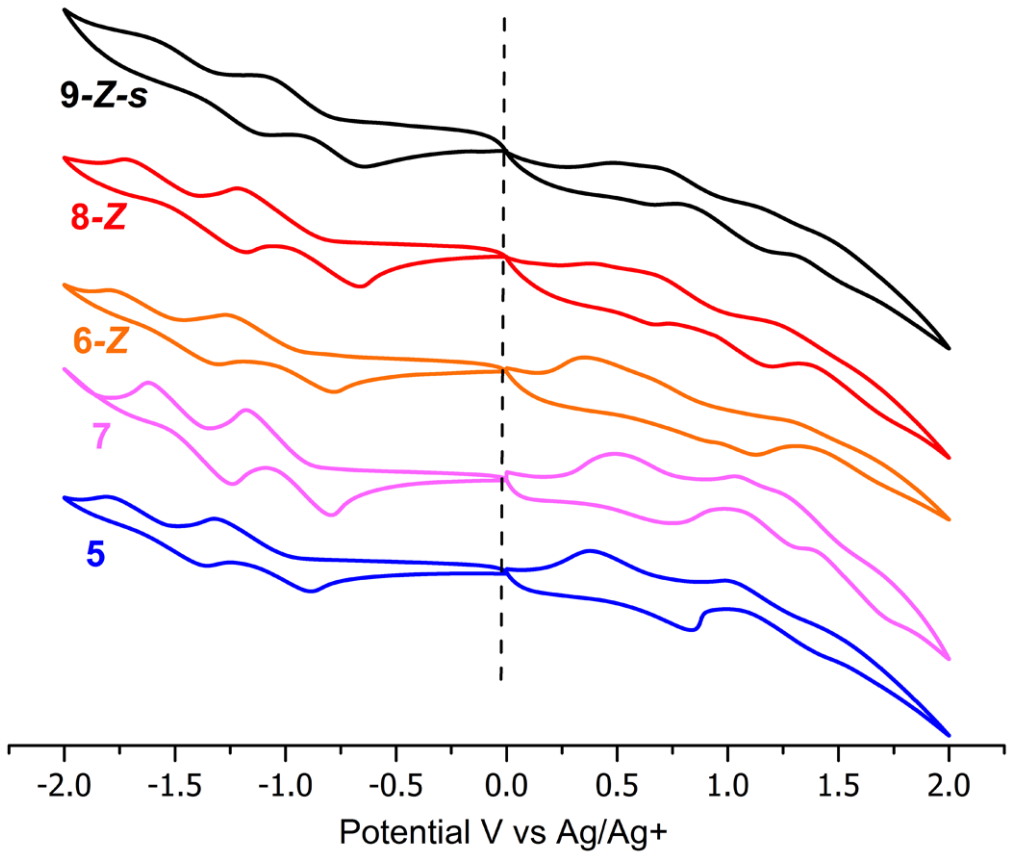

Figure 7-3. Representative cyclic voltammograms of the compounds indicated (dry CH_2Cl_2, 0.1 M $TBAPF_6$, [X] ~ 10^{-3} M, scan rate of 200 mV/s)

Table 7-3. Electrochemical half-wave potentials of the compounds investigated

Compound[a]	Reduction		Oxidation		HOMO-LUMO gap
	$E_{red2}^{1/2}$	$E_{red1}^{1/2}$	$E_{ox1}^{1/2}$	$E_{ox2}^{1/2}$	
C diol **5**	-3.48	-3.94	-5.67	-6.26	1.73
Mono-fused C diol **7**	-3.63	-4.07	-5.69	-6.24	1.62
Bis-fused C diol **10**	-3.50	-3.88	(-5.60)[c]	(-6.10)[c]	(1.72)[c]
BC tetraol **6-*Z***	-3.51	-4.06	-5.68	-5.97	1.62
BC tetraol **6-*E***	(-3.75)[c]	(-4.15)[c]	(-5.84)[c]	(-5.92)[c]	(1.69)[c]
Mono-fused BC **8-*Z***	-3.61	-4.12	-5.59	-6.00	1.47
Mono-fused BC **8-*E***	-3.64	-4.15	-5.68	-6.20	1.53
Bis-fused BC **9-*Z*-*s***	-3.72	-4.20	-5.64	-6.02	1.44
Bis-fused BC **9-*E*-*s***	-3.73	-4.21	-5.66	-6.00	1.45
Bis-fused BC **9-*Z*-*a***	-	-3.83	-5.40	-	1.57

[a] C = chlorin, BC = bacteriochlorin

[b] Measured reduction and oxidation potentials were referenced to Fc/Fc+, converted using E_{Fc/Fc^+} = +0.63V vs NHE, then converted to eV using a vacuum level potential of -4.44 V vs NHE, for ease of comparison with computed energy levels. For a table of the data in V vs. NHE see ESI.

[c] Unreliable data based on irreversible, ill-defined peaks.

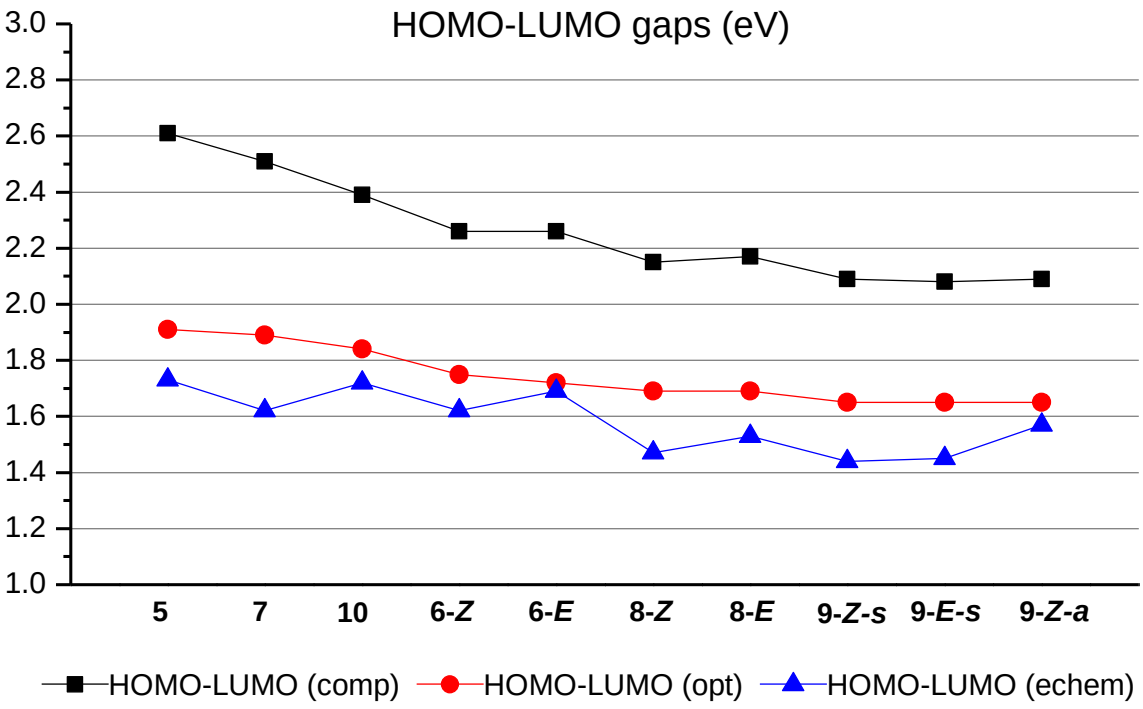

Figure 7-4. Comparison of HOMO and LUMO levels by computation (comp) or electrochemistry (echem) (based on oxidation and reduction potentials, respectively)

7.4 Conclusions

In conclusion, we demonstrate the limited electronic modulations can be tuned through chromene-annulation, with the comparison of the experimental determination of their optical properties and electrochemical properties examined by absorption and fluorescence spectroscopy and cyclic voltammetry, respectively. And small modulations of the frontier orbitals of the porphyrinoids are rationalized using DFT computations and can be traced to small electronic effects due to the co-planarized *meso*-aryl groups in combination with conformational effects.

CHAPTER 8. SUMMARY

The main objective of this thesis was to improve the performance of dye-sensitized solar cells by either reducing the energy loss in redox reactions using platinum nanoparticles or utilizing modified strongly light-absorbing novel porphyrinoid molecules to work as sensitizers in the DSC devices.

First of all, in Chapter 4, the comparison of the organometallic assemblies binding between Pt metal and the S atoms from either thiol group or disulfide group has been investigated. And the formation between Pt metal and S atoms of 4-mercaptobenzoic acid is confirmed by three different techniques: cyclic voltammetry, Raman spectroscopy and X-ray photoelectron spectroscopy. In addition, the formation of the assembly of TiO_2–4MBA–Pt has been developed and the result demonstrates that the binding of 4-MBA to Pt can increase the catalytic activity of iodide/triiodide redox couple in the electrolyte. Therefore, it paves a way for future enhancement on improving solar power conversion efficiency of DSCs by using target bifunctional dyes.

Then in Chapter 5, we first of all, anchored the model molecule, 4-MBA, to a TiO_2 surface, bound Pt nanoparticles to them, formed a demo system, TiO_2–4MBA–Pt, and also measured the catalytic capability of Pt in this assembly. Then we made the assembly with our bifunctional dye to replace the 4MBA, formed TiO_2–dye–Pt and built DSC devices. An enhancement in efficiency of solar cell devices has been investigated with a binding through Pt–S bond, by binding the Pt nanoparticles to a bifunctional N3-type complex, with one bipyridyl ligand modified with 4-mecaptobenzoic acid units to bind to the Pt nanoparticles, and another bipyridyl ligand modified by –COOH groups to attach to the TiO_2 surface. In devices made at EPFL, the addition of Pt NPs led to a near-50% decrease in efficiency in the reference dye, due to the decrease in both J_{sc} and

V_{oc}, indicating a fast recombination between the TiO_2 surface and the dissolved redox couple catalyzed by Pt nanoparticles. However, from the perspective of , the efficiency of the DSC devices with the bifunctional dye, $Ru(dcb)(4MA)(NCS)_2$,was enhanced by 21% by Pt NPs, due to the increased J_{sc} with no loss of V_{oc}. This suggests that the dye successfully blocked Pt NPs from making direct contact with the TiO_2 surface, while the dye itself bound Pt NPs via its thiol group. However, experiments at UConn saw the same performance decrease from the bifunctional dye as in the reference dye. This is likely due to differences in the procedures used in the two laboratories resulting in different character of the TiO_2 surface and different degrees of dye loading leaving more TiO_2 exposed to direct contact with Pt in the UConn experiments. Therefore, more experiments and characterizations need to be done in order to figure out the influence of the Pt nanoparticles in a DSC system with a bifunctional dye.

Lastly, in Chapter 6 and Chapter 7, electrochemical experiments have been done in order to investigate either the electronic effects of different substitutions and numbers of substitutions of modified T^FPP porphyrin derivatives or demonstrate the limited tunable electronic modulations of *meso*-pentafluorophenyl-substituted bacteriochlorin derivatives through chromene-annulation. However, these porphyrin dye molecules were not suitable for making DSC devices due to the energy mismatch.

Overall, in this work, we have successfully proved the binding between Pt and S atom from thiol group, built the assembly of TiO_2–bifunctional dye–Pt and proved the efficiency enhancement with Pt nanoparticles binding through S atom on the bifunctional dye. But more research needs to be done in the future work. For example, examine the impact of Pt nanoparticles in a DSC device with a bifunctional dye under different conditions; demonstrate that if the Pt nanoparticles allow the bifunctional dye to be regenerated despite a small overpotential. In order to do that, we will

have to tune the oxidation potential of the dye to less than 0.5 V more positive than the iodide/triiodide redox couple. The electronic interactions between the dye and the Pt nanoparticles have to be controlled to enable electron transfer only from the Pt to the oxidized dye instead of the other way around. Optical and photoelectrochemical measurements will be developed on this assembly to examine where the oxidized dye can be reduced by the Pt nanoparticle and whether the photoexcited dye is quenched by the Pt. And finally, complete DSC devices to provide the proof-of-concept of using catalysis to solve the overpotential problem with low-cost.

CHAPTER 9. REFERENCES

1. Samankumara, L. P.; Zeller, M.; Krause, J. A.; Brückner, C. Syntheses, structures, modification, and optical properties of *meso*-tetraaryl-2,3-dimethoxychlorin, and two isomeric meso-tetraaryl-2,3,12,13-tetrahydroxybacteriochlorins. *Organic and Biomolecular Chemistry* **2010,** *8* (8), 1951-1965.

2. Hyland, M. A.; Morton, M. D.; Brückner, C. *meso*-Tetra(pentafluorophenyl)porphyrin-derived Chromene-annulated Chlorins. *The Journal of Organic Chemistry* **2012,** *77* (7), 3038–3048.

3. O'Regan, B.; Grätzel, M. A low-cost, high-efficiency solar cell based on dye-sensitized colloidal TiO_2 films. *Nature* **1991,** *353* (6346), 737.

4. Kakiage, K.; Aoyama, Y.; Yano, T.; Oya, K.; Fujisawa, J. I.; Hanaya, M. Highly-efficient dye-sensitized solar cells with collaborative sensitization by silyl-anchor and carboxy-anchor dyes. *Chemical Communications* **2015,** *51* (88), 15894-15897.

5. Thakkar, V. N.; Parmar, H. R.; Nayak, J. S. GHG Tank : for Heat storage and utilization. *International Journal of Engineering Research & Technology* **2014,** *3* (11), 1131-1138.

6. REN21 Renewable 2014 Global Status Report.

7. Riordan, C.; Hulstron, R. What is an air mass 1.5 spectrum? *Photovoltaic Specialists Conference, Conference Record of the Twenty First IEEE* **1990**, 1085-1088.

8. Bell Labs Demonstrates the First Practical Silicon Solar Cell. *APS NEWS* **1954,** *18* (4).

9. Green, M. A. Third generation photovoltaics: advanced solar energy conversion. *Springer Series in Photonics* **2006,** *12*.

10. Leccisi, E.; Raugei, M.; Fthenakis, V. The energy and environmental performance of ground-mounted photovoltaic systems—A timely update. *Energies* **2016,** *9* (12), 622.

11. International Technology Roadmap for Photovoltaic (ITRPV). **2017,** *Eighth Edition*.

12. Baxter, J. B. Commercialization of dye sensitized solar cells: Present status and future research needs to improve efficiency, stability, and manufacturing. *Journal of Vacuum Science & Technology A: Vacuum, Surfaces, and Films* **2012,** *30* (2), 020801.

13. Hagfeldt, A.; Boschloo, G.; Sun, L.; Kloo, L.; Pettersson, H. Dye-sensitized solar cells. *Chemical Reviews* **2010,** *110* (11), 6595-6663.

14. Mozaffari, S.; Nateghi, M. R.; Zarandi, M. B. An overview of the challenges in the commercialization of dye sensitized solar cells. *Renewable and Sustainable Energy Reviews* **2017,** *71*, 675-686.

15. Grätzel, M. Solar energy conversion by dye-sensitized photovoltaic cells. *Inorganic Chemistry* **2005,** *44* (20), 6841-6851.

16. Boschloo, G.; Hagfeldt, A. Characteristics of the iodide/triiodide redox mediator in dye-sensitized solar cells. *Accounts of Chemical Research* **2009,** *42* (11), 1819-1826.

17. Huang, W. K.; Wu, H. P.; Lin, P. L.; Lee, Y. P.; Diau, E. W. Design and characterization of heteroleptic ruthenium complexes containing benzimidazole ligands for dye-sensitized solar cells: The effect of fluorine substituents on photovoltaic performance. *The Journal of Physical Chemistry Letters* **2012,** *3* (13), 1830-1835.

18. Nusbaumer, H.; Zakeeruddin, S. M.; Moser, J. E.; Grätzel, M. An alternative efficient redox couple for the dye-sensitized solar cell system. *Chemistry-A European Journal* **2003,** *9* (16), 3756-3763.

19. Nusbaumer, H.; Moser, J-E.; Zakeeruddin, S. M.; Nazeeruddin, M. K.; Grätzel, M. $Co^{II}(dbbip)_2^{2+}$ complex rivals tri-iodide/iodide redox mediator in dye-sensitized photovoltaic cells. *The Journal of Physical Chemistry B* **2001,** *105* (43), 10461-10464.

20. Bella, F.; Galliano, S.; Gerbaldi, C.; Viscardi, G. Cobalt-based electrolytes for dye-sensitized solar cells: recent advances towards stable devices. *Energies* **2016,** *9* (5), 384.

21. Daeneke, T.; Kwon, T. H.; Holmes, A. B.; Duffy, N. W.; Bach, U.; Spiccia, L. High-efficiency dye-sensitized solar cells with ferrocene-based electrolytes. *Nature Chemistry* **2011,** *3* (3), 211-215.

22. Zhang, Z.; Chen, P.; Murakami, T. N.; Zakeeruddin, S. M.; Grätzel, M. The 2,2,6,6-tetramethyl-1-piperidinyloxy radical: an efficient, iodine- free redox mediator for dye-sensitized solar cells. *Advanced Functional Materials* **2008,** *18* (2), 341-346.

23. Wang, M.; Chamberland, N.; Breau, L.; Moser, J. E.; Humphry-Baker, R.; Marsan, B.; Zakeeruddin, S. M.; Grätzel, M. An organic redox electrolyte to rival triiodide/iodide in dye-sensitized solar cells. *Nature Chemistry* **2010,** *2* (5), 385-389.

24. Chen, K. S.; Liu, W. H.; Wang, Y. H.; Lai, C. H.; Chou, P. T.; Lee, G. H.; Chen, K.; Chen, H. Y.; Chi, Y.; Tung, F. C. New family of ruthenium-dye-sensitized manocrystalline TiO_2 solar cells with a high solar-energy-conversion efficiency. *Advanced Functional Materials* **2007,** *17* (15), 2964-2974.

25. Chen, C. Y.; Wu, S. J.; Wu, C. G.; Chen, J. G.; Ho, K. C. A ruthenium complex with superhigh light-harvesting capacity for dye-sensitized solar cells. *Angewandte Chemie* **2006,** *118* (35), 5954-5957.

26. Polo, A. S.; Itokazu, M. K.; Iha, N. Y. M. Metal complex sensitizers in dye-sensitized solar cells. *Coordination Chemistry Reviews* **2004,** *248* (13-14), 1343-1361.

27. Mishra, A.; Fischer, M. K.; Bäuerle, P. Metal-free organic dyes for dye-sensitized solar cells: From structure: Property relationships to design rules. *Angewandte Chemie International Edition* **2009,** *48* (14), 2474-2499.

28. Horiuchi, T.; Miura, H.; Sumioka, K.; Uchida, S. High efficiency of dye-sensitized solar cells based on metal-free indoline dyes. *Journal of the American Chemical Society* **2004,** *126* (39), 12218-12219.

29. Wang, M.; Xu, M.; Shi, D.; Li, R.; Gao, F.; Zhang, G.; Yi, Z.; Humphry-Baker, R.; Wang, P.; Zakeeruddin, S. M. High-performance liquid and solid dye-sensitized solar cells based on a novel metal-free organic sensitizer. *Advanced Materials* **2008,** *20* (23), 4460-4463.

30. Yella, A.; Lee, H.-W.; Tsao, H. N.; Yi, C.; Chandiran, A. K.; Nazeeruddin, M. K.; Diau, E. W.-G.; Yeh, C.-Y.; Zakeeruddin, S. M.; Grätzel, M. Porphyrin-sensitized solar cells with cobalt (II/III)–based redox electrolyte exceed 12 percent efficiency. *Science* **2011,** *334* (6056), 629-634.

31. Bessho, T.; Zakeeruddin, S. M.; Yeh, C. Y.; Diau, E. W. G.; Grätzel, M. Highly efficient mesoscopic dye-sensitized solar cells based on donor–acceptor-substituted porphyrins. *Angewandte Chemie International Edition* **2010,** *49* (37), 6646-6649.

32. Campbell, W. M.; Jolley, K. W.; Wagner, P.; Wagner, K.; Walsh, P. J.; Gordon, K. C.; Schmidt-Mende, L.; Nazeeruddin, M. K.; Wang, Q.; Grätzel, M. Highly efficient porphyrin sensitizers for dye-sensitized solar cells. *The Journal of Physical Chemistry C* **2007,** *111* (32), 11760-11762.

33. Mathew, S.; Yella, A.; Gao, P.; Humphry-Baker, R.; Curchod, B. F.; Ashari-Astani, N.; Tavernelli, I.; Rothlisberger, U.; Nazeeruddin, M. K.; Grätzel, M. Dye-sensitized solar cells with 13% efficiency achieved through the molecular engineering of porphyrin sensitizers. *Nature Chemistry* **2014,** *6* (3), 242.

34. Lu, H. P.; Tsai, C. Y.; Yen, W. N.; Hsieh, C. P.; Lee, C. W.; Yeh, C. Y.; Diau, E. W. G. Control of dye aggregation and electron injection for highly efficient porphyrin sensitizers adsorbed on semiconductor films with varying ratios of coadsorbate. *The Journal of Physical Chemistry C* **2009,** *113* (49), 20990-20997.

35. Im, J. H.; Lee, C. R.; Lee, J. W.; Park, S. W.; Park, N. G. 6.5% efficient perovskite quantum-dot-sensitized solar cell. *Nanoscale* **2011,** *3* (10), 4088-4093.

36. Chang, C.-H.; Lee, Y.-L. Chemical bath deposition of CdS quantum dots onto mesoscopic TiO_2 films for application in quantum-dot-sensitized solar cells. *Applied Physics Letters* **2007,** *91* (5), 053503.

37. Santra, P. K.; Kamat, P. V. Mn-doped quantum dot sensitized solar cells: a strategy to boost efficiency over 5%. *Journal of the American Chemical Society* **2012,** *134* (5), 2508-2511.

38. Chen, C. Y.; Wang, M.; Li, J. Y.; Pootrakulchote, N.; Alibabaei, L.; Ngoc-le, C. H.; Decoppet, J. D.; Tsai, J. H.; Grätzel, C.; Wu, C. G.; Zakeeruddin, S. M.; Grätzel, M. Highly efficient light-harvesting ruthenium sensitizer for thin-film dye-sensitized solar cells. *ACS Nano* **2009,** 3 (10), 3103-3109.

39. Kuang, D.; Ito, S.; Wenger, B.; Klein, C.; Moser, J.-E.; Humphry-Baker, R.; Zakeeruddin, S. M.; Grätzel, M. High molar extinction coefficient heteroleptic ruthenium complexes for thin film dye-sensitized solar cells. *Journal of the American Chemical Society* **2006,** *128* (12), 4146-4154.

40. Haque, S. A.; Handa, S.; Peter, K.; Palomares, E.; Thelakkat, M.; Durrant, J. R. Supermolecular control of charge transfer in dye-sensitized nanocrystalline TiO_2 films: towards a quantitative structure–function relationship. *Angewandte Chemie International Edition* **2005,** *44* (35), 5740-5744.

41. Schmidt-Mende, L.; Kroeze, J. E.; Durrant, J. R.; Nazeeruddin, M. K.; Grätzel, M. Effect of hydrocarbon chain length of amphiphilic ruthenium dyes on solid-state dye-sensitized photovoltaics. *Nano Letters* **2005,** *5* (7), 1315-1320.

42. Mazille, F.; Fei, Z.; Kuang, D.; Zhao, D.; Zakeeruddin, S. M.; Grätzel, M.; Dyson, P. J. Influence of ionic liquids bearing functional groups in dye-sensitized solar cells. *Inorganic Chemistry* **2006,** *45* (4), 1585-1590.

43. Bessho, T.; Yoneda, E.; Yum, J. H.; Guglielmi, M.; Tavernelli, I.; Imai, H.; Rothlisberger, U.; Nazeeruddin, M. K.; Grätzel, M. New paradigm in molecular engineering of sensitizers for solar cell applications. *Journal of the American Chemical Society* **2009,** *131* (16), 5930-5934.

44. Zhang, L.; Cole, J. M. Anchoring groups for dye-sensitized solar cells. *ACS Applied Materials & Interfaces* **2015,** *7* (6), 3427-3455.

45. Galoppini, E. Linkers for anchoring sensitizers to semiconductor nanoparticles. *Coordination Chemistry Reviews* **2004,** *248* (13-14), 1283-1297.

46. Kalyanasundaram, K; Grätzel, M. Applications of functionalized transition metal complexes in photonic and optoelectronic devices. *Coordination Chemistry Reviews* **1998,** *77* (1), 347-414.

47. Campbell, W. M.; Burrell, A. K.; Officer, D. L.; Jolley, K. W. Porphyrins as light harvesters in the dye-sensitised TiO_2 solar cell. *Coordination Chemistry Reviews* **2004,** *248* (13-14), 1363-1379.

48. Li, L. L.; Diau, E. W. Porphyrin-sensitized solar cells. *Chemical Society Reviews* **2013,** *42* (1), 291-304.

49. Wu, J.; Lan, Z.; Lin, J.; Huang, M.; Huang, Y.; Fan, L.; Luo, G. Electrolytes in dye-sensitized solar cells. *Chemical Reviews* **2015,** *115* (5), 2136-2173.

50. Maçaira, J.; Andrade, L.; Mendes, A. Review on nanostructured photoelectrodes for next generation dye-sensitized solar cells. *Renewable and Sustainable Energy Reviews* **2013,** *27*, 334-349.

51. Raj, C. C.; Prasanth, R. A critical review of recent developments in nanomaterials for photoelectrodes in dye sensitized solar cells. *Journal of Power Sources* **2016,** *317*, 120-132.

52. Snaith, H. J. Estimating the maximum attainable efficiency in dye-sensitized solar cells. *Advanced Functional Materials* **2010,** *20* (1), 13-19.

53. Yum, J. H.; Walter, P.; Huber, S.; Rentsch, D.; Geiger, T.; Nüesch, F.; De Angelis, F.; Grätzel, M.; Nazeeruddin, M. K. Efficient far red sensitization of nanocrystalline TiO_2 films by an unsymmetrical squaraine dye. *Journal of the American Chemical Society* **2007,** *129* (34), 10320-10321.

54. Burke, A.; Schmidt-Mende, L.; Ito, S.; Grätzel, M. A novel blue dye for near-IR 'dye-sensitised'solar cell applications. *Chemical Communications* **2007,** (3), 234-236.

55. Kuang, D.; Walter, P.; Nüesch, F.; Kim, S.; Ko, J.; Comte, P.; Zakeeruddin, S. M.; Nazeeruddin, M. K.; Grätzel, M. Co-sensitization of organic dyes for efficient ionic liquid electrolyte-based dye-sensitized solar cells. *Langmuir* **2007,** *23* (22), 10906-10909.

56. Inakazu, F.; Noma, Y.; Ogomi, Y.; Hayase, S. Dye-sensitized solar cells consisting of dye-bilayer structure stained with two dyes for harvesting light of wide range of wavelength. *Applied Physics Letters* **2008,** *93* (9), 323.

57. Holliman, P. J.; Davies, M. L.; Connell, A.; Velasco, B. V.; Watson, T. M. Ultra-fast dye sensitisation and co-sensitisation for dye sensitized solar cells. *Chemical Communications* **2010,** *46* (38), 7256-7258.

58. Babu, D. D.; Elsherbiny, D.; Cheema, H.; El-Shafei, A.; Adhikari, A. V. Highly efficient panchromatic dye-sensitized solar cells: synergistic interaction of ruthenium sensitizer with novel co-sensitizers carrying different acceptor units. *Dyes and Pigments* **2016,** *132*, 316-328.

59. Chiang, Y. F.; Chen, R. T.; Burke, A.; Bach, U.; Chen, P.; Guo, T. F. Non-color distortion for visible light transmitted tandem solid state dye-sensitized solar cells. *Renewable Energy* **2013,** *59*, 136-140.

60. Lan, C. M.; Wu, H. P.; Pan, T. Y.; Chang, C. W.; Chao, W. S.; Chen, C. T.; Wang, C. L.; Lin, C. Y.; Diau, E. W. G. Enhanced photovoltaic performance with co-sensitization of porphyrin and an organic dye in dye-sensitized solar cells. *Energy & Environmental Science* **2012,** *5* (4), 6460-6464.

61. Sharma, G. D.; Angaridis, P. A.; Pipou, S.; Zervaki, G. E.; Nikolaou, V.; Misra, R.; Coutsolelos, A. G. Efficient co-sensitization of dye-sensitized solar cells by novel porphyrin/triazine dye and tertiary aryl-amine organic dye. *Organic Electronics* **2015,** *25*, 295-307.

62. Ikeuchi, T.; Agrawal, S.; Ezoe, M.; Mori, S.; Kimura, M. Enhanced charge separation efficiency in pyridine-anchored phthalocyanine-sensitized solar cells by linker elongation. *Chemistry–An Asian Journal* **2015,** *10* (11), 2347-2351.

63. Dong, L.; Zheng, Z.; Wang, Y.; Li, X.; Hua, J.; Hu, A. Co-sensitization of N719 with polyphenylenes from the Bergman cyclization of maleimide-based enediynes for dye-sensitized solar cells. *Journal of Materials Chemistry A* **2015,** *3* (21), 11607-11614.

64. Ma, B.; Gao, R.; Wang, L.; Zhu, Y.; Shi, Y.; Geng, Y.; Dong, H.; Qiu, Y. Recent progress in interface modification for dye-sensitized solar cells. *Science China Chemistry* **2010,** *53* (8), 1669-1678.

65. Gondane, V.; Bhargava, P. Tuning flat band potential of TiO_2 using an electrolyte additive to enhance open circuit voltage and minimize current loss in dye sensitized solar cells. *Electrochimica Acta* **2016,** *209*, 293-298.

66. Omelianovych, O.; Dao, V. D.; Larina, L. L.; Choi, H. S. Optimization of the PtFe alloy structure for application as an efficient counter electrode for dye-sensitized solar cells. *Electrochimica Acta* **2016,** *211*, 842-850.

67. Zhang, Y.; Khamwannah, J.; Kim, H.; Noh, S. Y.; Yang, H.; Jin, S. Improved dye sensitized solar cell performance in larger cell size by using TiO_2 nanotubes. *Nanotechnology* **2013,** *24* (4), 045401.

68. Sommeling, P.; O'Regan, B.; Haswell, R.; Smit, H.; Bakker, N.; Smits, J.; Kroon, J.; Van Roosmalen, J. Influence of a $TiCl_4$ post-treatment on nanocrystalline TiO_2 films in dye-sensitized solar cells. *The Journal of Physical Chemistry B* **2006,** *110* (39), 19191-19197.

69. Love, J. C.; Estroff, L. A.; Kriebel, J. K.; Nuzzo, R. G.; Whitesides, G. M. Self-assembled monolayers of thiolates on metals as a form of nanotechnology. *Chemical Reviews* **2005,** *105* (4), 1103-1170.

70. Strong, L.; Whitesides, G. M. Structures of self-assembled monolayer films of organosulfur compounds adsorbed on gold single crystals: electron diffraction studies. *Langmuir* **1988,** *4* (3), 546-558.

71. Nuzzo, R. G.; Allara, D. L. Adsorption of bifunctional organic disulfides on gold surfaces. *Journal of the American Chemical Society* **1983,** *105* (13), 4481-4483.

72. Techane, S. D.; Gamble, L. J.; Castner, D. G. X-ray photoelectron spectroscopy characterization of gold nanoparticles functionalized with amine-terminated alkanethiols. *Biointerphases* **2011,** *6* (3), 98-104.

73. Michota, A.; Bukowska, J. Surface-enhanced Raman scattering (SERS) of 4-mercaptobenzoic acid on silver and gold substrates. *Journal of Raman Spectroscopy* **2003,** *34* (1), 21-25.

74. Ho, C. H.; Lee, S. SERS and DFT investigation of the adsorption behavior of 4-mercaptobenzoic acid on silver colloids. *Colloids and Surfaces A: Physicochemical and Engineering Aspects* **2015,** *474*, 29-35.

75. Zhang, X.; Yu, Z.; Ji, W.; Sui, H.; Cong, Q.; Wang, X.; Zhao, B. Charge-transfer effect on surface-enhanced raman scattering (SERS) in an ordered Ag NPs/4-mercaptobenzoic acid/TiO2 system. *The Journal of Physical Chemistry C* **2015,** *119* (39), 22439-22444.

76. Ma, W. Q.; Fang, Y.; Hao, G. I.; Wang, W. G. Adsorption behaviors of 4-mercaptobenzoic acid on silver and gold films. *Chinese Journal of Chemical Physics* **2010,** *23* (6), 659.

77. Laibinis, P. E.; Whitesides, G. M.; Allara, D. L.; Tao, Y. T.; Parikh, A. N.; Nuzzo, R. G. Comparison of the structures and wetting properties of self-assembled monolayers of n-alkanethiols on the coinage metal surfaces, copper, silver, and gold. *Journal of the American Chemical Society* **1991,** *113* (19), 7152-7167.

78. Bourg, M. C.; Badia, A.; Lennox, R. B. Gold− sulfur bonding in 2D and 3D self-assembled monolayers: XPS characterization. *The Journal of Physical Chemistry B* **2000,** *104* (28), 6562-6567.

79. Ji, J.; Zhang, G.; Chen, H.; Li, Y.; Zhang, G.; Zhang, F.; Fan, X. A general strategy to prepare graphene-metal/metal oxide nanohybrids. *Journal of Materials Chemistry* **2011,** *21* (38), 14498-14501.

80. Castner, D. G.; Hinds, K.; Grainger, D. W. X-ray photoelectron spectroscopy sulfur 2p study of organic thiol and disulfide binding interactions with gold surfaces. *Langmuir* **1996,** *12* (21), 5083-5086.

81. Srinivasan, V.; Stiefel, E.; Elsberry, A.; Walton, R. X-ray photoelectron spectra of inorganic molecules. 21. Sulfur 2p chemical shifts associated with the binding of thiol and thioether groups of transition metal ions. *Journal of the American Chemical Society* **1979,** *101* (10), 2611-2614.

82. Gerson, A. R.; Bredow, T. Interpretation of sulphur 2p XPS spectra in sulfide minerals by means of ab initio calculations. *Surface and Interface Analysis* **2000,** *29* (2), 145-150.

83. Miao, P.; Shen, M.; Ning, L.; Chen, G.; Yin, Y. Functionalization of platinum nanoparticles for electrochemical detection of nitrite. *Analytical and Bioanalytical Chemistry* **2011,** *399* (7), 2407-2411.

84. Bokoch, M. P.; Devadoss, A.; Palencsár, M. S.; Burgess, J. D. Steady-state oxidation of cholesterol catalyzed by cholesterol oxidase in lipid bilayer membranes on platinum electrodes. *Analytica Chimica Acta* **2004,** *519* (1), 47-55.

85. Beebe, J. M.; Engelkes, V. B.; Miller, L. L.; Frisbie, C. D. Contact resistance in metal− molecule−metal junctions based on aliphatic SAMs: Effects of surface linker and metal work function. *Journal of the American Chemical Society* **2002,** *124* (38), 11268-11269.

86. Alloway, D. M.; Hofmann, M.; Smith, D. L.; Gruhn, N. E.; Graham, A. L.; Colorado, R.; Wysocki, V. H.; Lee, T. R.; Lee, P. A.; Armstrong, N. R. Interface Dipoles Arising from Self-Assembled Monolayers on Gold: UV−Photoemission Studies of Alkanethiols and Partially Fluorinated Alkanethiols. *The Journal of Physical Chemistry B* **2003,** *107* (42), 11690-11699.

87. Kahsar, K. R.; Schwartz, D. K.; Medlin, J. W. Control of metal catalyst selectivity through specific noncovalent molecular interactions. *Journal of the American Chemical Society* **2013,** *136* (1), 520-526.

88. Bayindir, Z.; Duchesne, P.; Cook, S.; MacDonald, M.; Zhang, P. X-ray spectroscopy studies on the surface structural characteristics and electronic properties of platinum nanoparticles. *The Journal of Chemical Physics* **2009,** *131* (24), 244716.

89. Kopecky, A.; Liu, G.; Agushi, A.; Agrios, A. G.; Galoppini, E. Synthesis of bifunctional Ru complexes with 1, 2-dithiolane and carboxylate-substituted ligands. *Tetrahedron* **2014,** *70* (36), 6271-6275.

90. Rosario-Castro, B. I.; Fachini, E. R.; Hernández, J.; Pérez-Davis, M. E.; Cabrera, C. R. Electrochemical and surface characterization of 4-aminothiophenol adsorption at polycrystalline platinum electrodes. *Langmuir* **2006,** *22* (14), 6102-6108.

91. Kaur, I.; Zhao, X.; Bryce, M. R.; Schauer, P. A.; Low, P. J.; Kataky, R. Modification of electrode surfaces by self-assembled monolayers of thiol-terminated oligo (phenyleneethynylene) s. *ChemPhysChem* **2013,** *14* (2), 431-440.

92. Dablemont, C.; Lang, P.; Mangeney, C.; Piquemal, J. Y.; Petkov, V.; Herbst, F.; Viau, G. FTIR and XPS study of Pt nanoparticle functionalization and interaction with alumina. *Langmuir* **2008,** *24* (11), 5832-5841.

93. Wang, Y.; Ren, J.; Deng, K.; Gui, L.; Tang, Y. Preparation of tractable platinum, rhodium, and ruthenium nanoclusters with small particle size in organic media. *Chemistry of Materials* **2000,** *12* (6), 1622-1627.

94. Hauch, A.; Georg, A. Diffusion in the electrolyte and charge-transfer reaction at the platinum electrode in dye-sensitized solar cells. *Electrochimica Acta* **2001,** *46* (22), 3457-3466.

95. Calogero, G.; Calandra, P.; Irrera, A.; Sinopoli, A.; Citro, I.; Di Marco, G. A new type of transparent and low cost counter-electrode based on platinum nanoparticles for dye-sensitized solar cells. *Energy & Environmental Science* **2011,** *4* (5), 1838-1844.

96. Fang, X.; Ma, T.; Guan, G.; Akiyama, M.; Kida, T.; Abe, E. Effect of the thickness of the Pt film coated on a counter electrode on the performance of a dye-sensitized solar cell. *Journal of Electroanalytical Chemistry* **2004,** *570* (2), 257-263.

97. Wang, G.; Xing, W.; Zhuo, S. Application of mesoporous carbon to counter electrode for dye-sensitized solar cells. *Journal of Power Sources* **2009,** *194* (1), 568-573.

98. Ikuta, N.; Tanaka, A.; Otsubo, A.; Ogawa, N.; Yamamoto, H.; Mizukami, T.; Arai, S.; Okuno, M.; Terao, K.; Matsugo, S. Spectroscopic studies of R(+)-alpha-lipoic acid--cyclodextrin complexes. *International Journal of Molecular Sciences* **2014,** *15* (11), 20469-20485.

99. Li, S.; Knauer, A.; Risch, K.; Ritter, U.; Koehler, J. M. Synthesis and characterization of ZnO/4-mercaptobenzoic acid/Au composite particles. *Materials Letters* **2013,** *91*, 103-106.

100. Nagashree, K.; Lavanya, R.; Kavitha, C.; Narayanan, N. V.; Sampath, S. Spontaneous formation of branched nanochains from room temperature molten amides: visible and near-IR active, SERS substrates for non-fluorescent and fluorescent analytes. *Rsc Advances* **2013,** *3* (22), 8356-8364.

101. Li, R.; Lv, H.; Zhang, X.; Liu, P.; Chen, L.; Cheng, J.; Zhao, B. Vibrational spectroscopy and density functional theory study of 4-mercaptobenzoic acid. *Spectrochimica Acta Part A: Molecular and Biomolecular Spectroscopy* **2015,** *148*, 369-374.

102. Hunyadi, S. E.; Murphy, C. J. Bimetallic silver–gold nanowires: fabrication and use in surface-enhanced Raman scattering. *Journal of Materials Chemistry* **2006,** *16* (40), 3929-3935.

103. Liu, H.; Feng, Y.; Cao, H.; Yang, J. Pt-containing Ag_2S-noble metal nanocomposites as highly active electrocatalysts for the oxidation of formic acid. *Nano-Micro Letters* **2014,** *6* (3), 252-257.

104. Lee, H. I.; Joo, S. H.; Kim, J. H.; You, D. J.; Kim, J. M.; Park, J. N.; Chang, H.; Pak, C. Ultrastable Pt nanoparticles supported on sulfur-containing ordered mesoporous carbon via strong metal-support interaction. *Journal of Materials Chemistry* **2009,** *19* (33), 5934-5939.

105. Hammond, J.; Winograd, N. XPS spectroscopic study of potentiostatic and galvanostatic oxidation of Pt electrodes in H_2SO_4 and $HClO_4$. *Journal of Electroanalytical Chemistry and Interfacial Electrochemistry* **1977,** *78* (1), 55-69.

106. Kwon, K.; Jin, S. A.; Pak, C.; Chang, H.; Joo, S. H.; Lee, H. I.; Kim, J. H.; Kim, J. M. Enhancement of electrochemical stability and catalytic activity of Pt nanoparticles via strong metal-support interaction with sulfur-containing ordered mesoporous carbon. *Catalysis Today* **2011,** *164* (1), 186-189.

107. Li, Z.; Chang, S.-C.; Williams, R. S. Self-assembly of alkanethiol molecules onto platinum and platinum oxide surfaces. *Langmuir* **2003,** *19* (17), 6744-6749.

108. Wu, H.; Tang, R.; He, Q.; Liao, X.; Shi, B. Highly stable Pt nanoparticle catalyst supported by polyphenol-grafted collagen fiber and its catalytic application in the hydrogenation of olefins. *Journal of Chemical Technology and Biotechnology* **2009,** *84* (11), 1702-1711.

109. Grimme, R. A.; Lubner, C. E.; Bryant, D. A.; Golbeck, J. H. Photosystem I/molecular wire/metal nanoparticle bioconjugates for the photocatalytic production of H_2. *Journal of the American Chemical Society* **2008,** *130* (20), 6308-6309.

110. Kou, R.; Shao, Y.; Wang, D.; Engelhard, M. H.; Kwak, J. H.; Wang, J.; Viswanathan, V. V.; Wang, C.; Lin, Y.; Wang, Y. Enhanced activity and stability of Pt catalysts on functionalized graphene sheets for electrocatalytic oxygen reduction. *Electrochemistry Communications* **2009,** *11* (5), 954-957.

111. Kou, R.; Shao, Y.; Mei, D.; Nie, Z.; Wang, D.; Wang, C.; Viswanathan, V. V.; Park, S.; Aksay, I. A.; Lin, Y. Stabilization of electrocatalytic metal nanoparticles at metal− metal oxide− graphene triple junction points. *Journal of the American Chemical Society* **2011,** *133* (8), 2541-2547.

112. Wang, Y.; Shen, Y.; Qiu, Y.; Zhang, T.; Liao, Y.; Zhao, S.; Ma, J.; Mao, H. Biopolymer-stabilized Pt nanoparticles colloid: a highly active and recyclable catalyst for biphasic catalysis. *Journal of Nanoparticle Research* **2016,** *18* (10), 293-300.

113. Eklund, S. E.; Cliffel, D. E. Synthesis and catalytic properties of soluble platinum nanoparticles protected by a thiol monolayer. *Langmuir* **2004,** *20* (14), 6012-6018.

114. Ahmadi, T. S.; Wang, Z. L.; Green, T. C.; Henglein, A.; El-Sayed, M. A. Shape-controlled synthesis of colloidal platinum nanoparticles. *Science* **1996,** *272* (5270), 1924-1925.

115. Cao, M.; Miyabayashi, K.; Shen, Z.; Ebitani, K.; Miyake, M. Olefin hydrogenation catalysis of platinum nanocrystals with different shapes. *Journal of Nanoparticle Research* **2011,** *13* (10), 5147.

116. Kotani, H.; Hanazaki, R.; Ohkubo, K.; Yamada, Y.; Fukuzumi, S. Size-and shape-dependent activity of metal nanoparticles as hydrogen-evolution catalysts: mechanistic insights into photocatalytic hydrogen rvolution. *Chemistry-A European Journal* **2011,** *17* (9), 2777-2785.

117. Liu, G.; Arellano-Jimenez, M. J.; Carter, C. B.; Agrios, A. G. Preparation of functionalized platinum nanoparticles: a comparison of different methods and reagents. *Journal of Nanoparticle Research* **2013,** *15* (6), 1744.

118. Zhang, B.; Wang, D.; Hou, Y.; Yang, S.; Yang, X. H.; Zhong, J. H.; Liu, J.; Wang, H. F.; Hu, P.; Zhao, H. J.; Yang, H. G. Facet-dependent catalytic activity of platinum nanocrystals for triiodide reduction in dye-sensitized solar cells. *Scientific Reports* **2013,** *3*, 1836-1842.

119. Campbell, S.; Smith, J.; Lloyd, G.; Walsh, F.; Ralph, T. Electrochemical and microscopic characterisation of platinum-coated perfluorosulfonic acid (Nafion 117) materials. *Analyst* **1998,** *123* (10), 1923-1929.

120. Wang, P.; Zakeeruddin, S. M.; Comte, P.; Charvet, R.; Humphry-Baker, R.; Grätzel, M. Enhance the performance of dye-sensitized solar cells by co-grafting amphiphilic sensitizer and hexadecylmalonic acid on TiO_2 nanocrystals. *The Journal of Physical Chemistry B* **2003,** *107* (51), 14336-14341.

121. Scheer, H. An overview of chlorophylls and bacteriochlorophylls: biochemistry, biophysics, functions and applications. In *Chlorophylls and Bacteriochlorophylls*; Springer, **2006,** 1-26.

122. Stromberg, J. R.; Marton, A.; Kee, H. L.; Kirmaier, C.; Diers, J. R.; Muthiah, C.; Taniguchi, M.; Lindsey, J. S.; Bocian, D. F.; Meyer, G. J. Examination of tethered porphyrin, chlorin, and bacteriochlorin molecules in mesoporous metal-oxide solar cells. *The Journal of Physical Chemistry C* **2007,** *111* (42), 15464-15478.

123. Spellane, P. J.; Gouterman, M.; Antipas, A.; Kim, S.; Liu, Y. C. Porphyrins. 40. Electronic spectra and four-orbital energies of free-base, zinc, copper, and palladium tetrakis(perfluorophenyl)porphyrins. *Inorganic Chemistry* **1980,** *19* (2), 386-391.

124. Sun, X.; Wang, Y.; Li, X.; Ågren, H.; Zhu, W.; Tian, H.; Xie, Y. Cosensitizers for simultaneous filling up of both absorption valleys of porphyrins: a novel approach for developing efficient panchromatic dye-sensitized solar cells. *Chemical Communications* **2014,** *50* (98), 15609-15612.

125. Hewage, N.; Yang, B.; Agrios, A. G.; Brückner, C. Introduction of carboxylic ester and acid functionalities to meso-tetrakis(pentafluorophenyl)porphyrin and their limited electronic effects on the chromophore. *Dyes and Pigments* **2015,** *121*, 159-169.

126. Ambre, R. B.; Chang, G. F.; Hung, C. H. Three p-carboxyphenyl groups possessing zinc porphyrins: efficient, stable, and cost-effective sensitizers for dye-sensitized solar cells. *Chemical Communications* **2014,** *50*, 725–727.

127. Galoppini, E. Linkers for anchoring sensitizers to semiconductor nanoparticles. *Coordination Chemistry Reviews* **2004,** *248* (13-14), 1283-1297.

128. Duclairoir, F.; Marchon, J. C. Anchoring of Porphyrins and Phthalocyanines on Conductors and Semiconductors for Use in Hybrid Electronics. In *Handbook of Porphyrin Scienc*e: *With Applications to Chemistry, Physics, Materials Science, Engineering, Biology and Medicine* **2010,** *10*, 245-311.

129. Wuts, P. G. M.; Green, T. W. *Protective Groups in Organic Synthesis*; 4th ed.; John Wiley & Sons: New York, **2006.**

130. Kadish, K. M.; Royal, G.; van Caemelbecke, E.; Gueletti, L. Metalloporphyrins in Nonaqueous Media: Database of Redoxpotentials. In *The Porphyrin Handbook*, Kadish, K. M.; Smith, K. M.; Guilard, R., Eds.; Academic Press: San Diego, **2000,** *9*, 1-219.

131. Starnes, S. D.; Rudkevich, D. M.; Rebek Jr., J. Cavitand-Porphyrins. *Journal of the American Chemical Society* **2001,** *123* (20), 4659-4669.

132. Sutton, J. M.; Clarke, O. J.; Fernandez, N.; Boyle, R. W. Porphyrin, Chlorin, and Bacteriochlorin Isothiocyanates: Useful Reagents for the Synthesis of Photoactive Bioconjugates. *Bioconjugate Chemistry* **2002,** *13* (2), 249-263.

133. Bruhn, T.; Brückner, C. Origin of the Regioselective Reduction of Chlorins. *Journal of Organic Chemistry* **2015,** *80* (10), 4861-4868.

134. Hyland, M. A.; Hewage, N.; Walton, K.; Nimthong Roldan, A.; Zeller, M.; Samaraweera, M.; Gascon, J. A.; Brückner, C. Chromene-annulated Bacteriochlorins. *Journal of Organic Chemistry* **2016,** *81*, 3603–3618.

135. Kratky, C.; Waditschatka, R.; Angst, C.; Johansen, J. E.; Plaquevent, J. C.; Schreiber, J.; Eschenmoser, A. Die Sattelkonformation der hydroporphinoiden Ni(II)-Komplexe: Struktur, Ursprung, und stereochemische Konsequenzen. *Helvetica Chimica Acta* **1985,** *68*, 1312-1337.

136. Ryeng, H.; Ghosh, A. Do Nonplanar Distortions of Porphyrins Bring about Strongly Red-Shifted Electronic Spectra? Controversy, Consensus, New Developments, and Relevance to Chelatates. *Journal of the American Chemical Society* **2002,** *124*, 8099-8103.

137. Parusel, A. B.; Wondimagegn, T.; Ghosh, A. Do nonplanar porphyrins have red-shifted electronic spectra? A DFT/SCI study and reinvestigation of a recent proposal. *Journal of the American Chemical Society.* **2000,** *122* (27), 6371-6374.

138. Gouterman, M. Optical spectra and electronic structure of porphyrins and related rings. In *The Porphyrins*, Dolphin, D., Ed.; Academic Press: New York, **1978,** *3*, 1-165.

139. Fukuzumi, S.; Ohkubo, K.; Chen, Y.; Pandey, R. K.; Zhan, R.; Shao, J.; Kadish, K. M. Photophysical and Electrochemical Properties of New Bacteriochlorins and Characterization of Radical Cation and Radical Anion Species. The *Journal of Physical Chemistry A* **2002,** *106* (20), 5105-5113.

140. Liu, C.; Dobhal, M. P.; Ethirajan, M.; Missert, J. R.; Pandey, R. K.; Balasubramanian, S.; Sukumaran, D. K.; Zhang, M.; Kadish, K. M.; Ohkubo, K.; Fukuzumi, S. Highly Selective Synthesis of the Ring-B Reduced Chlorins by Ferric Chloride-Mediated Oxidation of Bacteriochlorins: Effects of the Fused Imide vs. Isocyclic Ring on Photophysical and Electrochemical Properties. *Journal of the American Chemical Society* **2008,** *130* (43), 14311-14323.

141. Kozyrev, A.; Ethirajan, M.; Chen, P.; Ohkubo, K.; Robinson, B. C.; Barkigia, K. M.; Fukuzumi, S.; Kadish, K. M.; Pandey, R. K. Synthesis, Photophysical and Electrochemistry of Near-IR Absorbing Bacteriochlorins Related to Bacteriochlorophyll a. *The Journal of Organic Chemistry* **2012,** *77* (22), 10260-10271.

142. Fukuda, T.; Makarova, E. A.; Luk'yanets, E. A.; Kobayashi, N. Synthesis and spectroscopic and electrochemical studies of novel benzo- or 2,3-naphtho-fused tetraazachlorins, bacteriochlorins, and isobacteriochlorins. *Chemistry—A European Journal.* **2004,** *10* (1), 117-133.

143. Mathew, S.; Imahori, H. Tunable, strongly-donating perylene photosensitizers for dye-sensitized solar cells. *Journal of Materials Chemistry* **2011,** *21* (20), 7166-7174.

144. Kozyrev, A.; Ethirajan, M.; Chen, P.; Ohkubo, K.; Robinson, B. C.; Barkigia, K. M.; Fukuzumi, S.; Kadish, K. M.; Pandey, R. K. Synthesis, photophysical and electrochemistry of near-IR absorbing bacteriochlorins related to bacteriochlorophyll a. *The Journal of Organic Chemistry* **2012,** *77* (22), 10260-10271.